The masses of nobelium and lawrencium isotopes, the mass difference between ^{180}W and ^{180}Hf, and a characterization of the future cryogenic stopping cell of the online mass spectrometer SHIPTRAP

I n a u g u r a l d i s s e r t a t i o n

zur

Erlangung des akademischen Grades eines

Doktors der Naturwissenschaften (Dr. rer. nat.)

der

Mathematisch-Naturwissenschaftlichen Fakultät

der

Ernst-Moritz-Arndt-Universität Greifswald

vorgelegt von

Christian Droese

geboren am 15.02.1984

in Wolgast

Greifswald, den 18.11.2014

ii

Dekan: Prof. Dr. Klaus Fesser

1. Gutachter: Prof. Dr. Lutz Schweikhard

2. Gutachter: Prof. Dr. Georg Bollen

Tag der Promotion: 29.01.2015

Contents

List of Figures

List of Tables

Nomenclature

$2\Delta r$	Spatial distribution of the projected ions onto the detector
A	Atomic mass number
B	Magnetic field strength
B_{2h}	Energy of the double-electron hole in the atomic shell of the daughter nuclide
BE	Binding energy
C	Capacity
c	Speed of light in vacuum
d	Characteristic Penning trap dimension
E	Energy
E_{el}	Electric field strength
E_{pot}	Potential energy
E_γ	Energy of the nuclear excited state
F	Viscous damping force
f	Surface normal
I	Current
K_0	Reduced ion mobility
k_B	Boltzmann constant
m	Atomic mass
m_n	Neutron mass
m_p	Proton mass
m_e	Electron mass
ME	Mass excess
N	Neutron number
$n_\pm$	Number of full revolutions of the magnetron or cyclotron motion
N_{ion}	Number of detected ions
p	Pressure
p_0	Standard pressure ($1013\,\mathrm{mbar}$)
Q	Quality factor
q	Electric charge of an ion
$Q_{\epsilon\epsilon}$	Mass difference between mother and daughter nuclide of the neutrinoless double-electron capture
R	Resolving power

R_p	Parasitic resistance
r_{ion}	Radius of an ion in the Penning trap
S_i	Separation energy, $i = n, 2n, p$
T	Temperature
t	Phase accumulation time
T_0	Standard temperature ($273.15\,\mathrm{K}$)
$T_{1/2}$	Half-life
T_{rev}	Data acquisition time
T_{RF}	Dipolar/Quadrupolar excitation period
U	Voltage
U_0	Electrostatic potential
U_d	Dipolar excitation signal
U_q	Quadrupolar excitation signal
v	Velocity
$|V_{\epsilon\epsilon}|$	Nuclear matrix element
x, y, z	Cartesian coordinates
Z	Proton number
$Z(\omega_{ion})$	Impedance
z_0	Distance of the center of the Penning trap to the endcap electrodes
δ	Damping coefficient
δ_{2n}	Shell-gap parameter
Δ	Degeneracy parameter
Φ	Phase angle
Γ_{2h}	Sum of the widths of the double-electron hole
$\lambda_{\epsilon\epsilon}$	Rate of the neutrinoless double-electron capture process
μ	Magnetic moment
μ_{dip}	Electric dipole moment
$\omega_z = 2\pi\nu_z$	Axial frequency
$\omega_c = 2\pi\nu_c$	Cyclotron frequency
$\omega_+ = 2\pi\nu_+$	Modified cyclotron frequency
$\omega_- = 2\pi\nu_-$	Magnetron frequency
σ	Fusion-evaporation reaction cross section
ρ_0	Distance of the center of the Penning trap to the ring electrodes
ρ, z	Cylindrical coordinates
θ	Time-dependent angle of the rotation
ζ	Charge density

Chapter 1

Introduction

The isotopic nature of elements was discovered in the beginning of the 20th century [Sod17]. The identification of the stable isotopes ^{20}Ne and ^{22}Ne by F. W. Aston [Ast20] with one of the first mass spectrometers with a relative precision on the order of 10^{-3} resulted in a revival of the 'whole number rule': all masses are whole numbers, and a fractional 'chemical' mass, like 20.2 for neon, is a mixture of isotopes. An exception was hydrogen with a mass of 1.008 in relation to ^{16}O = 16. With Einstein's fundamental relation $E = mc^2$ this mass excess was correctly interpreted by A. Eddington as the binding energy of the nucleus [Edd20]. In 1927 F. W. Aston built an improved mass spectrometer with a relative precision of 10^{-4}. The mass measurements revealed the violation of the 'whole number rule' which was first named the 'packing fraction' [Ast27] and later assigned to the binding energy of the nucleus. Thus, the mass of an atom provides insight into the fundamental interactions of protons and neutrons of the nucleus.

The binding energy of a nucleus with Z protons and N neutrons

$$BE(N, Z) = (N \cdot m_n + Z \cdot m_p + Z \cdot m_e - m)c^2 \qquad (1.1)$$

is the deficit of the total mass m from the sum of the mass of its constituents. It represents an average of the interactions of the protons and neutrons in the nucleus. In Eq. 1.1 m_n is the neutron mass, m_p is the proton mass and m_e is the electron mass. The binding energy gives insight into the nuclear structure. Of particular interest are nuclides with a composition of protons and neutrons that does not lead to stable conditions. These nuclei away from the region of stability are referred to as exotic nuclei. High-precision mass measurements are important to determine the masses of exotic nuclei in order to gain access to the nuclear structure. One example, is the calculation of the neutron separation energy

$$S_n = BE(N, Z) - BE(Z, N - 1) \qquad (1.2)$$

and the proton separation energy

$$S_p = BE(N, Z) - BE(Z - 1, N). \qquad (1.3)$$

The neutron separation energy and the proton separation energy fall below zero if it is energet-

Figure 1.1: Chart of nuclides presenting their decay modes. The dashed horizontal lines represent closed proton shells and the solid vertical lines indicate the closed neutron shells. The proton and the neutron drip lines according to predictions from the global finite range droplet model [Moe95] are indicated by the blue and the green solid line, respectively. Figure adapted from [NUC].

ically more favourable to separate a neutron or a proton from the nucleus, respectively. Thus, by calculation of the neutron and proton separation energies the position of the neutron and the proton drip line can be determined. In the chart of nuclides the proton and neutron drip lines enclose the region of nuclides that exist without prompt emission of protons and neutrons, respectively. In this region radionuclides decay by either α-decay, β-decay, electron capture or spontaneous fission (see Fig. 1.1).

For the observation of other nuclear structure effects the two-neutron separation energy

$$S_{2n} = BE(N, Z) - BE(N - 2, Z) \tag{1.4}$$

is more preferable since the pairing effects which lead to a zigzag structure in the S_n trends cancel out. By means of investigations of the two-neutron separation energies nuclear structure effects like shell-closure or shape coexistence [Hey11] become evident. The S_{2n} values for the mass region beyond lead are plotted in Fig. 1.2. Distinct kinks in the trends of the two-neutron
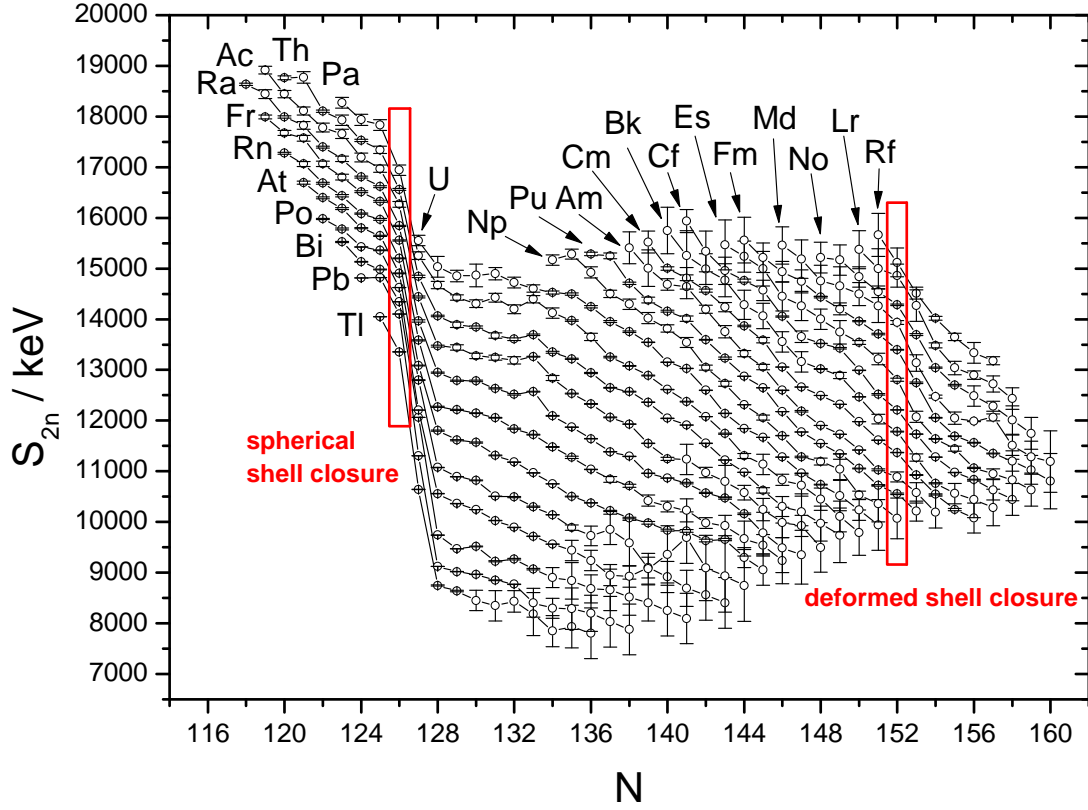
Figure 1.2: The two-neutron separation energy S_{2n} as a function of the neutron number N for region of heavy nuclides. The distinct kinks in the otherwise smooth trend indicate spherical neutron shell closure. Here, the shell closures at $N = 126$ and $N = 152$ are highlighted here by a red frame. The data was obtained from the atomic mass evaluation 2012 [Wan12].

separation energies reveal nuclear configurations in which spherical shell closure is obtained, which results in an enhanced stability of the nucleus. Under consideration of the two-neutron separation energies the shell gap parameter

$$\delta_{2n}(N, Z) = S_{2n}(N, Z) - S_{2n}(N + 2, Z). \tag{1.5}$$

can be calculated which enables the identification of less pronounced shell effects like the deformed shell closure. With the calculation of the shell gap parameter the deformed shell closure at the neutron number $N = 152$, which was mapped by the direct mass measurements of the transfermium elements $^{252-255}$No and ^{255,256}Lr by the high-precision Penning trap mass spectrometer SHIPTRAP, becomes evident (see thesis article I).

Due to extremely low production yields of exotic nuclei far away from the valley of stability one has to rely on estimated mass values based systematic trends in order to derive conclusive statements on the nuclear properties in a certain mass region. In Fig. 1.3 the differences between the two-neutron separation energies of nobelium isotopes given in [Wan12] and the predictions based on two different models, a global finite-range droplet model [Moe95] and a microscopic Hartree-Fock-Bogoliubov model with Skyrme interactions [Gor10], are depicted. The two-neutron separation energies of both mass models are fluctuating within several hun-
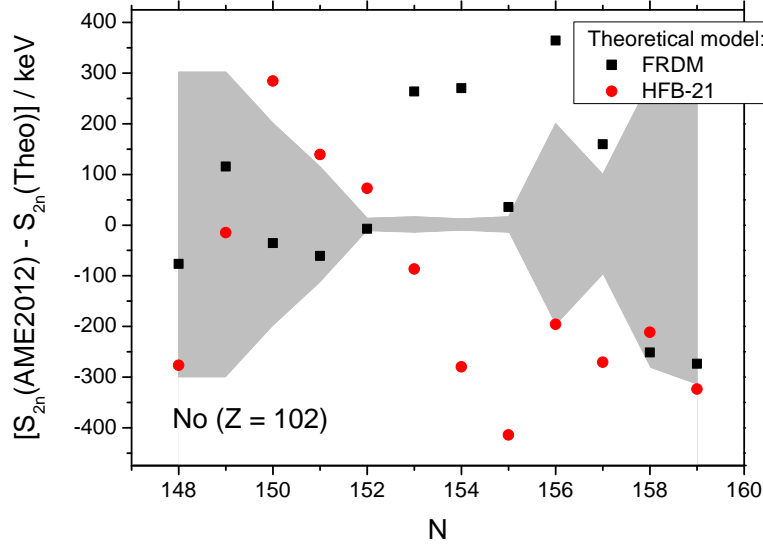
Figure 1.3: Comparison between the S_{2n} values for the element nobelium obtained from the atomic mass evaluation 2012 [Wan12] and predictions based on the microscopic-macroscopic finite-range-droplet-model (FRDM) [Moe95] and the microscopic Hartree-Fock-Bogoliubov model with Skyrme interactions labelled HFB-21 [Gor10]. The gray band indicates the uncertainties of the experimental values.

dreds of keV around the value given in the atomic mass evaluation 2012. The large deviation becomes even more evident for the isotopes $^{254-257}$No whose uncertainties of the S_{2n} values is about 20 keV due to the reduced mass uncertainty of the investigated nobelium isotopes (see Sec. 4.1).

The development of improved mass models implies the adjustment of the model parameters in order to reproduce known atomic masses. Thus, high-precision mass measurements are necessary to benchmark mass models and are a key requisite for the development of improved models.

The observation of nuclear structure effects like shell closure and tests of theoretical models requires accuracies on the order of 10^{-7} [Cha13, Eib13, Man13]. For g-factor measurements or tests of CPT symmetry relative mass uncertainties below the 10^{-10} level are a prerequisite

[Ulm11, Stu14].

The assessment of possible candidates for the exploration of the neutrinoless double-electron capture process of long-lived nuclides requires mass difference measurements of isobars with relative uncertainties on the order of 10^{-9} which corresponds to absolute uncertainties of about $100\,\mathrm{eV}/c^2$. The observation of the neutrinoless double-electron capture would imply that neutrinos are their own anti-particles, i.e. Majorana particles. In addition, the obtained data would provide information on the effective neutrino mass. The expected half-life of this decay is about 10^{30} years (for an assumed effective neutrino mass of $1\,\mathrm{eV}/c^2$) which results in a large quantity of material needed to equip experiments for the search for neutrinoless double-electron capture. However, the decay rate of neutrinoless double-electron capture is resonantly enhanced by up to six orders of magnitudes if the initial and final states of the transition are degenerate in energy [Ber83, Suj04]. In order to identify suitable candidates for large scale experiments the mass difference to its daughter nuclide needs to be precisely measured. These measurements have been extensively carried out at SHIPTRAP. In Sec. 4.2 an overview of the obtained results is presented. A detailed review of the mass-difference measurement between ^{180}W/^{180}Hf is presented in thesis article II.

After a brief introduction on the principles of the ion motion in a Penning trap (see Sec. 2.1), the buffer-gas cooling technique for isobar separation is presented in Sec. 2.2 which is a requirement for high-precision mass measurements with the time-of-flight ion-cyclotron-resonance (ToF-ICR) technique (see Sec. 2.3). The experimental setup of SHIPTRAP is described in Chapter 3. The recent and upcoming technical developments at SHIPTRAP are described in Chapter 5.

A major improvement of the SHIPTRAP setup with regard to the overall efficiency which is mostly limited by the stopping and extraction efficiency of the buffer-gas stopping cell is the development of a cryogenic gas stopping cell. In comparison to the first-generation buffer-gas cell the cryogenic gas cell has a larger stopping volume which has been calculated to result in an increase of the stopping efficiency by a factor of 2.5. Furthermore, the buffer gas is cooled to $40\,\mathrm{K}$ which results in a higher buffer-gas cleanliness due to freezing of the residual gas atoms (except hydrogen and helium). In offline measurements an increased extraction efficiency by a factor of two in comparison to the first-generation buffer-gas cell was obtained. The overall efficiency is given by the product of the stopping efficiency and the extraction efficiency. An increase by a factor of five is anticipated. A detailed presentation of the setup and the results of the first offline measurements using a ^{219}Rn recoil ion source are given in Sec. 5.1. and thesis article III.

Section 5.2 concerns the possible improvement of the measurement technique to increase the sensitivity of the setup. The achievable resolving power of the well established ToF-ICR technique is rather poor for heavy isotopes with half-lives shorter than $1\,\mathrm{s}$. Furthermore, the minimum number of detected ions necessary for mass measurements is about 50 which is difficult to obtain for exotic nuclides with production rates smaller than 1 per hour. To this end, two mass measurement techniques, which have been either developed at SHIPTRAP (Phase-Imaging Ion-Cyclotron-Resonance technique (see Sec. 5.2.1)) or are about to be implemented in the existing setup (Fourier-Transform Ion-Cyclotron-Resonance technique (see Sec. 5.2.2)),

are briefly presented.

Chapter 2

Mass measurements with Penning traps

Due to their versatility Penning traps are utilized in many fields in physics, e.g. mass spectrometry [Bla06], optical spectroscopy [Mav14] or g-factor measurements [Bla09]. Penning traps around the world are employed for high-precision mass measurements on exotic and stable nuclei across almost the entire known nuclear chart.

In a Penning trap ions are confined by superposition of a homogeneous magnetic field and an electrostatic quadrupole field created by a dedicated electrode structure. An ion is forced on a characteristic trajectory whose equation of motion can be solved analytically (see Sec. 2.1). The solution yields three independent motions with characteristic frequencies. From the radial eigenfrequencies the cyclotron frequency can be obtained. The cyclotron frequency ω_c gives access to the charge-to-mass ratio of the trapped ion. The frequency is the observable which can be determined with the highest precision. Due to this circumstance and other technical advancements, mass measurements can be performed with relative uncertainties smaller than 10^{-8} for exotic isotopes [Bla09a] and less than 10^{-11} for stable isotopes [Mye13].

Mass measurements with precisions on the ppb level require a particular careful preparation of a pure ion sample. Among other existing methods to purify and cool an ion sample the buffer-gas cooling technique, which is used at SHIPTRAP, is presented in Sec. 2.2.

The cyclotron frequency ω_c can be determined by various techniques like e.g. the phase-imaging ion-cyclotron-resonance technique (see Sec. 5.2.1) or the non-destructive Fourier-transform ion-cyclotron-resonance technique, which is addressed in Sec. 5.2.2. In Sec. 2.3 the established time-of-flight ion-cyclotron-resonance technique is presented.

2.1 Principle of the Penning trap

In the presence of a homogeneous magnetic field with the strength $\vec{B} = B\vec{e_z}$, an ion with the charge q and the velocity $\vec{v}$ is forced on a circular orbit. In Penning traps the Lorentz force is utilized to radially confine the charged particles. An ideal Penning trap consists of two hyperbolic endcap electrodes and one hyperbolic ring electrode with an applied electrostatic

potential U_0 (see Fig. 2.1 (a)). The distance from center of the trap to the endcap electrodes and the ring electrode is z_0 and ρ_0, respectively. Due to the hyperbolic shape of the electrodes an electrostatic quadrupole field is created that confines the ions in axial direction in a harmonic potential (see Fig. 2.1 (b)).

The equation of motion of an ion in a Penning trap is well understood and can be solved
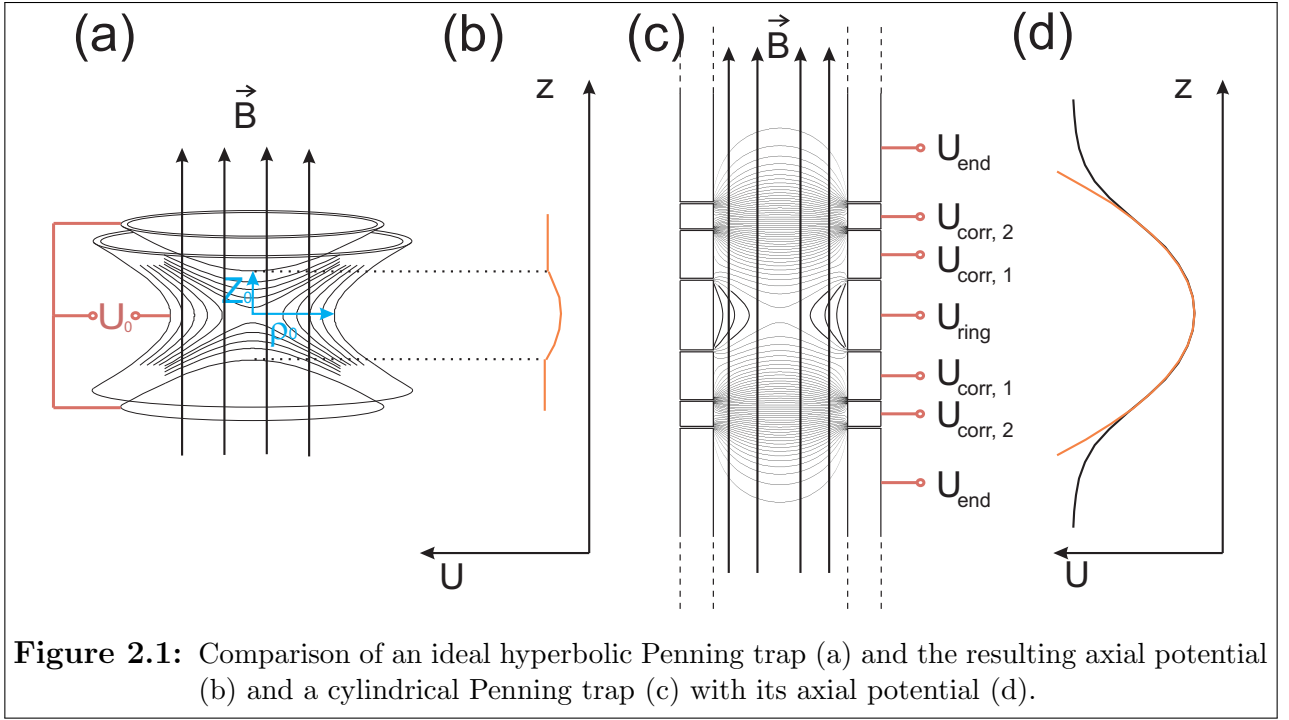
Figure 2.1: Comparison of an ideal hyperbolic Penning trap (a) and the resulting axial potential (b) and a cylindrical Penning trap (c) with its axial potential (d).

analytically [Bro86]. The electrostatic potential U with respect to the position of the ion in the Penning trap (in cylindrical coordinates ρ and z) is

$$U(\rho, z) = \frac{U_0}{2d^2}(z^2 - \frac{\rho^2}{2}). \tag{2.1}$$

Here, d is the characteristic trap dimension which is given by [Bro86]

$$d^2 = 1/2(z_0 + \rho_0^2/2). \tag{2.2}$$

The electric field strength can be easily calculated to

$$\vec{E}_{el}(\rho, z) = \frac{U_0}{d^2}(\frac{\vec{\rho}}{2} - \vec{z}). \tag{2.3}$$

Considering the orientation of the magnetic field along the symmetry axis z, the axial motion is decoupled from the radial motion. The axial equation of motion can be written as

$$\ddot{z} + \omega_z^2 z = 0 \tag{2.4}$$

which is the well-known equation of motion of a harmonic oscillator with the resonance frequency

$$\omega_z = \sqrt{\frac{qU_0}{md^2}}.$$ (2.5)

The superposition of the electrostatic force due to the quadrupole field (see Eq. 2.3) and the Lorentz force results in the radial equation of motion

$$\ddot{\vec{\rho}} = q \left(\frac{U_0 \vec{\rho}}{2d^2} + \dot{\vec{\rho}} \times \vec{B} \right).$$ (2.6)

Under the consideration of the definition of the cyclotron frequency

$$\omega_c = \frac{qB}{m}$$ (2.7)

and the axial resonance frequency ω_z (Eq. 2.5) the radial equation of motion can be written as

$$\ddot{\vec{\rho}} + \omega_c z \times \dot{\vec{\rho}} - \frac{1}{2} \omega_z^2 \vec{\rho} = 0.$$ (2.8)

With the introduction of the complex variable $u = x + iy$, the radial component of the equation of motion simplifies to

$$\ddot{u} + i\omega_c \dot{u} - \frac{\omega_z}{2} u = 0.$$ (2.9)

With the ansatz that $u = e^{-i\omega t}$ two characteristic frequencies of the radial motion arise:

$$\omega_\pm = \frac{\omega_c}{2} \pm \sqrt{\frac{\omega_c^2}{4} - \frac{\omega_z^2}{2}}.$$ (2.10)

Here, ω_+ is the modified cyclotron frequency, i.e. the cyclotron frequency reduced due to the presence of an electric field, and ω_- is the magnetron frequency, of the corresponding circular motional modes. From Eq. 2.10 the fundamental relation

$$\omega_c = \omega_+ + \omega_-$$ (2.11)

can be derived. As a result, the determination of the independent eigenfrequencies of the cyclotron motion ω_+ and the magnetron motion ω_- gives access to the 'pure' cyclotron frequency ω_c (in the absence of an electric trapping field) from which the charge-to-mass ratio q/m (see Eq. 2.7) can be calculated under the assumption of a known magnetic-field strength B. Experimentally, the magnetic-field strength B is determined by cyclotron frequency measurements of an ion with a well-known mass (e.g. $^{133}\text{Cs}^+$) or a ^{12}C cluster[1].
The solution of the equation of motion (Eq. 2.9) results in ion trajectories depicted in Fig 2.2. The ion motion is a superposition of three independent eigenmotions, i.e. the axial motion, the

---

[1]By definition a ^{12}C atom has no mass uncertainty. However, in a ^{12}C cluster the uncertainties of the covalent binding energy between the carbon atoms has to be considered.

Figure 2.2: The characteristic motion of an ion in a Penning trap consists of three independent eigenmotions, i.e. the axial motion, the cyclotron motion and the magnetron motion.
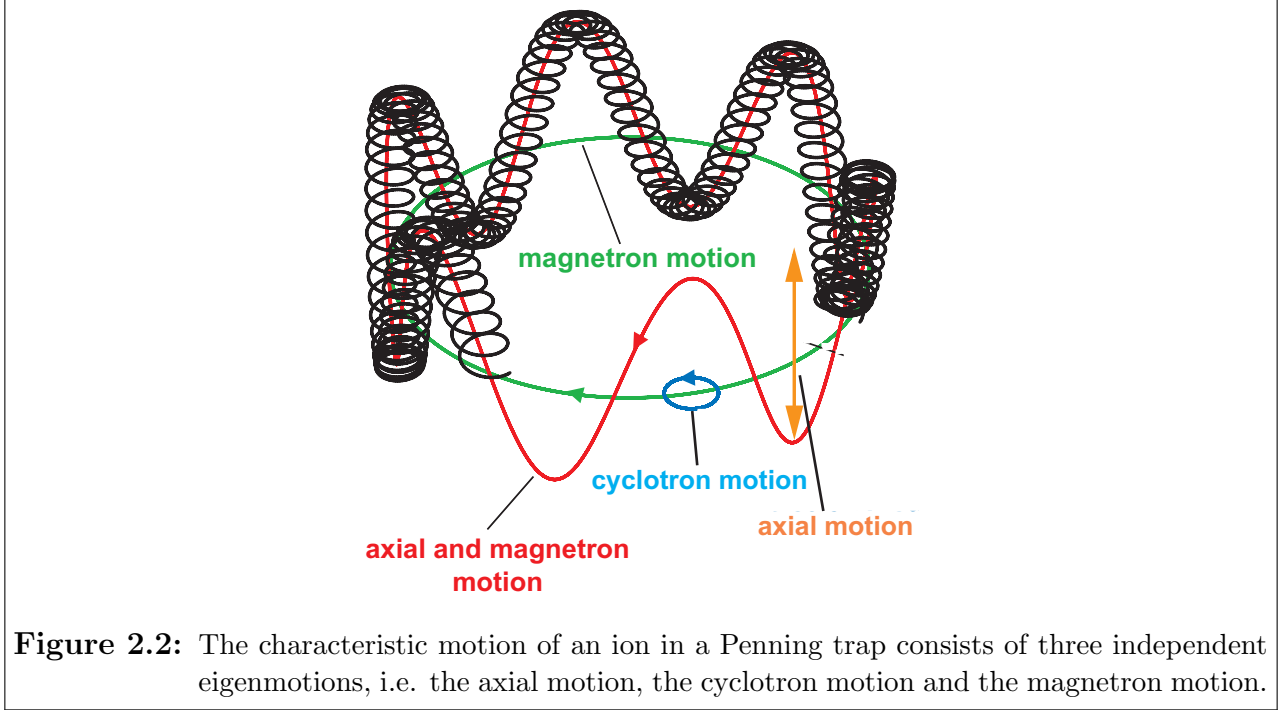
cyclotron motion and the magnetron motion. At SHIPTRAP the Penning traps have a cylindrical geometry. A schematic of a cylindrical Penning trap is given in Fig. 2.1 (c). Compared to the hyperbolic electrode structure, the manufacturing process of these electrodes as well as the ion injection into the traps is easier. A harmonic DC potential U (see Fig. 2.1 (d)) can be obtained in the vicinity of the ring electrode of the trap with the assistance of the adjacent correction electrodes.

In Tab. 2.1 the eigenfrequencies of $^{133}\text{Cs}^+$ determined at SHIPTRAP are presented. Here, a DC potential depth of $U_0 = $ -41.06 V was applied. The dimensions and the applied DC potentials of the second Penning trap of the SHIPTRAP tandem Penning trap system are given in Fig. 2.3. The magnetic-field strength of the SHIPTRAP solenoid is approximately 7.003 T [Dro11]. Using the fact that $\omega_c \gg \omega_z$ Eq. 2.10 can be simplified by means of the Taylor

Table 2.1: The eigenfrequencies of the cyclotron, magnetron and axial motion of a singly charged ^{133}Cs ion in the SHIPTRAP Penning trap with a DC potential depth $U_0 = 41.06$ V.

	Eigenfrequency / Hz
ν_+	80878.2
ν_-	545
ν_z	29691.3

expansion to

$$\omega_+ \approx \omega_c - \frac{U_0}{2d^2 B} \tag{2.12}$$
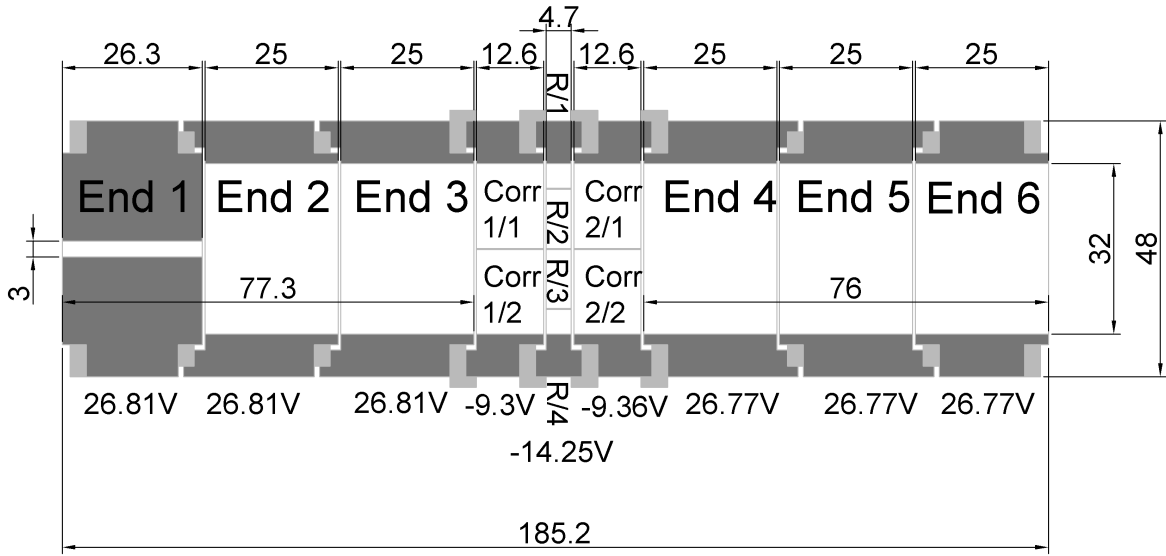
Figure 2.3: Cut of the second SHIPTRAP Penning trap. The copper electrodes are shown in dark grey and the ceramic insulators in light grey. The dimensions of the electrodes above are given in mm. On the bottom the applied voltages are shown.

and

$$\omega_- \approx \frac{U_0}{2d^2 B}. \tag{2.13}$$

Eq. 2.13 implies that the magnetron frequency is in first order independent from the charge-to-mass ratio of the trapped ion.

2.2 The buffer-gas cooling technique

The eigenmotions of an ion in a Penning trap are decoupled. Therefore, the individual modes can be excited independently. The axial motion can be excited by application of a dipolar rf field at the axial eigenfrequency ω_z at the endcap electrodes. The radial eigenmotions can be excited by dipolar and quadrupolar excitation which are applied via the two and four segments, respectively, of the eightfold segmented ring electrode (Fig. 2.4). For dipolar excitation of the magnetron motion an rf signal of the frequency $\nu_- = \omega_-/2\pi$ is applied. The radiofrequency is

Figure 2.4: Electrode configuration for dipolar and quadrupolar excitation in the radial plane of an eightfold segmented ring electrode: (a) A 180° phase shifted rf signal $\pm U_d$ at the magnetron frequency ω_- applied to two opposing electrodes increases the energy of the magnetron motion and, thus decreases the orbit of the ion motion. (b) Between electrodes shifted by 90° of the 8-fold segmented ring electrode a 180° phase shifted rf signal $\pm U_q$ with the frequency $\omega_c = \omega_+ + \omega_-$ is applied in order to convert the magnetron motion into cyclotron motion via quadrupolar excitation.

split in two 180° phase shifted signals $\pm U_d$ which are applied on two opposing segements of the ring electrode (Fig. 2.4 (a)). The dipolar excitation couples energy into the magnetron motion which decreases its orbit. The radius of magnetron motion is antiproportional to the amplitude of U_d and duration of the rf signal T_{RF}. In first order the magnetron frequency is independent from the ion mass (see Eq. 2.13).

For the application of the quadrupolar excitation, an rf signal $\pm U_q$ with the frequency ω_c is applied to four elements of the eightfold segmented ring electrode with a phase difference of 180° between adjacent active segments (Fig. 2.4 (b)). By use of the quadrupolar excitation at the side-band frequency, i.e. the cyclotron frequency $\omega_c = \omega_+ + \omega_-$ the magnetron motion can be converted into the cyclotron motion. In case of a full conversion the final radius of the cyclotron motion equals the initial radius of the magnetron motion. The magnetron motion of any contaminant ions in the Penning trap is not converted into cyclotron motion.

For high-precision Penning trap mass measurements the preparation of the ion sample is crucial. Ideally, a mass measurement is performed with a single ion in the trap. Larger quantities of ions and, in particular, the presence of contaminant ions within a sample of ions of interest in the trap alters the resulting frequency and can, thus, lead to deviations from the correct mass value [Jef83]. Furthermore, the energy of the ions needs to be well tuned to trap them in the harmonic part of the DC potential which requires ion cooling. Besides collisionless techniques like resistive cooling [Ita95], laser cooling [Jav80, Jav81] and stochastic cooling [Bev88, Bev88a] the preparation of a cooled isobaric pure sample can be performed as well with the buffer-gas

cooling technique [Sav91] which is utilized at SHIPTRAP. With the buffer-gas cooling technique energy is removed from the trapped ions by collisions with helium gas atoms. At SHIPTRAP this preparation is performed in the first Penning trap of the tandem Penning trap system (see Sec. 3.4).

In the presence of buffer gas, typically a noble gas like helium or argon (with large ionization potential for reduced probability to undergo charge exchange reactions or molecule formation with the ions of interest), the ion motion is damped. The damping force on an ion with the charge q and the mass m propagating with a velocity v through such a medium can be described by a viscous damping force

$$F = -\delta \cdot m \cdot v. \tag{2.14}$$

The damping coefficient δ is given by

$$\delta = \frac{qpT_0}{mK_0p_0T}. \tag{2.15}$$

Here, p is the pressure and T the temperature of the buffer gas in the Penning trap. Furthermore, K_0 is the tabulated reduced ion mobility of the ion in the buffer gas. T_0 and p_0 are the standard temperature of $273.15\,\mathrm{K}$ and the standard pressure of $1013\,\mathrm{mbar}$, respectively.

As Eq. 2.14 indicates, the damping force increases with increasing velocity. Since $\omega_+ \gg \omega_-$ (see Tab. 2.1) the kinetic energy of cyclotron motion decreases faster than the kinetic energy of the magnetron motion as depicted in Fig. 2.5 (a). Thus, by application of the mass-selective

Figure 2.5: In the presence of buffer gas the particle motion is damped. (a) The initial cyclotron motion disappears rapidly while the damping increases the orbit of the magnetron motion. (b) While applying the quadrupolar excitation with $\omega_c = \omega_+ + \omega_-$ the orbit of the cyclotron motion decreases as well as the radius of the magnetron motion due to the conversion into the cyclotron motion. Ultimately, the ions of interest remain in the center of the trap indicated by the intersection of the straight lines. Figure taken from [Web04].

quadrupolar excitation the ions of interest are separated from the contaminants in the phase space. Due to the presence of buffer-gas atoms, the viscous damping force (Eq. 2.14) reduces the kinetic energy of the magnetron motion which results in an increasing orbit. The conversion

of the magnetron motion into cyclotron motion by application of the quadrupolar excitation decreases the radius of the magnetron motion of the ions of interest while simultaneously the orbit of the cyclotron motion is efficiently reduced in the presence of the buffer gas. After a certain cooling time the cyclotron motion has vanished and an isobarically pure sample of ions of interest remains in the center of the Penning trap.

At SHIPTRAP a tandem Penning trap system is installed which consists of two traps, separated by a concentric orifice with a diameter of 1.5 mm (see Sec. 3.4). By switching the endcap electrodes of the first Penning trap, a potential gradient is created that transports the cooled ions of interest through the orifice while the contaminants at a larger orbit collide with the aperture. The ions of interest are injected into the second Penning trap which is utilized for mass measurement by means of the Time-of-Flight Ion-cyclotron-resonance technique which is presented in the following section.

2.3 The Time-of-Flight Ion-Cyclotron-Resonance technique

The Time-of-Flight Ion-Cyclotron-Resonance (ToF-ICR) technique is a well-known method to measure the cyclotron frequency ω_c of ions in the Penning trap. The ToF-ICR technique utilizes the manipulation of the ion motion by means of dipolar and quadrupolar excitation which have been introduced in Sec. 2.2. In this section the measurement principle will be described briefly. A detailed discussion can be found in [Gra80]. An ion with the charge q moving at a frequency ω in a Penning trap creates a current

$$I = \frac{q\omega}{2\pi}, \tag{2.16}$$

which results in a magnetic moment

$$\vec{\mu} = I \cdot \vec{f}. \tag{2.17}$$

The surface normal $\vec{f}$ of the surface $F = \pi\rho^2$ enclosed by the particle trajectory is antiparallel to the magnetic field $\vec{B} = B \cdot \vec{e_z}$ which is oriented along the z axis. Therefore, the potential energy of an ion circulating in the homogeneous magnetic field can be calculated under the consideration of Eq. 2.16 with

$$E_{pot} = \mu \cdot B = \frac{q\omega\rho^2 B}{2}. \tag{2.18}$$

As the ions are ejected from the Penning trap they experience a strong magnetic-field gradient (Fig. 2.6). Passing the gradient, the potential energy of the motional magnetic moment in the trap (see Eq. 2.18) is transformed into axial kinetic energy. Thus, the particle is accelerated by

$$F = \mu\frac{\partial B}{\partial z}. \tag{2.19}$$

According to Eq. 2.16 and Eq. 2.17, $\vec{F}$ is proportional to the revolution frequency ω of the trapped ion. The revolution frequency can be manipulated by application of the dipolar and
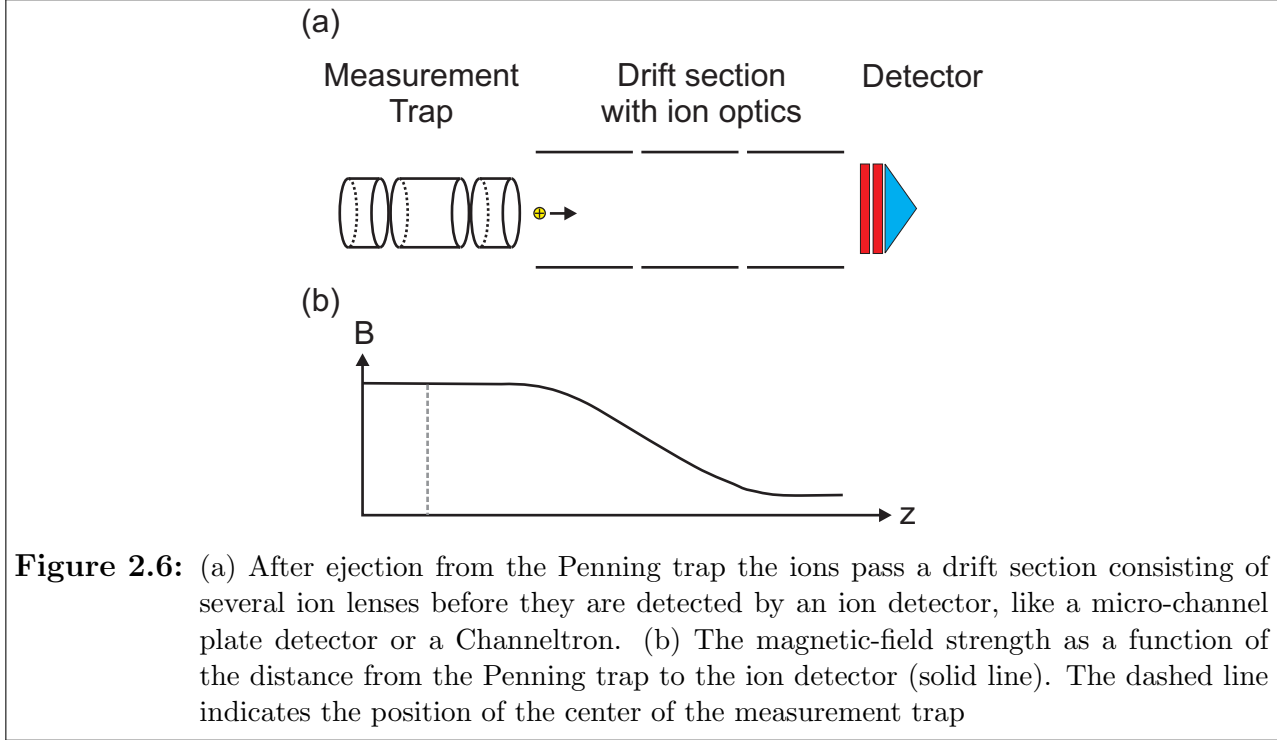
Figure 2.6: (a) After ejection from the Penning trap the ions pass a drift section consisting of several ion lenses before they are detected by an ion detector, like a micro-channel plate detector or a Channeltron. (b) The magnetic-field strength as a function of the distance from the Penning trap to the ion detector (solid line). The dashed line indicates the position of the center of the measurement trap

quadrupolar excitation, as described in Sec. 2.2. The application of a resonant quadrupole rf field for a certain conversion period via quadrupolar excitation converts the magnetron motion into cyclotron motion, which leads to an acceleration along the z-axis. Thus, the time of flight from the trap center to an ion counting detector, such as an MCP or a Channeltron, decreases substantially as demonstrated in Fig. 2.7. In this example, the mean time of flight decreases from $88\,\mu$s to $67\,\mu$s if the magnetron motion of the $^{133}\text{Cs}^+$ ions is converted to the cyclotron motion by application of the quadrupolar excitation. The time-of-flight measurement between the ejection from the trap and the ion detection is repeated for certain excitation frequencies ν_{RF}. A scanning region of appropriate range around the expected cyclotron frequency results in a resonance curve such as of Fig. 2.8. The minimum flight time is measured for $\nu_{RF} = \omega_c/2\pi = \nu_c$, which is reflected by the global minimum in the obtained resonance curve. A function [Kon95] which corresponds to the Fourier transformation of the quadrupolar excitation pulse with the excitation period T_{RF} can be fitted to the data to precisely determine the resonance frequency ν_c. The resolving power R of the ToF-ICR technique is proportional to the duration of the quadrupolar excitation pulse T_{RF} [Bol90]

$$R = \frac{\nu_c}{\Delta\nu_c(FWHM)} \approx \frac{\nu_c T_{RF}}{0.8}. \tag{2.20}$$

However, due to damping effects caused by the presence of residual gas atoms, temporal magnetic-field fluctuations [Dro11] and a limited half-life of certain radionuclides the applicable excitation time and, thus, the resolving power, for a given magnetic-field strength of 7 T
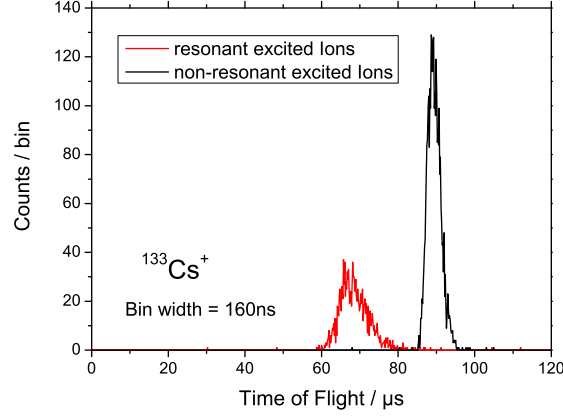
Figure 2.7: The time-of-flight distribution of $^{133}Cs^+$ ions from the ejection of the measurement trap to the ion detector. The time of flight significantly decreases as the ions are resonantly excited and, thus, their magnetron motion is converted into cyclotron motion.
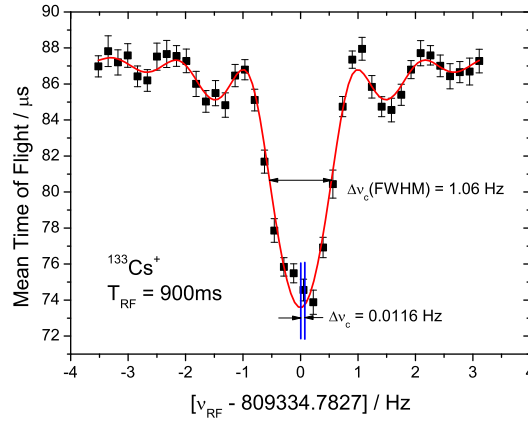
Figure 2.8: Time-of-flight ion cyclotron resonance obtained for $^{133}Cs^+$ with a quadrupole excitation time $T_{RF} = 0.9\,\text{s}$. A fit function (solid line) [Kon95] was applied to the experimental data points (black squares).

used at SHIPTRAP, is practically limited to about 10^6. In order to minimize the statistical uncertainty

$$\left(\frac{\delta m}{m}\right)_{stat} = \frac{a}{R \cdot \sqrt{N_{ion}}} \tag{2.21}$$

of the determined cyclotron frequency, the measurement cycles are repeated several times to maximize the number of detected ions N_{ion}. In Eq. 2.21 a is a dimensionless constant which

was determined in systematic studies of the accuracy of the SHIPTRAP setup to a value of a = 0.79(14) [Cha07].

Since the first application more than 30 years ago [Gra80] the ToF-ICR technique has been modified to improve its resolving power and precision. The Ramsey technique [Geo11] uses two (or more) rectangular pulses separated by a certain waiting time, which results in a gain in precision by a factor of three.

The resolving power can be increased by more than one order of magnitude if the quadrupole rf field is replaced by an octupole field [Eli07]. Since the resolving power is proportional to the cyclotron frequency ω_c and, thus, according to Eq. 2.7 to the charge state q of the investigated ion, the use of highly charged ions [Gal12] is favourable. However, in order to produce highly charged ions an additional preparation step, i.e. charge breeding, is required which lowers the overall efficiency of setup.

A novel mass-measurement technique developed at SHIPTRAP that determines the eigenfrequencies via projection of the ion motion in the Penning trap onto a position-sensitive detector is presented in detail in Sec. 5.2.1. Furthermore, in Sec. 5.2.2 an overview of the non-destructive Fourier-Transform Ion-Cyclotron-Resonance (FT-ICR) technique is given.

Chapter 3

The SHIPTRAP setup

The Penning trap mass spectrometer SHIPTRAP is located at the GSI Helmholtzzentrum für Schwerionenforschung GmbH at Darmstadt [GSI]. For online measurements performed with exotic radionuclides it is connected to the **S**eparator for **H**eavy **I**on reaction **P**roducts (SHIP) [Hof00]. This unique combination enables high-precision Penning trap mass measurements on transfermium elements. A schematic of the velocity filter is given in Fig. 3.1 and the setup is described in Sec. 3.1. An overview of the Penning trap mass spectrometer SHIPTRAP is givien in Fig. 3.2. The main devices of the SHIPTRAP setup, i.e. the buffer-gas stopping cell, the RFQ buncher, and the Penning traps will be briefly described in the subsequent sections.

Figure 3.1: Schematic overview of the velocity filter SHIP.
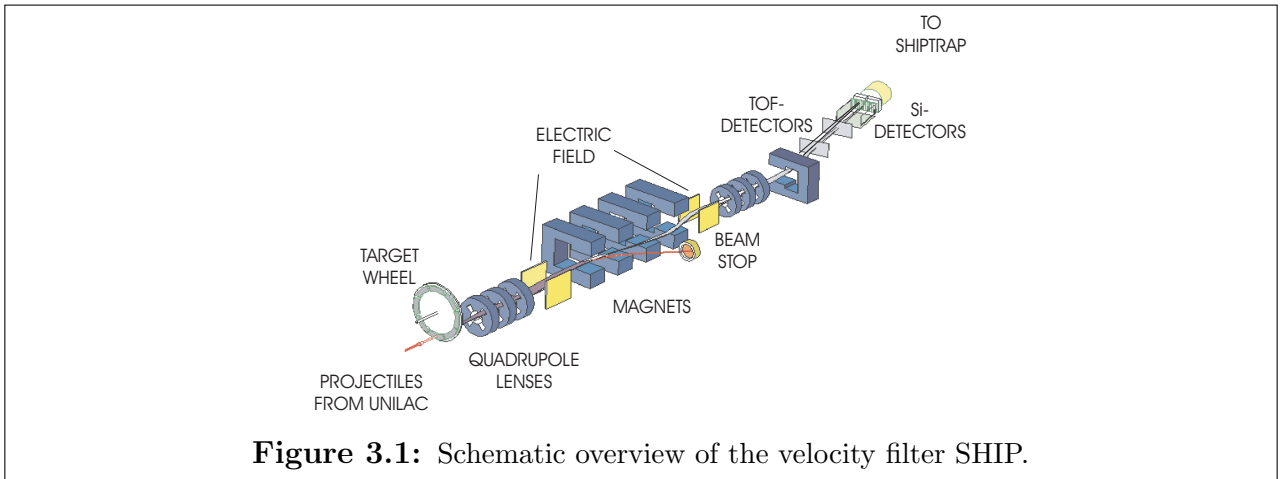
3.1 The velocity filter SHIP

At the velocity filter SHIP (see Fig. 3.1) exotic nuclei are created via fusion-evaporation reactions. Therefore, targets consisting of thin metallic foils ($<1\,\mathrm{mg/cm^2}$) which are placed on a rotating wheel are irradiated with a projectile beam delivered by the **UNI**versal **L**inear **AC**celerator (UNILAC) [Yar07] with typical energies of 3-6 MeV per nucleon. The UNILAC

delivers highly charged ions ($q = 10$ for ^{70}Ni) with beam currents up to $3\,\mathrm{p\mu A}$. The absolute kinetic energy of the primary beam can be tuned with an accuracy of $\pm 0.01\,\mathrm{MeV/u}$ to overcome the Coulomb barrier between the projectile and the target nucleus. The created excited compound nucleus is cooled by emission of neutrons. Other decay modes, like the emission of protons or alpha particles from the nucleus, are suppressed due to the dominance of neutrons in the compound nucleus. The evaporation residues which leave the target due to scattering as a divergent beam are focussed by a magnetic lens realized by three magnetic quadrupoles with a maximum gradient of $9.5\,\mathrm{T/m}$. Due to a combination of forces created by electrical and magnetic fields (Wienfilter principle) only particles having a certain velocity are transmitted through SHIP. The fast projectiles are separated from the reaction products with kinetic energies of several hundreds of keV per nucleon within 1-2 μs. In order to maximise the transmission of the setup another magnetic lens is placed behind the velocity filter. The background on the detector is reduced by a 7.5° bending dipole magnet that deflects projectiles with low charge states and high velocities or projectiles at similar velocities as the reaction products, which manage to pass the velocity filter. The beam spot in the focal plane has a dimension of 50x30 mm^2. In case the velocity filter is not connected to SHIPTRAP the created isotopes, usually superheavy elements which decay by emission of alpha particles, are identified by an array of seven identical 16-strip silicon detectors and three germanium detectors. For further details see [Hof00].

The velocity filter SHIP is in use since the 1970's. Over the years numerous experiments have been performed which revealed insight on the nuclear structure of superheavy elements [Den00, Hof00]. Furthermore, the elements with the proton number $Z = 107\text{-}112$ have been first discovered and investigated at SHIP by means of decay spectroscopy [Mun81, Mun84, Mun88, Oga99, Hof02].

3.2   The gas stopping cell and extraction RFQ

Reaction products from the velocity filter SHIP have kinetic energies of tens of MeV depending on the performed fusion-evaporation reaction. In order to perform Penning-trap mass measurements the kinetic energy of the reaction products needs to be efficiently reduced by several orders of magnitude to the eV range. The ions lose the largest fraction of their kinetic energy in the buffer-gas stopping cell [Neu04]. A CAD model of the gas cell is presented in Fig. 3.3. The reaction products from SHIP enter the gas cell through the entrance window consisting of a metallic foil of a few μm thickness. As they pass the foil they lose 90 % of their kinetic energy due to collisions with the atoms of the foil. The residual kinetic energy is removed by collisions with buffer-gas atoms of ultra-pure helium that fills the gas cell. The thermalized ions are then guided by a homogeneous electrostatic field supplied by the DC cage to the RF funnel. By superposition of DC- and RF-voltage the RF funnel repels the ions from the electrode structure and guides them towards the nozzle. The extraction nozzle serves as a pumping barrier between the buffer-gas filled cell at a pressure of approximately 60 mbar and the extraction
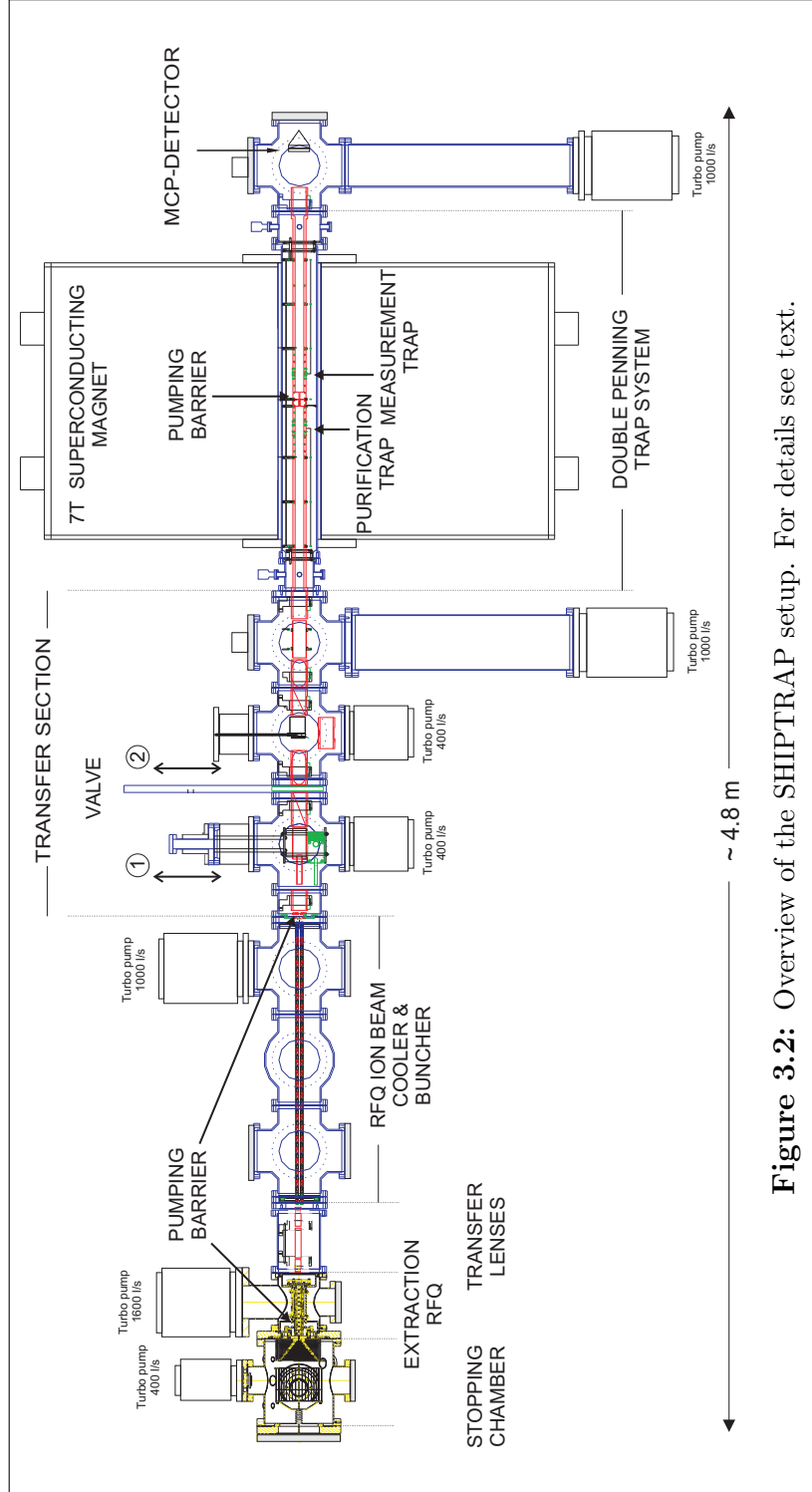
Figure 3.2: Overview of the SHIPTRAP setup. For details see text.

RFQ chamber at a pressure of $1 \cdot 10^{-2}$ mbar. In the nozzle a supersonic gas jet with velocities of about 1600 m/s is created which extracts the ions from the gas cell into the extraction RFQ.

Figure 3.3: CAD model of the buffer-gas stopping cell. Figure taken from [Neu04].
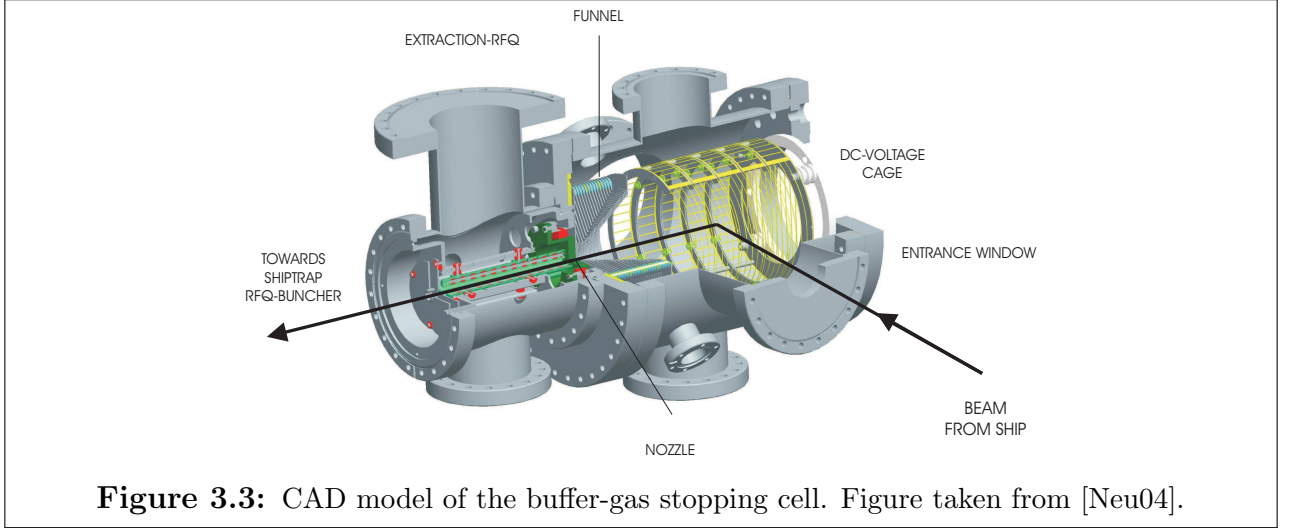
The extraction RFQ is a linear Paul trap [Pau90] which confines the ions radially and guides them further downstream by superposition of a DC gradient with a rf quadrupole field while the buffer gas introduced by the gas jet is removed by a turbomolecular pump. The current gas stopping cell has a stopping and extraction efficiency of 12 % [Eli07a]. Recently, a second-generation gas cell with a higher stopping and extraction efficiency has been set up. A detailed presentation of the principle of this new gas cell as well as the results of the efficiency and extraction time measurements performed in offline experiments, utilizing a ^{219}Rn ion source, is given in the thesis article III.

3.3   The RFQ buncher

The thermalized ions are ejected from the extraction RFQ as a continuous beam. For an efficient capture of the ions in the Penning trap it is inevitable to store and cool them in a preceding trapping device, i.e. the RFQ buncher. The RFQ buncher is a linear Paul trap [Pau90] with a length of one meter. It consists of four stainless steel rods with a diameter of $9\,\text{mm}$ each segmented into 34 segments. The distance between opposing rods is $2r_0 = 7.8\,\text{mm}$. A sketch of the RFQ buncher is given in Fig. 3.4. The buncher is operated at a helium buffer-gas pressure of approximately $5{\cdot}10^{-3}\,\text{mbar}$. The rf quadrupole field with a frequency of $721\,\text{kHz}$ confines the ions in radial dimension. In addition, a superimposed DC field with a potential minimum (see Fig. 3.4) traps the ions in axial dimension. The DC voltages gradually decreases from $2\,\text{V}$ applied to the first segment to -12 V applied to segment 33 followed by a DC potential of $2\,\text{V}$ at the last segment.

Due to collisions with helium buffer-gas atoms, the kinetic energy of the ions decreases and, thus, the ions approach the potential minimum. The cooling time in the buncher is on the order a few tens of milliseconds. The ions are ejected from the buncher by pulsing the last segment from $2\,\text{V}$ down to -70 V. The phase space and, thus, the temporal width of the ejected ion
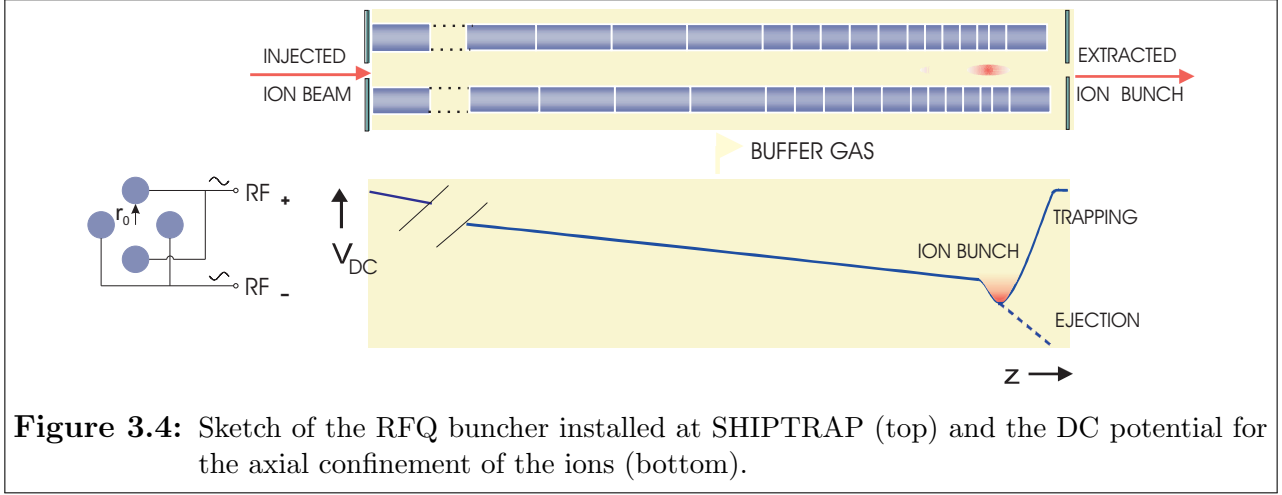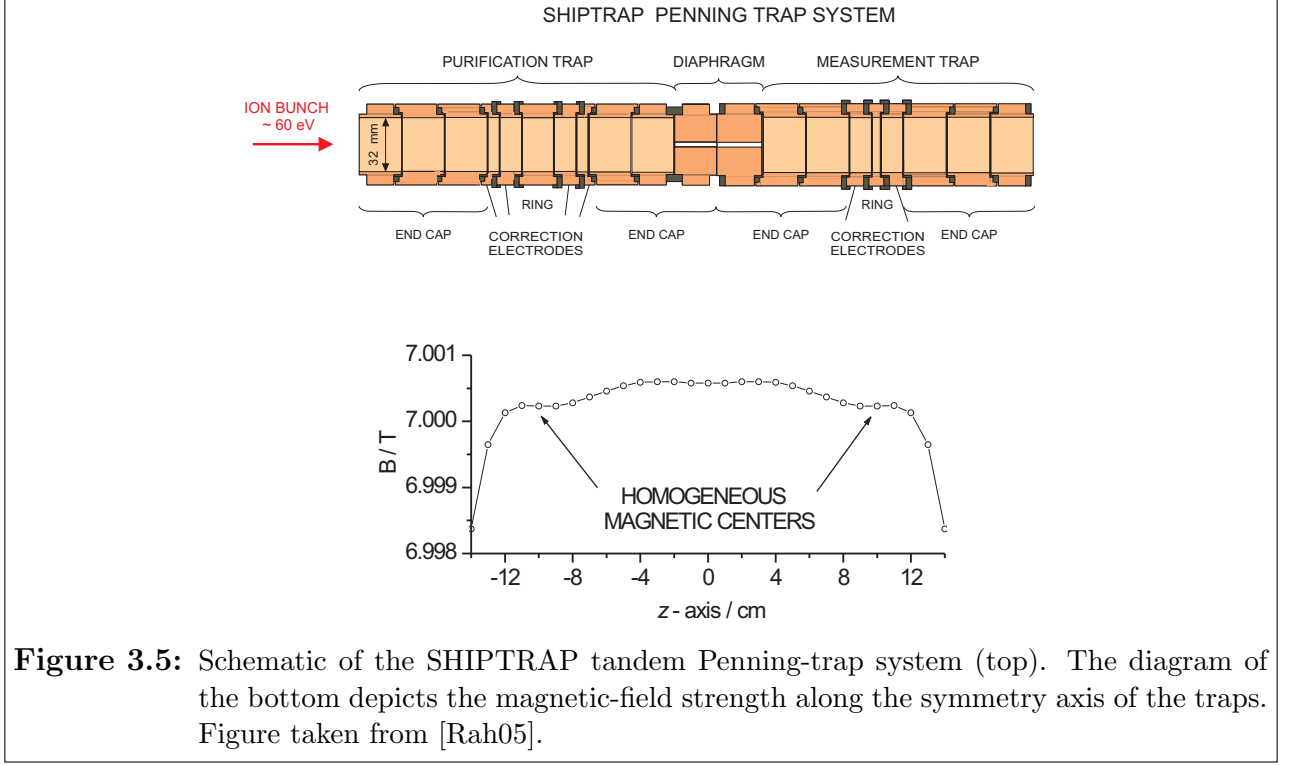
Figure 3.4: Sketch of the RFQ buncher installed at SHIPTRAP (top) and the DC potential for the axial confinement of the ions (bottom).

bunch can be further reduced by switching the segment 31 in front of the potential minimum from -11 V to 60 V. In this configuration a bunch width of 500 ns [Rod03] can be obtained. A detailed description of the performance of the RFQ buncher currently operated at SHIPTRAP can be found in [Rod03].
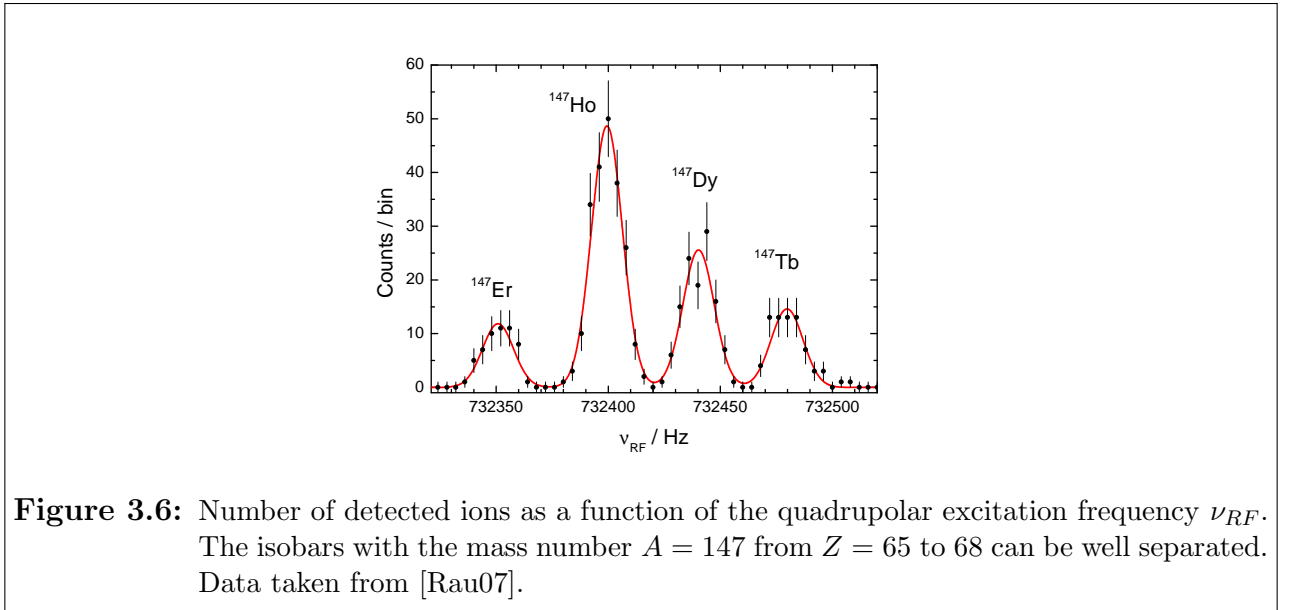
Recently, a second-generation RFQ quadrupole system has been developed to increase the transmission from currently 35 % to approximately 90 % [Hae11]. The new RFQ system is a three-stage device that consists of an rf cooler, a mass analyzer, and an RFQ buncher. The rf cooler utilizes buffer-gas cooling at a pressure of $8 \cdot 10^{-2}$ mbar to reduce the energy of the incoming ions to 0.0125 eV and acts as a preparatory stage for the mass analyzer. The mass analyzer has a resolving power of 130 at full transmission which can be increased to 500 for 20 % transmission efficiency. Therefore, the mass analyzer can be utilized to separate the incoming ions on an isotopic level. In the final stage, i.e. the RF buncher, the ions are accumulated and extracted in bunches with a peak width of about 100 ns.

3.4 The Penning trap system

The cooled ion bunches are injected into the tandem Penning-trap electrode system which is situated in a 7 T superconducting magnet (MAGNEX SCIENTIFIC MRBR 7.0/160/AS). Both Penning traps are cylindrical. The second Penning trap is orthogonalized [Gab89]. In order to minimize the distortion of the magnetic field of the solenoid the trap electrodes are made out of material with small magnetic susceptibility, i.e. gold plated oxygen-free high-conductivity (OFHC) copper and alumina used for electrical insulation. A schematic overview of the Penning traps is given in Fig. 3.5. The first Penning trap, called preparation or purification trap (PT), has a length of 212 mm. It consists of three pairs of endcap electrodes, two pairs of twofold segmented correction electrodes and an eightfold segmented ring electrode. For typical operating conditions a resolving power of 10^5 can be obtained. By use of the buffer-gas cooling technique [Sav91], at a helium pressure of $5 \cdot 10^{-5}$ mbar, isobaric separation can be performed

Figure 3.5: Schematic of the SHIPTRAP tandem Penning-trap system (top). The diagram of
the bottom depicts the magnetic-field strength along the symmetry axis of the traps.
Figure taken from [Rah05].

as shown in Fig. 3.6.

Figure 3.6: Number of detected ions as a function of the quadrupolar excitation frequency ν_{RF}.
The isobars with the mass number $A = 147$ from $Z = 65$ to 68 can be well separated.
Data taken from [Rau07].

After passing an orifice with an open diameter of $1.5\,\text{mm}$ and a length of $52\,\text{mm}$ an isobaric
pure sample is injected into the second Penning trap, the measurement trap (MT), in which

mass measurements with the ToF-ICR technique (see Sec. 2.3) or the PI-ICR technique (see Sec. 5.2.1) are performed. Due to differential pumping a pressure of $1 \cdot 10^{-9}$ mbar was measured in the vicinity of the MCP detector behind the magnet. According to calculations, the actual pressure in the Penning traps is increased by a factor of 50 [Sai05] compared to the measured value. This results in a pressure of about $5 \cdot 10^{-8}$ mbar in the MT obtained during the operation with buffer gas in the PT. The MT consists of three pairs of endcap electrodes, one pair of twofold segmented correction electrodes and an eightfold segmented ring electrode. The MT has a total length of 185 mm. Due to an increased spatial homogeneity of the magnetic-field strength of the solenoid at the measurement trap, a revolving power of 10^6 can be obtained which is sufficient to separate ions in different isomeric states with an energy difference down to 200 keV in the mass region around $Z \approx 200$.

Chapter 4

Mass measurements at SHIPTRAP

The scientific focus of the Penning trap experiment SHIPTRAP is high-precision mass measurements of exotic nuclides in the region of the heaviest elements. In online experiments in 2008, 2009, 2010, and 2011 the masses of the isotopes $^{252-255}$No and ^{255,256}Lr were measured. The experimental results are briefly discussed in Sec. 4.1. The impact of these first direct mass measurements on the nuclear structure around the neutron number $N = 152$ is described in thesis article I.

The campaign for the identification of suitable candidates for the observation of the neutrinoless double-electron capture in large scale experiments started in 2011 and is still ongoing. To this end the mass difference ($Q_{\epsilon\epsilon}$-value) between the mother and the daughter nuclide of the yet unobserved neutrinoless double-electron capture has been determined with uncertainties of only few hundreds of eV/c^2. Up to now the $Q_{\epsilon\epsilon}$-values of 12 isotope pairs were measured to check for a resonant enhancement in the neutrinoless double-electron capture decay rate. The investigation of the possible candidate ^{180}W is presented in thesis article II. A review of the investigated candidates at SHIPTRAP is given in Sec. 4.2.

4.1 Mass measurements in the region of the heaviest elements

The production and investigation of transuranium elements goes back to the 1940's. Until now elements with proton numbers up to $Z = 118$ [Oga06] have been created. The motivation for the ongoing quest for superheavy elements (SHE) with even larger proton numbers is the prospect of a long-lived spherical doubly magic nuclide that forms the so-called island of stability. Due to the closure of the proton and neutron shells the binding energies of the nuclide at the island of stability is substantially increased which results in a longer half-live. The existence of a doubly-magic SHE nucleus was envisaged in the late 1960's by G. T. Seaborg. In the following years several theoretical models using the liquid drop model with the Strutinsky shell-correction method [Str67] agreed upon the magic proton number $Z = 114$ [Mye66, Mel67, Nil69, Mos69]. Nowadays, theoretical mass models do not agree on the prediction of the proton number for the

closed shell configuration. The liquid drop models predict spherical shell closure at 114 [Mye96] while Hartree-Fock calculations indicate larger proton numbers, i.e. $Z = 120$ [Gup97] or $Z = 126$ [Cwi96]. Most of the current models agree that the neutron shell closure is obtained at $N = 184$.

Precision mass measurements in the vicinity of superheavy elements are crucial to benchmark the quality of the nuclear shell models since the measured mass values directly provide the binding energies. To this end, the masses of the isotopes $^{252-255}$No and ^{255,256}Lr have been measured at SHIPTRAP. These experiments mark the first direct mass measurements of transfermium elements which resulted in an unambiguous determination of the deformed neutron shell closure at the neutron number $N = 152$. The nuclei have been produced in fusion-evaporation reactions by irradiation of lead and bismuth targets with a ^{48}Ca beam at an energy of about 4.55 MeV per nucleon. Further details of the fusion-evaporation reactions are given in Tab. 4.1.

Table 4.1: Fusion-evaporation reactions for the production of the isotopes $^{252-255}$No and ^{255,256}Lr with a ^{48}Ca beam at an energy of 4.55 MeV/u (second column), corresponding reaction cross section σ (third column) and count rate on the Channeltron detector behind the SHIPTRAP magnet(last column).

| Isotope	Reaction	σ / nbarn	detected counts / h
^{252}No	^{206}Pb(^{48}Ca,2n)^{252}No	400	3
^{253}No	^{207}Pb(^{48}Ca,2n)^{253}No	1800	15
^{254}No	^{208}Pb(^{48}Ca,2n)^{254}No	2000	17
^{255}No	^{208}Pb(^{48}Ca,1n)^{255}No	140	1
^{255}Lr	^{209}Bi(^{48}Ca,2n)^{255}Lr	300	3
^{256}Lr	^{209}Bi(^{48}Ca,1n)^{256}Lr	60	0.5

After preparation of the ions of interest in the gas stopping cell and the RFQ buncher, the ion bunch was isobarically cleaned via buffer-gas cooling (see Sec. 2.2). In this mass region and for the employed so-called cold fusion reactions the one- or two-neutron evaporation channels are dominant. Compared to the nuclide of interest the cross section for other evaporation channels is significantly lower and unwanted isobars are not an issue. However, due to impurities of the helium buffer-gas in the gas cell, the RFQ buncher and the PT, there is a certain chance of charge-exchange reactions. After preparation of an isobarically pure sample the masses of the nobelium and lawrencium ions were measured with the ToF-ICR technique (see Sec. 2.3).

The low reaction cross sections (4.1) and the efficiency of the SHIPTRAP setup (Sec. 5.1) resulted in count rates below one per minute on the Channeltron detector. On average one ^{256}Lr ion was detected every two hours which resulted in a measurement duration of 4 days to acquire a time-of-flight resonance with 48 ions. In order to realize such long-term mass measurements with a reasonable uncertainty, a pressure of $5 \cdot 10^{-8}$ mbar in the measurement trap and an active temperature stabilization of the magnetic field [Dro11] are crucial.

From the mass values m the mass excess (in units of keV as usual in the literature [Aud03])

$$ME = [m - A \cdot u] \cdot c^2 \tag{4.1}$$

is extracted. Here, A is the atomic mass number and c is the speed of light. A comparison between the experimental results and the mass excess values of the atomic mass evaluation 2003 [Aud03] [2] is given in Fig. 4.1. The uncertainties of the mass excess values of the investigated
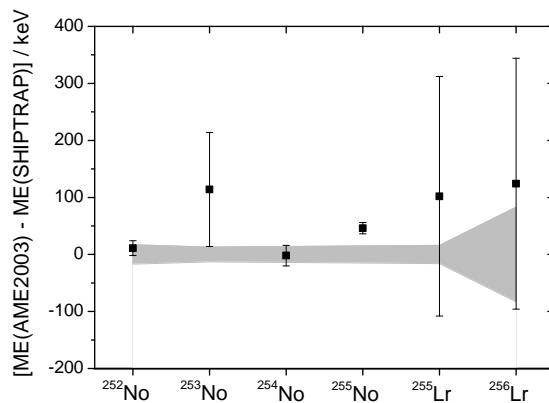
Figure 4.1: Difference between the mass excess values of $^{252-255}$No and ^{255,256}Lr of the atomic mass evaluation 2003 [Aud03] (black squares) and the present experimental results. The uncertainties of the measured mass excess values are indicated by the gray band.

nuclides, which were previously obtained from alpha-decay chains to known nuclei or from systematic trends, were substantially reduced to approximately $14\,\text{keV}$. The low statistics of the time-of-flight resonance of ^{256}Lr in addition to the short excitation time $T_{RF} = 200\,\text{ms}$ results in a larger mass uncertainty of $83\,\text{keV}$ which still falls below the uncertainty of the mass excess value given in the atomic mass evaluation 2003 [Aud03].

A quantitative investigation of the nuclear subshell closure in the range of $N = 148$ - 157 by means of the neutron shell-gap parameter

$$\delta_{2n}(N, Z) = S_{2n}(N, Z) - S_{2n}(N-2, Z) = -2ME(N, Z) + ME(N-2, Z) + ME(N+2, Z) \tag{4.2}$$

was performed in thesis article I. The shell gap parameter is the difference between the two-neutron separation energies of two isotopes differing by two neutrons. The two-neutron separation energy $S_{2n}(N, Z)$ corresponds to the energy necessary to remove two neutrons from the nucleus. The results revealed a closure of the deformed neutron shell at $N = 152$. The shell gap parameter derived from the experimental results was compared with a selection of theoretical nuclear models, i.e. a microscopic-macroscopic global finite-range droplet model [Moe95],

---

[2]The experimental values are compared to an outdated version of the atomic mass evaluation since the results of these experiments are now incorporated in the latest version, the atomic mass evaluation 2012.

a microscopic-macroscopic model optimized for heavy nuclei within $Z = 102$ - 109 [Mun03], a self-consistent mean-field model using the Skyrme-Hartree-Fock effective interaction SkM* [Rut97] and a relativistic mean-field model using the effective interaction TW-99 [Zha05][3]. In Fig. 4.2 the mass excess values of the atomic mass evaluation 2012 which includes the recent experimental results [Wan12] are compared to the predictions given by the theoretical models mentioned above [Moe95, Rut97, Mun03, Zha05]. In general a better agreement of the
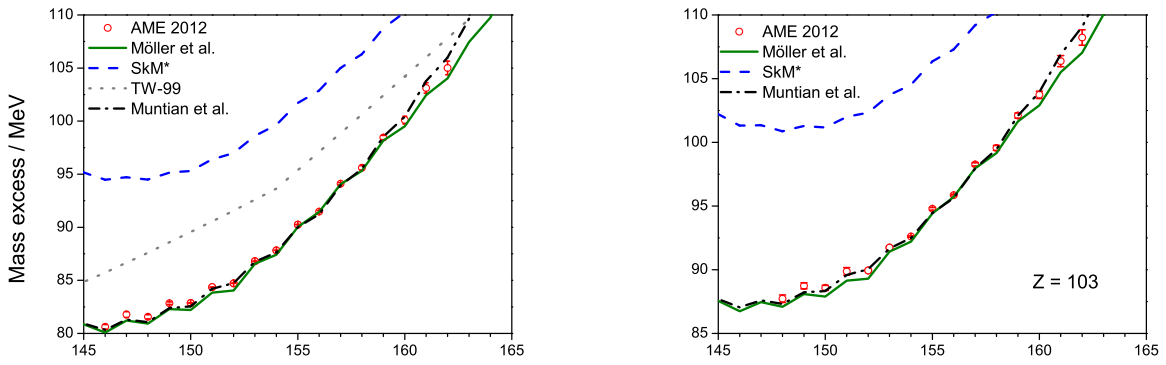
Figure 4.2: The mass excess of nobelium (left) and lawrencium (right) isotopes. The data points, obtained from the atomic mass evaluation 2012 [Wan12], are based on experimental results and extrapolated values from systematic trends. The data points are compared to a selection of theoretical models [Moe95, Rut97, Mun03, Zha05]. For details see text.

experimental values is obtained with the results of the microscopic-macroscopic mass models than the relativistic mean-field model and the self-consistent mean-field model. However, a comparison of Fig. 4.2 with Fig. 3 of thesis article I indicates that the agreement of the predicted mass excess with the experimental results does not necessarily imply a good agreement of the predicted strength of the shell-gap parameter. In Fig. 4.2 the mass excess predicted by the self-consistent mean-field model with Skyrme-Hartree-Fock effective interaction SkM* [Rut97] differs by several MeV from the experimental results however, reproduces the trend of the neutron shell-gap parameter correctly. The nuclear models utilizing the FRDM ansatz [Moe95, Mun03] reproduce the strength of the shell-gap parameter within the the uncertainties of the experimental results. Furthermore, the microscopic-macroscopic mass model optimized for very heavy elements [Mun03] reproduces the correct mass excess value more accurately than the global FRDM model by Möller et al. However, the difference between theoretical predictions and experimental values [Aud03] exceeds a few hundreds of keV for nuclei with $N < 150$ and $N < 152$ for nobelium and lawrencium, respectively.

The relevance of direct mass measurements in the region of the heaviest elements in order to benchmark nuclear models becomes in particular evident for the relativistic mean-field model

---

[3]From this particular mass model data was only available for even-even nuclei.

using the effective interaction TW-99 [Zha05]. In Fig. 4.2 (left) the predicted mass excess deviates by several MeV from the experimental results. Furthermore, this model predicted deformed neutron shell closure at the neutron number $N = 154$ which indicates an incorrect parametrization of the model parameters.

The investigation of the deformed neutron shell closure for different proton numbers in further mass measurements would be beneficial to investigate the dependency of the strength of the neutron shell gap parameter at the deformed neutron shell closure on the proton number. Furthermore, the first direct confirmation of the deformed neutron shell closure at $N = 162$ by means of high-precision mass spectrometry would be beneficial to improve the understanding of the nuclear structure of superheavy elements.

4.2 $Q_{\epsilon\epsilon}$-value measurements for the assessment of nuclides that are candidates for the neutrinoless double-electron capture
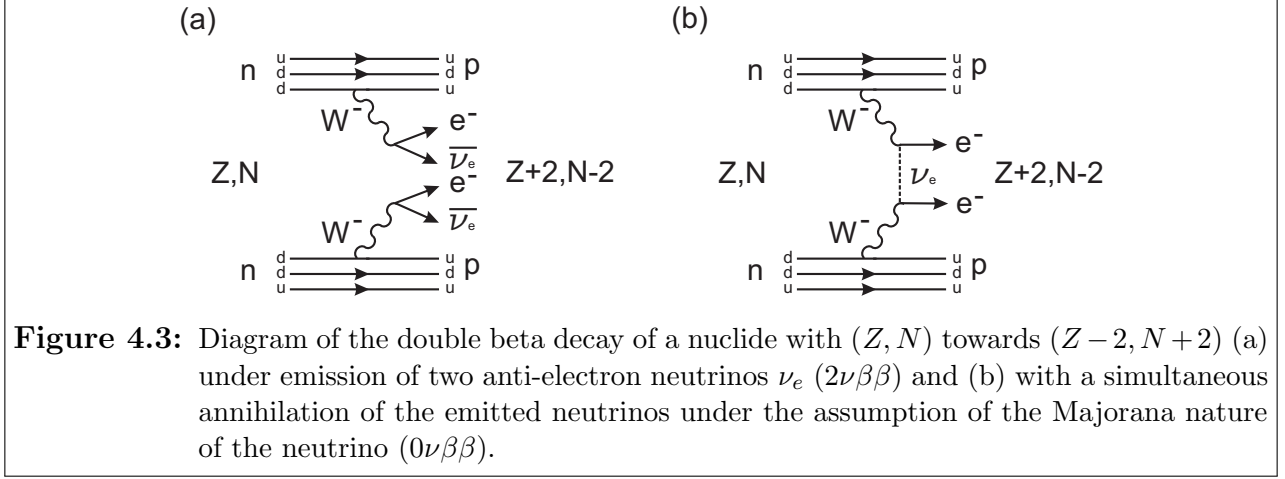
In the beginning of the 20th century the continuous energy spectrum of the β^- decay, by then considered to be a two-body process, which indicated a violation of the conservation of energy, was one of the most pressing mysteries in particle physics. In 1930 Wolfgang Pauli first proposed the existence of another particle involved in the decay making it a three-body-event [Pau77]. In 1933 Enrico Fermi postulated the existence of the electron neutrino ν_e having an extremely small reaction cross section with known particles [Fer34]. In fact, the first indirect experimental proof of its existence by the detection of the reaction products of the inverse beta decay involving the anti-electron neutrino $\bar{\nu}_e$

$$\bar{\nu}_e + p \rightarrow e^+ + n. \tag{4.3}$$

succeeded 23 years later [Rei56]. Since then, the existence of the muon neutrino ν_μ [Ste62] and the tau neutrino ν_T [Kod01] were confirmed.

In the 1960's neutrino oscillations were predicted [Pon68] giving direct evidence of a non-vanishing mass value of the neutrinos. In 2001 the Sudbury Neutrino observatory gave first unambiguous evidence for the existence of neutrino oscillations in the sun [Ahm01]. However, the absolute mass value is still unknown. From β-spectrometry experiments investigating the beta decay of tritium an upper mass limit of $2.2\,\mathrm{eV}/c^2$ [Lob03] was found. Currently the KArlsruhe TRitium Neutrino (KATRIN) [Wol10] large scale electrostatic spectrometer is set up to determine the neutrino mass providing a lower mass limit of $0.2\,\mathrm{eV}/c^2$.

Another yet theoretical approach is the determination of the neutrino mass via observation of the neutrinoless double beta decay ($0\nu\beta\beta$). In comparison to the double beta decay which occurs under emission of two anti-electron neutrinos ($2\nu\beta\beta$) (see Fig. 4.3 (a)) two neutrinos created by the process annihilate in the neutrinoless double beta decay (see Fig. 4.3 (b)). The observation of the neutrinoless double beta decay implies the Majorana nature of the neutrino meaning that it is its own antiparticle. Furthermore, this process results in a violation of the

Figure 4.3: Diagram of the double beta decay of a nuclide with (Z, N) towards $(Z - 2, N + 2)$ (a) under emission of two anti-electron neutrinos ν_e ($2\nu\beta\beta$) and (b) with a simultaneous annihilation of the emitted neutrinos under the assumption of the Majorana nature of the neutrino ($0\nu\beta\beta$).

lepton conservation which would indicate physics beyond the standard model. Currently, there are numerous large scale experiments either taking data [Ago13, Avi08, Ack11] or being commissioned [Arn10, Gol13]. The Heidelberg-Moscow experiment claimed first observation of the neutrinoless double beta decay in ^{76}Ge with a half-live of $2.23^{+0.44}_{-0.31} \cdot 10^{25}$ years [Kla06]. However, due to the low statistics the results are controversially discussed within the community.

Another approach to determine whether the neutrino is a Majorana particle is the observation
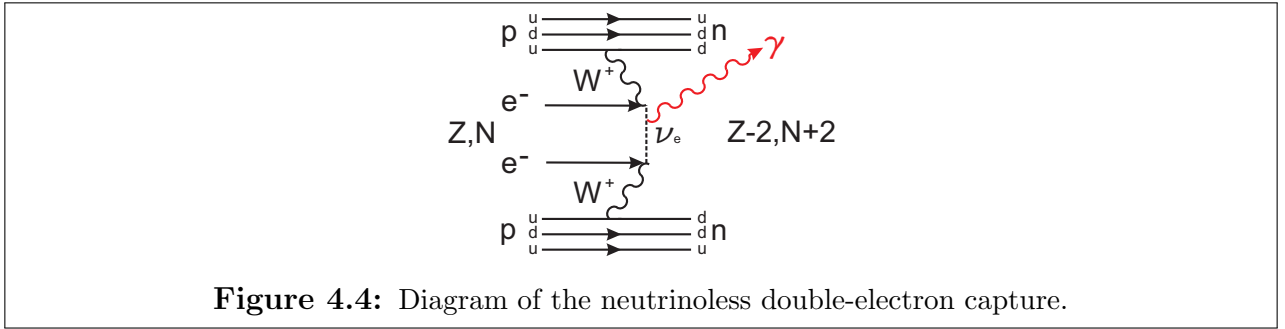
Figure 4.4: Diagram of the neutrinoless double-electron capture.

of neutrinoless double-electron capture (see Fig. 4.4) which offers several advantages in comparison to the neutrinoless double β decay. The excess energy of the daughter nucleus is carried away by a monoenergetic γ photon which can be used as a coincidence trigger to suppress any random background during the measurement of X-rays and/or Auger electrons due to the capture of atomic shell electrons by the nucleus. The large transmission of the emitted long-ranged gamma photon reduces the chance of absorption by the surrounding material. This possibility to spatially separate the source from the detector allows the usage of a different material for the source than for the detector, typically Ge detector, which gives access to a variety of possible candidates to study the neutrinoless double-electron capture.

The expected half-life of neutrinoless double-electron capture ($0\nu\epsilon\epsilon$) is on the order of 10^{30}years (for an effective neutrino mass of $1\,\text{eV}$) which exceeds the half-life of the $0\nu\beta\beta$ decay by several orders of magnitude. However, according to [Ber83, Suj04] the rate of neutrinoless double-

electron capture process

$$\lambda_{\epsilon\epsilon} = |V_{\epsilon\epsilon}|^2 \frac{\Gamma_{2h}}{\Delta^2 + \Gamma_{2h}^2/4} \qquad (4.4)$$

is resonantly enhanced if the mother and the daughter nuclide are degenerate in energy. In Eq. 4.4 $|V_{\epsilon\epsilon}|$ is the nuclear matrix element [Ber83], Γ_{2h} is the sum of widths of the double-electron hole and the nuclear excited state in the daughter nuclide and Δ is the degeneracy parameter

$$\Delta = Q_{\epsilon\epsilon} - B_{2h} - E_\gamma. \qquad (4.5)$$

Here, $Q_{\epsilon\epsilon}$ is the mass difference between the mother and the daughter nuclide, B_{2h} is the energy of the double-electron hole in the atomic shell of the daughter nuclide and E_γ equals the energy of the nuclear excited state in the daughter nuclide. The nuclear matrix element is larger if the spin and parity is identical for mother and daughter nuclide. Thus, the ground-state to ground-state transitions of the possible candidates for neutrinoless double-electron capture, ^{152}Gd/^{152}Sm, ^{164}Er/^{164}Dy and ^{180}W/^{180}Hf, are expected to have a larger decay rate. A value between 7.0 and 7.4 for the nuclear matrix element $|V_{\epsilon\epsilon}|$ was calculated for the transition ^{152}Gd/^{152}Sm [Eli11].
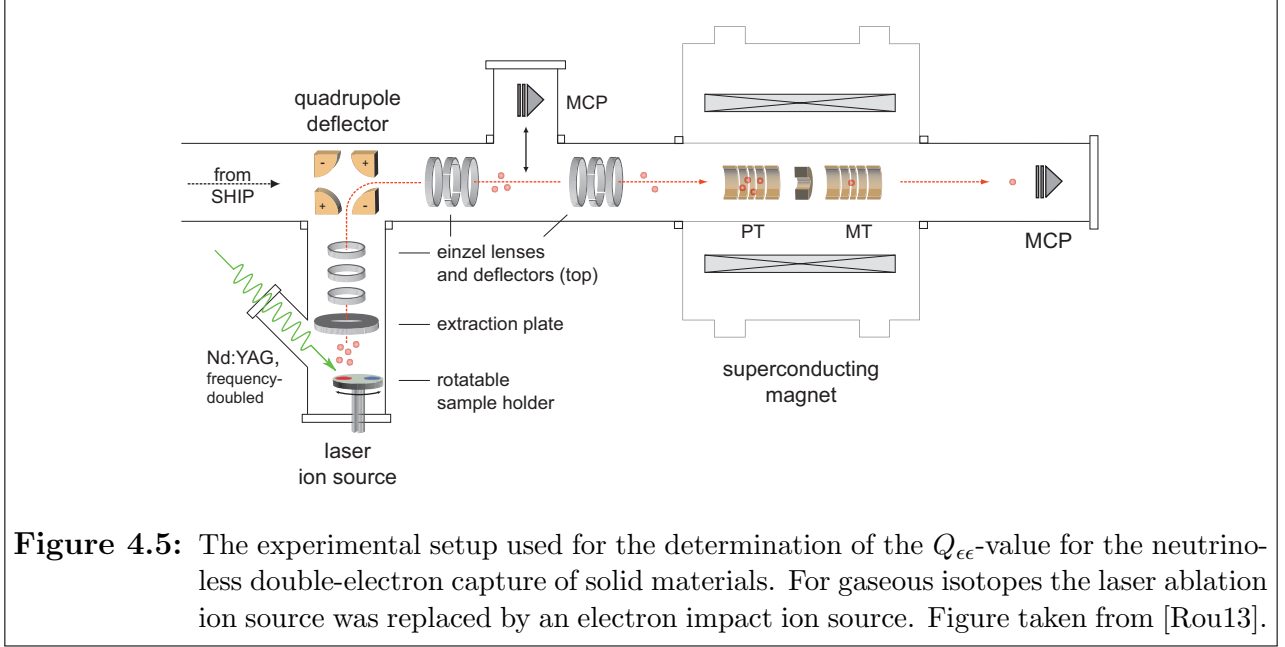The sum of the widths of the double-electron hole and the nuclear excited state Γ_{2h} is on the order of eV. However, the uncertainty of the mass difference between the mother and daughter nuclides deduced from [Aud03] was on the order of several keV which prohibited a conclusive statement whether the candidate fulfils the resonance condition. Due to advancements in Penning trap mass measurements a determination of the mass difference with an uncertainty of less than $100\,\mathrm{eV}$ [Rou13] is feasible. At SHIPTRAP an extended search for isotopes with a resonant enhancement in the rate of the $0\nu\epsilon\epsilon$ has been performed. A sketch of the measurement setup is given in Fig. 4.5.
Here, the ions of the mother and the daughter nuclide are produced via laser ablation with a frequency doubled Nd:YAG laser at a wavelength of $532\,\mathrm{nm}$. Isotopes that were gaseous at room temperature were ionized with an electron-impact ion source. The ions were guided by ion optics to the tandem Penning trap in which the determination of the cyclotron frequency ν_c has been performed by use of the ToF-ICR Ramsey excitation scheme (see Sec. 2.3). In alternating measurements the cyclotron frequency of the mother and the daughter nuclide, $\nu_c(mother)$ and $\nu_c(daughter)$, respectively was determined from which the $Q_{\epsilon\epsilon}$-value

$$Q_{\epsilon\epsilon} = m_{mother} - m_{daughter} = (m_{daughter} - m_e)(\frac{\nu_c(daughter)}{\nu_c(mother)} - 1) \qquad (4.6)$$

can be calculated. An overview of the investigated nuclides is given in Tab. 4.2.
The degeneracy parameter Δ indicates that neutrinoless double-electron capture of most of the investigated candidates is not resonantly enhanced. However, the ground-state to ground-state transition in ^{152}Gd/^{152}Sm [Eli11] shows a resonant enhancement (i.e. Δ is close to zero). The corresponding half-life is reduced to 10^{26} years for an effective neutrino mass of $1\,\mathrm{eV}$. Due to its low abundance of $0.2\,\%$ an amount of $1.3\,\mathrm{tons}$ of gadolinium with the natural isotopic abundance distribution would be necessary in order to observe one neutrinoless double-electron

Figure 4.5: The experimental setup used for the determination of the $Q_{\epsilon\epsilon}$-value for the neutrino-less double-electron capture of solid materials. For gaseous isotopes the laser ablation ion source was replaced by an electron impact ion source. Figure taken from [Rou13].

Table 4.2: The investigated candidates of the neutrinoless double-electron capture process. The $Q_{\epsilon\epsilon}$-values based on the data taken from [Aud03] are compared to the results of the $Q_{\epsilon\epsilon}$-value measurements performed at SHIPTRAP. The degeneracy parameter Δ indicates whether this transition is resonantly enhanced. More detailed informations can be found in the corresponding references (last column).

$0\nu\epsilon\epsilon$ transition	$Q_{\epsilon\epsilon}^{old}$ / keV	$Q_{\epsilon\epsilon}^{new}$/ keV	Δ/ keV	Reference
^{152}Gd - ^{152}Sm	54.6(3.5)	55.7(0.2)	0.91(0.18)	[Eli11]
^{164}Er - ^{164}Dy	23.3(3.9)	25.07(0.12)	6.81(0.12)	[Eli11a]
^{180}W - ^{180}Hf	144.4(4.5)	143.20(0.27)	11.24(0.27	[Dro12]
^{96}Ru - ^{96}Mo	2718.5(8.2)	2714.51(0.13)	8.92(0.13)	[Eli11b]
^{162}Er - ^{162}Dy	1843.8(3.9)	1846.95(0.30)	38.86(0.3)	[Eli11b]
^{168}Yb - ^{168}Er	1421.7(4.7)	1409.27(0.25)	31.35(0.25)	[Eli11b]
^{102}Pd - ^{102}Ru	1172.9(3.6)	1203.27(0.36)	75.26(0.36)	[Gon11]
^{106}Cd - ^{106}Pd	2770(7)	2775.39(0.1)	42.14(0.13)	[Gon11]
^{144}Sm - ^{144}Nd	1781.2(1.8)	1782.59(0.87)	171.89(0.87)	[Gon11]
^{156}Dy - ^{156}Gd	2012.2(7.4)	2005.95(0.1)	0.04(0.1)	[Eli11c]
^{124}Xe - ^{124}Te	2864.4(2.3)	2856.73(0.09)	1.86(0.15)	[Nes12]
^{136}Ce - ^{136}Ba	2418.9(13)	2378.53(0.27)	$-11.67(0.38)$	[Nes12]

capture event in one year.

A multiple resonance phenomenon was observed for the transition ^{156}Dy/^{156}Gd [Eli11c]. Here, the double-electron capture of electrons in the following configurations are resonantly enhanced: KL_1, KM_1, L_1L_1 and M_1N_3. The calculation of the nuclear matrix element $|V_{\epsilon\epsilon}|$ is difficult in

case the spin and parity changes between mother and daughter nuclides. Therefore, the half life was only calculated for the transition in the configuration of $L_1 L_1$ to $6 \cdot 10^{28}$ years for an effective neutrino mass of $1\,\mathrm{eV}$. In contrast to the transition with the electron configuration $M_1 N_3$ the transition $L_1 L_1$ is not in full resonance. Thus, it can be deduced that the final half life for the neutrinoless double-electron capture of ^{156}Dy is shorter making ^{156}Dy a promising candidates for future experiments for the search of $0\nu\epsilon\epsilon$.

Chapter 5

Future perspectives

Currently the binding energies of the heaviest elements are mainly known from decay spectroscopy, predictions of nuclear models as well as from extrapolations of systematic trends. By measurements of the Q_α-values by means of decay spectroscopy of alpha-decay chains that end in known nuclei the masses of transfermium isotopes with even proton and neutron numbers (even-even nuclides) can be determined with uncertainties on the order of a few tens of keV/c^2. However, odd-even, even-odd and odd-odd isotopes often decay towards excited states whose excitation energies are in most cases not precisely determined which results in increased mass uncertainties. The masses of superheavy elements whose alpha-decay chains end in spontaneous fission can only be determined from systematic trends. Direct mass measurements of transfermium elements create anchorpoints along these decay chains and, thus, improve the accuracy of the isotopes along them.

However, direct high-precision mass measurements on superheavy elements with $Z \geq 104$ are technically challenging due to the low production rates. The next nuclide envisaged to be investigated at SHIPTRAP is ^{257}Rf which has a reaction cross section of approximately $10(1)$ nbarn [Hes97] for the irradiation of a ^{208}Pb target with a ^{50}Ti beam. Considering beam intensities comparable to the nobelium and lawrencium mass measurements utilizing a ^{48}Ca beam, a measurement duration of approximately 16 days would be necessary to perform a mass measurement containing approximately 50 ions with the ToF-ICR method. Even though the magnetic field of the superconducting solenoid is actively stabilized [Dro11] the absolute magnetic-field related uncertainty would be substantial. Therefore, technical advancements of the SHIPTRAP setup that increase the efficiency as well as the sensitivity are inevitable.

A second-generation gas stopping cell (CryoCell) has been built to increase the efficiency of the SHIPTRAP apparatus. The CryoCell was characterized in terms of efficiency and extraction time for several parameters using a ^{219}Rn recoil ion source. The cryogenic gas stopping cell is presented in detail in thesis article III and will be shortly addressed in Sec. 5.1.

Furthermore, the sensitivity of the SHIPTRAP setup has to be increased in order to gain access to the mass region of the superheavy elements facing production cross sections below 1 nbarn and half-lives of less than 1 s. To this end, the phase-imaging ion-cyclotron-resonance technique (PI-ICR) [Eli13, Eli14] was developed at SHIPTRAP. By projection of the ion motion in the

Penning trap onto a position-sensitive detector the eigenfrequencies can be obtained via the phase of the ion motion. The PI-ICR method offers a 25 times faster determination of the cyclotron frequency than the ToF-ICR method. This will gives access to mass measurements of short-lived radionuclides. Furthermore, this method requires less detected ions of interest to measure ν_c with comparable accuracy to the ToF-ICR technique. The PI-ICR technique is presented in Sec. 5.2.1.

Ultimately, the Fourier-transform ion-cyclotron-resonance technique (FT-ICR) [Com74] is planned to be implemented at SHIPTRAP. It allows performing non-destructive mass measurements on a single ion. The image charges induced on the trap electrodes by an ion moving in the Penning trap give access to the revolution frequency and, thus, the eigenfrequencies of the ion of interest. The principles of the FT-ICR technique are presented in Sec. 5.2.2.

5.1   The cryogenic gas stopping cell

In 1950 the first experiments of an isotope separator connected to a particle accelerator were carried out at the Copenhagen cyclotron [Kof51]. In the 1960's the Isotope Separator On-Line (ISOL) technique was developed [Kla65]. In the first ISOL facilities the accelerator beams were stopped in a thick target which was heated to enhance the diffusion of the reaction products out of the target material. In a subsequent step the reaction products were ionized again by a dedicated ion source. This concept is still utilized at the ISOL facilities ISOLDE [Kug00] at CERN and ISAC [Dom00] situated at TRIUMF. At ISOLDE targets of about $50\,\mathrm{g/cm^2}$ are irradiated with a proton beam of up to $1.4\,\mathrm{GeV}$ at an average current of $2.1\,\mu\mathrm{A}$. The ISOL facility ISAC at TRIUMF utilizes targets with a thickness between $10\text{-}30\,\mathrm{g/cm^2}$ due to a lower kinetic energy of the impinging proton beam of $500\,\mathrm{MeV}$ at a current up to $100\,\mu\mathrm{A}$. The targets are heated to temperatures above $2000\,^{\circ}\mathrm{C}$ to decrease the diffusion time. The reaction products are then ionized by a surface ion source, a plasma ion source or a laser ion source depending on the chemical properties of the isotopes of interest. In both facilities the reaction products are reaccelerated to $60\,\mathrm{keV}$. The process time of these facilities is on the order of about $100\,\mathrm{ms}$. However, the large yields of about $10^9\,\mathrm{nuclei/s/\mu A}$ [Dom00] that can be produced give access to Penning trap mass measurements on nuclides with shorter half-lives, such as $^{11}\mathrm{Li}$ ($T_{1/2} = 8.5(2)\,\mathrm{ms}$) [Smi08] or $^{100}\mathrm{Rb}$ ($T_{1/2} = 48(3)\,\mathrm{ms}$) [Man13].

Since its development different concepts of the ISOL technique arose to reduce the duration of the process. For instance, targets with a thickness below the recoil range of the reaction products were used to circumvent the time consuming process of the diffusion of the reaction products out of the target material. After leaving the target the reaction products were stopped in a high-pressure noble-gas environment with an admixture of aerosols. The reaction products, attached to the aerosols, are then extracted by a gas jet through a capillary into an ionization chamber for reionization. Noble gases, like helium or argon, are commonly used as the stopping medium to reduce the probability of neutralization by charge-exchange reactions due to their large ionization potential [Kud01]. In the presence of helium buffer gas the neutralization of

the ion of interest X^+ in the three-body reaction

$$X^+ + e^- + He \Longrightarrow X + He \qquad (5.1)$$

is, besides the molecule formation with residual gas atoms, a major contribution for ion losses in a gas filled environment. Due to the time-dependency of the neutralization rate [Kud01] fast stopping and extraction times are crucial.

By additional guidance of the reaction products in a noble-gas filled atmosphere by electrical fields the transport time can be decreased such that the reaction products survive in a singly charged state. The extracted ions can then be injected directly into the accelerator stage making the reionization by a dedicated ion source obsolete. These Ion Guide Isotope Separator On-Line (IGISOL) systems have been developed in Jyväskylä in the 1980's [Den97].

Due to their chemical and nuclear properties certain isotopes can not be produced with the ISOL technique. A larger variety of elements can be produced by means of in-flight separation. However, due to the momentum conservation of the projectiles the reaction products have large kinetic energies up to a few hundreds of MeV/u in fragmentation reaction. In fusion-evaporation reactions nuclides heavier than the target atoms can be created which have kinetic energies a few hundreds of keV/u.

In order to perform Penning-trap mass measurements the produced ions need to be efficiently decelerated by several orders of magnitude to kinetic energies on the order of electronvolts. The pioneering work on the IGISOL systems led to the developments of buffer-gas stopping cells which are now widely used in nuclear physics [Wad03, Wei05, Wad06, Sav08] and, in particular for high-precision mass spectrometry [Neu04, Pla13]. In gas catchers the energetic particles are decelerated by collisions with atoms of a solid degrader and the buffer gas.

The short half-life of exotic nuclei requires a fast extraction from the gas catcher. Therefore, the extraction of the charged particles from the buffer gas is performed by use of electric fields. Thus, gas stopping cells are equipped with an electrode system for DC gradients of several V/cm. The extraction efficiency is substantially increased by application of a RF/DC guiding field which directs the ions towards the exit hole by, e.g. an RF carpet [Wad03, Sch11] or an RF funnel [Wad03].

At SHIPTRAP, the ions of interest are produced by fusion-evaporation reactions as described in Sec. 3.1. The reaction products with energies of tens of MeV are injected into the gas stopping cell through a thin metallic foil of a few μm thickness. The thickness of the foil was chosen according to simulations using the SRIM code [Zie10], such that the passing ions lose 90 % of their initial kinetic energy. After thermalization in a helium buffer-gas environment the cooled ions are guided by an electrostatic field, provided by the DC cage, towards an electrode structure of conical shape, i.e. the RF funnel, which guides the ions towards the exit nozzle. A supersonic gas jet created by the pressure difference between the stopping chamber and the subsequent vacuum chamber guides the ions through the exit nozzle of *de Laval* type [Jen06]. In the subsequent section, i.e. the extraction RFQ [Pau90], the ions are radially confined and guided downstream, while the buffer gas of the supersonic gas jet is removed by a turbomolecular pump. A CAD model of the first-generation gas stopping cell used at SHIPTRAP is given in Fig. 3.3 of Sec. 3.2.

The efficiency of the SHIPTRAP setup is on the order of a few percent [Dwo10]. The bottle-neck besides the current RFQ buncher with a transmission of approximately 30 % [Rod03] is the gas stopping cell. A major improvement of the efficiency is expected by the development of a second-generation gas stopping cell (CryoCell) [Eli08] to increase the stopping and extraction efficiency of 12 % [Eli07a] of the first-generation gas stopping cell.

In comparison to the first-generation gas cell the CryoCell has a larger stopping volume and a coaxial injection. According to simulations of realistic beam conditions [Dro13], using the SRIM code, the extended stopping volume of the CryoCell increases the stopping efficiency by a factor of two in comparison to the first-generation gas cell.

Furthermore, the CryoCell, and thus the containing buffer gas, is cooled down to 40 K. Under these conditions the impurities of the helium buffer gas (purity 99.9999 %) are not gaseous (except hydrogen). As a result the purity increases, which in turn reduces the chance of neutralization of the ions of interest caused by charge-exchange reactions and molecule formation. In offline measurements performed with a ^{219}Rn recoil ion source extraction efficiencies of 74(3) % were obtained resulting in a gain of a factor of 2.5 compared to the first-generation gas stopping cell which has an extraction efficiency of approximately 30 % [Eli07a]. The product of the measured extraction efficiency of 74(3) % and the stopping efficiency of 90 %, determined by simulations using the SRIM code [Zie10], yields an overall efficiency of the CryoCell of about 67(3) %. This corresponds to an increase by a factor of 5 in comparison to the previous version of the gas stopping cell [Eli07a]. A detailed review of the CryoCell is given in thesis article III.

5.2   New mass measurement techniques

Mass measurements on exotic nuclides, for example superheavy elements, are challenging due to their short half-lives and low production yields. In order to perform these measurements it is favourable to apply a mass measurement technique with highest sensitivity.

With the recent development of the phase-imaging ion-cyclotron-resonance (PI-ICR) technique, which is addressed in Sec. 5.2.1, it is possible to determine the cyclotron frequency ν_c with a given uncertainty in a 25 times shorter measurement period compared to the conventional ToF-ICR method, giving access to mass measurements on exotic nuclei with half-lives well below one second. So far, the PI-ICR technique has been utilized for mass-difference measurements of long-lived or stable nuclides with relative uncertainties below one part per billion [Nes14].

By the implementation of the non-destructive Fourier transform ion-cyclotron-resonance (FT-ICR) technique, which is described in Sec 5.2.2, single-ion mass measurements can be obtained. For nuclei with half-lives of about one second the mass values can be obtained with relative uncertainties around 10^{-8} with only one particle.

5.2.1   The Phase-Imaging Ion-Cyclotron-Resonance technique

The PI-ICR technique [Eli13] utilizes the projection of the ion motion in the Penning trap (see Sec. 2.1) onto a position-sensitive delay-line MCP-detector [Spi01]. Ions that are ejected from the measurement trap towards the detector follow the divergent magnetic-field lines which

results in a magnification of the radial position of the ions inside the measurement trap at the moment of ejection onto the MCP detector. The magnification depends on the distance of the detector to the solenoid. For the PI-ICR technique, a commercial delay-line detector (DLD40 Roentdek GmbH) with an active diameter of 42 mm and a channel diameter of 25 μm has been installed. The position resolution of the detector is 70 μm.
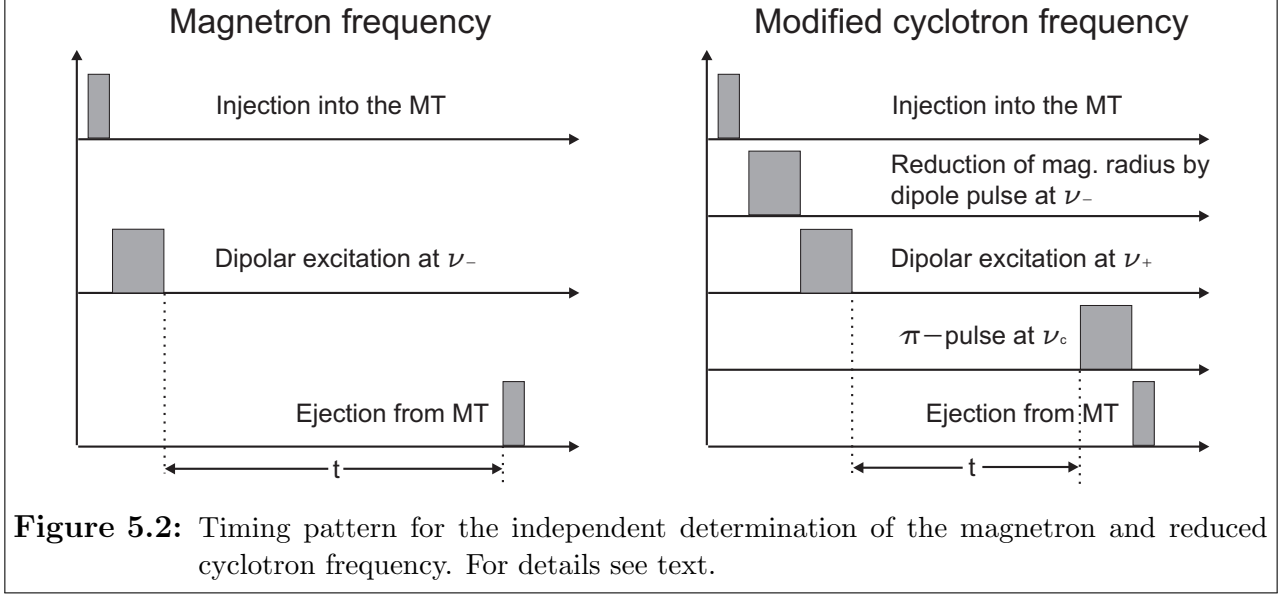
By independent determination of magnetron and reduced cyclotron frequency the cyclotron frequency $\nu_c = \nu_+ + \nu-$ is obtained (see Eq. 2.12). The eigenfrequencies ν_+ and ν_- are determined in a series of three steps as illustrated in Fig. 5.1.
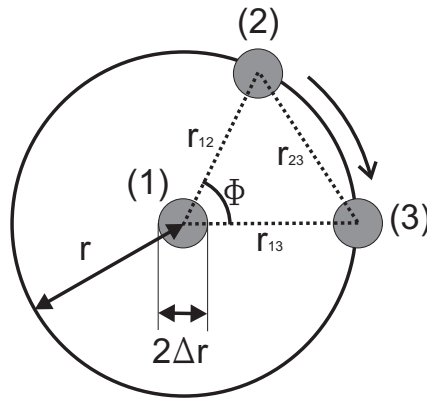
Figure 5.1: Schematic of the measurement principle of the PI-ICR technique for the determination of the eigenfrequencies ν_+ and ν_-. For details see text.

In order to determine the center of the projection of the ion motion in the Penning trap onto the delay-line detector (DLD) the particle is injected into the measurement trap ($t_{in} \approx$ 60 μs) before it is ejected ($t_{ej} = 200\,\mu$s) from the trap without any excitation applied (see (1) in Fig. 5.1). Next, the particle is excited by dipolar excitation (see Sec. 2.1) at either the magnetron or the reduced cyclotron frequency for a period of $t_{dip} \approx 1$ ms, which couples energy into the particle motion. The particle is then detected at a radius r_{12} from the center (see (2) in Fig. 5.1). Finally, the second step is repeated with an additional phase accumulation time t during which the ions are moving in the measurement trap before they are ejected onto the DLD ((3) in Fig. 5.1). The three spots form a triangle with the phase angle Φ (see Fig. 5.1). Knowing the coordinates of the center of the spots on the DLD, Φ can be calculated. From this phase angle and the known phase accumulation time the eigenfrequency of the ion motion is determined (see below). The cyclotron motion has a substantially higher revolution frequency than the magnetron motion (see Tab. 2.1) which increases the spatial distribution of the ion cloud in the Penning trap due to the time-of-flight distribution of the ejected ions between the measurement trap and the detector. In order to avoid an increased uncertainty for the determination of the reduced cyclotron frequency ν_+ due to a broadened spot on the DLD the excitation pattern is extended by two intermediate steps. After the injection of the ion into the the MT the introduced magnetron motion is damped by a dipole pulse at ν_-. In a further step the cyclotron motion is converted to magnetron motion after the phase-accumulation

time passed. A full conversion of the cyclotron motion into magnetron motion is obtained by application of quadrupolar excitation at the cyclotron frequency ν_c for about 2.5 ms, i.e. the so-called π-pulse. The timing patterns for the determination of magnetron and reduced cyclotron frequency are given in Fig. 5.2. The phase angle Φ

Figure 5.2: Timing pattern for the independent determination of the magnetron and reduced cyclotron frequency. For details see text.

$$\Phi_\pm = 2\pi(\nu_\pm t - n_\pm). \tag{5.2}$$

is proportional to the phase accumulation time and the revolution frequency of the ions in the trap. In Eq. 5.2 $n_\pm$ is the number of full revolutions of the magnetron or cyclotron motion the particle performs during the phase accumulation time t. Knowing the phase angles $\Phi_\pm$ the eigenfrequencies $\nu_\pm$ can be determined with

$$\nu_\pm = \frac{\Phi_\pm + 2\pi n_\pm}{2\pi t} \overset{0 \leq \Phi_\pm \leq \pi}{=} \frac{arccos(k) + 2\pi n_\pm}{2\pi t} \overset{\pi < \Phi_\pm < 2\pi}{=} \frac{2\pi(n_\pm + 1) - arccos(k)}{2\pi t}. \tag{5.3}$$

Their corresponding uncertainties follow from

$$\delta\nu_\pm = \frac{\delta k}{2\pi t \sqrt{1 - k^2}} \tag{5.4}$$

where

$$k = (r_{12}^2 + r_{13}^2 - r_{23}^2)/(2r_{12}r_{13}). \tag{5.5}$$

Considering an identical spatial distribution $2\Delta r$ for the three projected spots the uncertainty of the introduced parameter k can calculated with

$$\delta k = \sqrt{2^3(\Delta r)^2 \left[\left(\frac{r_{12}^2 - r_{13}^2 + r_{23}^2}{2r_{13}r_{12}^2} \right)^2 + \left(\frac{r_{13}^2 - r_{12}^2 + r_{23}^2}{2r_{12}r_{13}^2} \right)^2 + \frac{r_{23}^2}{r_{12}^2 r_{13}^2} \right]}. \tag{5.6}$$

Under the assumptions that the distance of the projections of the excited ions ((2) and (3) of Fig. 5.1) from the center are identical for the magnetron and the reduced cyclotron motion and that the distance $r_{23} \ll r$ the uncertainty of the cyclotron frequency ν_c is given by [Eli14]

$$\delta \nu_c \approx \frac{1}{\pi t \sqrt{N_{ion}}} \cdot \frac{\Delta r}{r}. \tag{5.7}$$

Eq. 5.7 indicates that the uncertainty of the determined cyclotron frequency can be reduced by an increased distance r of the excited ions from the center position and a smaller spatial distribution Δr of the ions on the detector. The former is practically limited by the anharmonicity of the electrostatic quadrupole field inside the measurement trap which increases with increasing orbit of the particle motion and leads to a systematic uncertainty of the determined revolution frequency. The spatial distribution can be decreased by careful preparation of the ion sample in the preparation trap. Typically, the radius is $r \approx 1 \, \mathrm{mm}$ and the spatial distribution $\Delta r \approx 50 \, \mu \mathrm{m}$.

According to Eq. 2.13, the magnetron frequency is mass independent. Thus, the resolving power is mainly determined by the ability to resolve the phase difference of the reduced cyclotron frequency:

$$\frac{\nu_c}{\Delta \nu_c} \approx \frac{\nu_+}{\Delta \nu_+} = \frac{\Phi_+ + 2\pi n_+}{\Delta \Phi} = \frac{\pi \nu_+ t r}{\Delta r}. \tag{5.8}$$

Assuming a phase accumulation time $t = 100 \, \mathrm{ms}$ and a reduced cyclotron frequency $\nu_+ = 809251.8 \, \mathrm{Hz}$ for $^{133}\mathrm{Cs}^+$ ions (see Tab. 2.1), a resolving power of $5 \cdot 10^6$ is obtained. The ToF-ICR technique under comparable conditions yields a resolving power of $1.25 \cdot 10^5$ for $^{133}\mathrm{Cs}^+$. Thus, the PI-ICR technique offers a gain in resolving power by a factor of 40 compared to the conventional ToF-ICR method.

In [Eli14] an improved measurement procedure is presented which enables the direct determination of the cyclotron frequency ν_c (see Fig. 5.3). In the new measurement method two timing patterns are executed in an alternating manner. Pattern 2 is identical to the one presented for the determination of ν_+ (see Fig. 5.2 (right)). The other pattern is similar except that the conversion of cyclotron motion into magnetron motion is triggered right after the application of the dipolar excitation at ν_+. For both patterns the same phase accumulation time is used. The difference of both images on the DLD is represented by the cyclotron phase angle
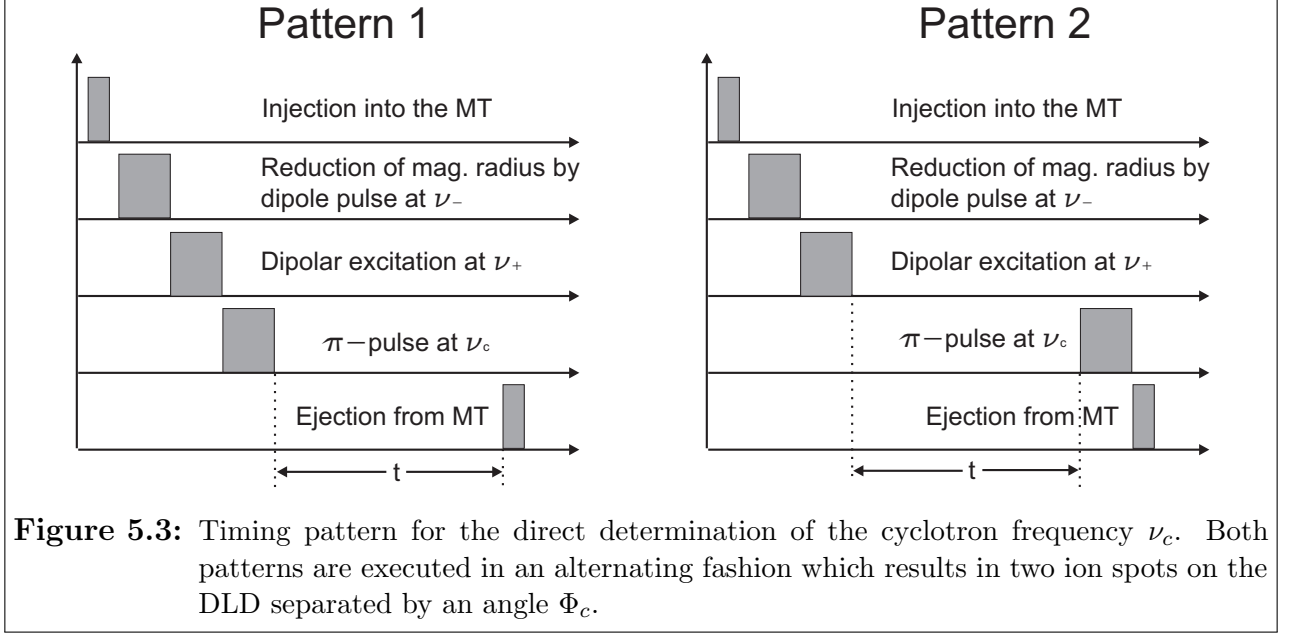
$$\Phi_c = 2\pi \nu_c t - 2\pi (n_+ + n_-) \tag{5.9}$$

which gives access to the cyclotron frequency ν_c.

The PI-ICR technique has been successfully utilized for mass difference measurements between $^{129}\mathrm{Xe}/^{130}\mathrm{Xe}$ [Eli13] and $^{187}\mathrm{Re}/^{187}\mathrm{Os}$ [Nes14] with relative uncertainties below one ppb. A detailed analysis of the systematics involved in the PI-ICR mass measurement technique is given in [Eli14].

5.2.2 The Fourier Transform Ion-Cyclotron-Resonance technique

The FT-ICR technique was developed in the 1970's [Com74] for broad-band identification of the elemental composition of chemical samples. In the same decade the FT-ICR technique was

Figure 5.3: Timing pattern for the direct determination of the cyclotron frequency ν_c. Both patterns are executed in an alternating fashion which results in two ion spots on the DLD separated by an angle Φ_c.
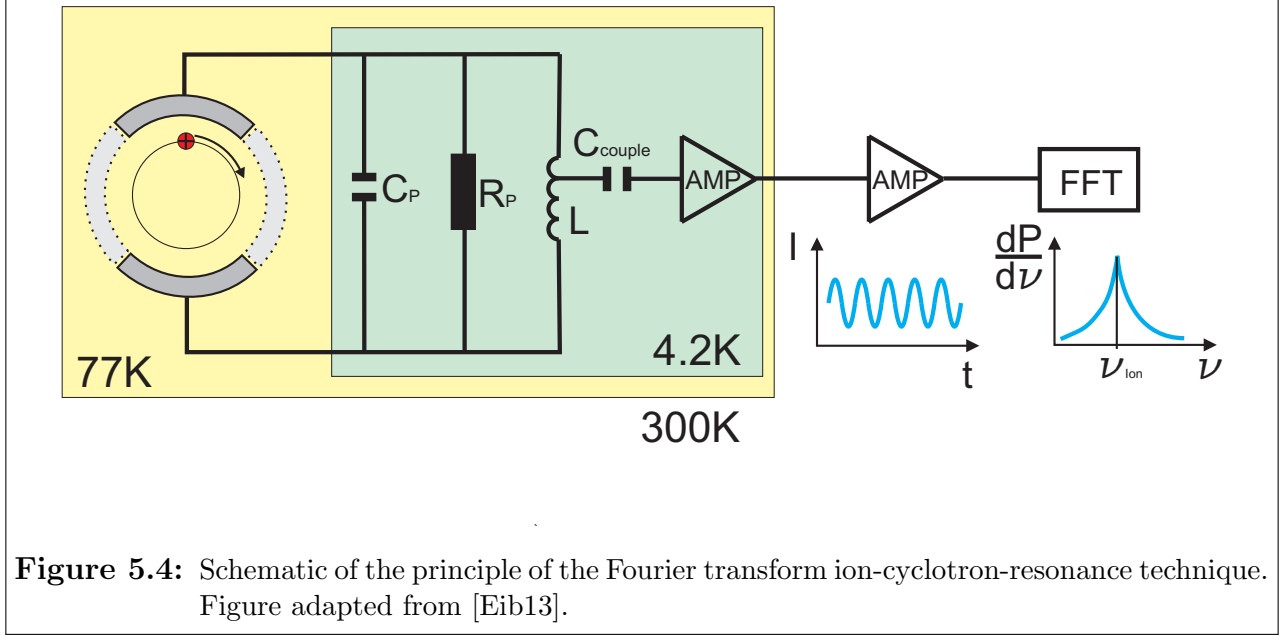
utilized for the determination of the axial frequency of single electrons [Win73]. In 1989 the narrow-band FT-ICR technique in Penning traps was first applied on single molecular ions for the mass difference measurement between N_2^+ and CO^+ with an accuracy of $4 \cdot 10^{-10}$ [Cor89]. Nowadays, the narrow-band FT-ICR technique is utilized in many Penning-trap facilities for mass measurements on stable isotopes in the field of neutrino physics [Str14], g-factor measurements [Ulm11, Stu14] and mass measurements [Hoe13].

A future project at SHIPTRAP is the implementation of the narrow-band FT-ICR technique for high-precision mass measurements on radioactive nuclei. In contrast to existing experiments that utilize the FT-ICR technique on stable nuclei to obtain mass values with accuracies below the ppb level the motivation to use the narrow-band FT-ICR technique at SHIPTRAP is the possibility to perform mass measurements on superheavy elements with production rates less than one ion per day.

A prototype of the FT-ICR detection system for SHIPTRAP is currently set up at TRIGA-TRAP. The current status of the development is presented in [Eib13]. A sketch of the FT-ICR detection technique is given in Fig. 5.4: A trapped ion induces image currents of tens of fA on the segmented ring electrodes (see Fig. 5.4) due to its radial motions, i.e. the magnetron motion as well as on the cyclotron motion, and on the endcap electrodes due to its axial motion. Due to the small image currents the signal-to-noise ratio is a key parameter describing the performance of the experimental setup. The current induced on the electrodes can be determined by the approach of [Com78]:

An ion (with the charge q) is rotating in a radius r_{ion} due the presence of a magnetic field B between two parallel plates with the surface A and the distance D. The electric monopole of the ion can be substituted by a dipole and two monopoles. The monopoles have no differential effect since their induced signals cancel. The electric dipole however induces an electric dipole

Figure 5.4: Schematic of the principle of the Fourier transform ion-cyclotron-resonance technique. Figure adapted from [Eib13].

moment

$$\mu_{dip} = qr_{ion}cos\theta \tag{5.10}$$

where $\theta(t) = \omega t + \varphi$ is the time-dependent angle of the rotation and φ is the phase angle. This leads to a charge density of

$$\zeta(t) = -\frac{\mu_{dip}}{AD} = -\frac{qr_{ion}cos(\omega t + \varphi)}{AD}. \tag{5.11}$$

The negative sign in Eq. 5.11 indicates a negative image charge which leads to

$$Q(t) = \zeta A = -\frac{qr_{ion}cos(\omega t + \varphi)}{D}. \tag{5.12}$$

The image current induced on the parallel plates is then

$$I(t) = \frac{dQ}{dt} = \frac{\omega qr_{ion}sin(\omega t + \varphi)}{D}. \tag{5.13}$$

The root-mean-square value of the image current results in an effective current of

$$I_{eff} = \frac{q^2 r_{ion} B}{\sqrt{2}mD} \tag{5.14}$$

under consideration of $\omega = \omega_c = qB/m$. The induced signal is first amplified by a resonance circuit that is coupled by a tunable capacitive diode C_{couple} to a low-noise amplifier which is operated at LHe temperatures (4.2 K) to reduce the thermal noise. The preamplified signal is fed into the main amplifier stage, placed at room temperature. After the last amplification step the

time-dependent signal is converted via Fourier transformation (by a FFT spectrum analyzer) into a frequency spectrum with a distinct peak at the eigenfrequency of the corresponding ion motion.

The total capacity of the resonance circuit C_{tot}

$$C_{tot} = C_{trap} + C_p + \gamma \frac{C_{amp} C_{couple}}{C_{couple} + C_{amp}} \tag{5.15}$$

originates from the capacity of the trap electrodes C_{trap}, the input capacity of the low-noise amplifier C_{amp}, the tunable coupling capacitor C_{couple} and the parasitic capacity of the connecting wires C_p. In Eq. 5.15 γ denotes the winding ratio where the low-noise amplifier is coupled to the resonator coil with the inductance L. The resonance frequency of the LC_{tot} circuit is tuned with the capacitive diode C_{couple} to match the revolution frequency of the trapped ion. The image current I_{eff} of a trapped ion induces the voltage

$$U_{det} = I_{eff} \cdot Z(\omega_{ion}) \tag{5.16}$$

on the frequency-depending impedance $Z(\omega_{ion})$. The impedance of the resonance circuit, connected to the segments of the ring electrode, consisting of the parasitic resistance R_p of the connecting wires, the total capacity C_{tot} and the inductance L is

$$Z_{LC}^{-1} = \frac{1}{i\omega L} + i\omega C_{tot} + \frac{1}{R_p}. \tag{5.17}$$

As mentioned above the signal is picked up by a tuned LC_{tot} circuit with the resonance frequency $\omega_{LC} = 1/\sqrt{LC_{tot}} = \omega_{ion}$ which matches the revolution frequency of the trapped ion. In this case the imaginary terms of Eq. 5.17 vanish. The quality factor of parallel resonance circuit $Q = \nu/\Delta\nu$ can be also written as

$$Q = R_p \sqrt{\frac{C_{tot}}{L}} = R_p \omega C. \tag{5.18}$$

The thermal noise level of a resistor R_p at the temperature T for a certain spectral range $\Delta\nu$ is

$$U_{noise} = \sqrt{4 k_B T R_p \Delta\nu} \tag{5.19}$$

where k_B is the Boltzmann constant. From Eq. 5.16 and Eq. 5.19 the signal-to-noise ratio S/N results in

$$\frac{S}{N} = \frac{U_{Det}}{U_{noise}} = \frac{q r_{ion} Q}{D C_{tot} \sqrt{8 k_B T R_p \Delta\nu}}. \tag{5.20}$$

Thus, a large quality factor of the inductance L is crucial for a large signal-to-noise ratio. The thermal noise is reduced due to the operation of the resonance circuit and the preamplifier at $4.2\,\mathrm{K}$. Under consideration of Eq. 5.20 the signal-to-noise ratio of a singly charged ion moving in an orbit with a radius $r_{ion} = 1\,\mathrm{mm}$ between two parallel plates in a distance $D =$

32 mm can be estimated. To this end, an upper limit of the total capacity $C_{tot} = 1\,\text{nF}$ and the parasitic resistance $R_p = 0.5\,\Omega$ was chosen. At TRIGA-trap a quality factor (at $T = 4.2\,\text{K}$) of the unloaded tank circuit of about 27000 has been obtained which decreases to $Q = 1400$ if a capacitor of 12 pF, representing the capacity of the Penning trap, is connected to the circuit [Eib13]. A spectral range $\Delta\nu = 2\,\text{Hz}$ corresponds to the measurement range which covers twice the full-width-at-half-maximum of the ToF-ICR resonance for an cyclotron excitation period $T_{exc} = 900\,\text{ms}$ (see Fig. 2.8). The given values result in a signal-to-noise ratio of approximately 300 which would be sufficient for high-precision Penning trap mass measurements. However, it has to be noted that additional sources of noise, like e.g. from the main amplifier and the power supplies creating the electrostatic quadrupole field in the Penning trap, have to be considered for a more elaborate determination of the signal-to-noise ratio.

According to [Com76] resolving power of the FT-ICR technique

$$R = \frac{\omega_c}{\Delta\omega_c(FWHM)} = \frac{\omega T_{rev}}{3.791} = \frac{\nu_c T_{rev}}{0.6} \tag{5.21}$$

is proportional to the data acquisition time T_{rev} during which the ion is moving in the Penning trap and the induced signal is picked up. The dependency of the resolving power from the data acquisition time is similar to those of the quadrupolar excitation time T_{RF} of the ToF-ICR technique (see Eq. 2.20). As a result, the application of the FT-ICR technique to isotopes with half-lives well below 1 s is not favourable since the data acquisition time is limited by the half-life. The FT-ICR technique is a complementary addition to the PI-ICR technique that allows for mass measurements of short-lived nuclei while the FT-ICR technique will provide single-ion sensitivity for mass measurements on isotopes with longer half-lives.

Chapter 6

Summary

In this work the recent activities at the Penning trap mass spectrometer SHIPTRAP have been presented. The main focus of SHIPTRAP is the high-precision mass measurement of transfermium elements. In several experiments since 2008 the masses of the isotopes $^{252-255}$No and ^{255}Lr have been measured with uncertainties of less than $20\,\mathrm{keV}/c^2$ and ^{256}Lr with an uncertainty $83\,\mathrm{keV}/c^2$ [Blo10, Dwo10, Min12]. These masses have been used as anchorpoints for alpha-decay chains to superheavy elements which reduced their mass uncertainty tremendously and, thus, gave valuable input for nuclear mass models. Furthermore, a first direct determination of the deformed shell closure at $N = 152$ by means of the shell-gap parameter $\delta_{2n}(N, Z)$ was given [Min12].

The isotope ^{256}Lr has a reaction cross section of $60(2)\,\mathrm{nbarn}$ which makes it the isotope with the lowest reaction cross section ever measured in a Penning trap. At a detection rate of one ^{256}Lr^{2+} ion in $2\,\mathrm{hours}$ one time-of-flight ion-cyclotron-resonance was obtained within an overall measurement period of four days. For future mass measurements of superheavy elements even smaller production rates are expected. The next envisaged candidate for high-precision mass measurements at SHIPTRAP is ^{257}Rf which has a reaction cross section of $10(1)\,\mathrm{nbarn}$ in the fusion-evaporation reaction ^{208}Pb(^{50}Ti,1n)^{257}Rf. To this end, the overall efficiency of the SHIPTRAP setup, currently mostly limited by the stopping and extraction efficiency of the buffer-gas stopping cell [Neu04, Neu06], needs to be increased. To this end, the cryogenic gas stopping cell was designed [Eli08], commissioned and first tested in offline extraction measurements using a ^{223}Ra ion source. In extensive investigations an extraction efficiency of $74(3)\,\%$ was measured [Dro14]. The stopping efficiency of $91\,\%$ was determined for realistic beam conditions [Dro13] from calculation using the SRIM code. This results in an overall efficiency of $67(3)\,\%$. In comparison to the first-generation gas stopping cell which has an overall efficiency of about $12\,\%$, the CryoCell increases the total efficiency by a factor of 5.

In order to perform high-precision mass measurements on nuclides with half-lives well below $1\,\mathrm{s}$ the PI-ICR technique was developed at SHIPTRAP. In detailed investigations using stable nuclei it was possible to measure mass differences with comparable uncertainties 25 times faster than with the conventional ToF-ICR technique using the Ramsey excitation pattern [Eli13]. In future online experiments on radionuclides the PI-ICR technique will lead to a tremendous

reduction of necessary beam time to measure mass values with comparable accuracy than with the ToF-ICR method.

Ultimately, the implementation of the FT-ICR technique which provides the possibility to perform high-precision mass measurements with a single ion with half-lives above 1 s will pave the way towards direct mass measurements of superheavy nuclei with production rates less than one per day. The development of a small-band FT-ICR prototype for SHIPTRAP at the TRIGATRAP experiment is ongoing [Ket09, Eib13].

With an increased efficiency of SHIPTRAP due to the implementation of the CryoCell and an increased sensitivity of the mass measurement of either short-lived radionuclides with the PI-ICR method or single ions with half lives longer than 1 s with the FT-ICR technique, SHIPTRAP is well suited for high-precision mass measurements of superheavy nuclides.

Aside from mass measurements in the vicinity of superheavy elements, SHIPTRAP is strongly involved in the assessment of possible candidates for the observation of neutrinoless double-electron capture. To this end mass-difference measurements between mother and daughter nuclides have been performed in order to identify mass doublets that are degenerate in energy, which results in a resonant enhancement of the decay rate for this rare process. So far the mass differences between mother and daughter nuclide of 12 potential candidates have been investigated at SHIPTRAP (see Tab. 4.2). Most of the investigated nuclides have to be ruled out from the list of potential candidates for the exploration of the neutrinoless double-electron capture since the resonance condition is not fulfilled. However, the most promising candidate to date is ^{152}Gd [Eli11] whose resonant enhancement leads to a half-life of neutrinoless double-electron capture of 10^{26} years for an effective neutrino mass of 1 eV. Resonant enhancement is furthermore obtained for the transition from ^{156}Dy to ^{156}Gd [Eli11c]. In this particular case, a multiple resonant enhancement to excited nuclear states in ^{156}Dy has been observed with one of them in full resonance within the uncertainty of the mass difference of 100 eV. Thus, the search among the most promising candidates yielded two isotopes worthwhile to investigate the pressing question whether neutrinos are Majorana or Dirac particle in large-scale experiments.

Chapter 7

Bibliography

7.1 Publications as first author

[Dro11] C. Droese, M. Block, M. Dworschak, S. Eliseev, G. Marx, E. Minaya Ramirez, D. Nesterenko and L. Schweikhard, *Investigation of the magnetic field fluctuation and implementation of a temperature and pressure stabilization at SHIPTRAP*, Nucl. Instrum. Methods Phys. Res. Sect. A 632 (2011) 157

[Dro12] C. Droese, K. Blaum, M. Block, S. Eliseev, F. Herfurth, Yu.N. Novikov, E. Minaya Ramirez, L. Schweikhard, V. M. Shabaev, I. I. Tupitsyn, S. Wychech, K. Zuber and N. A. Zubova, *Probing the nuclide ^{180}W for neutrinoless double-electron capture exploration*, Nucl. Phys. A 875 (2012) 1

[Dro13] C. Droese, D. Ackermann, L.-L. Andersson,4, K. Blaum, M. Block, M. Dworschak, M. Eibach, S. Eliseev, U. Forsberg, E. Haettner, F. Herfurth, F.P. Heßberger, S. Hofmann, J. Ketelaer, G. Marx, E. Minaya Ramirez, D. Nesterenko, Yu. N. Novikov, W. R. Plaß, D. Rodríguez, D. Rudolph, C. Scheidenberger, L. Schweikhard, S. Stolze, P.G. Thirolf and C. Weber, *High-precision mass measurements of $^{203-207}Rn$ and ^{213}Ra with SHIPTRAP*, Eur. Phys. J. A 49 (2013) 13

[Dro14] C. Droese, S. Eliseev, K. Blaum, M. Block, F. Herfurth, M. Laatiaoui, F. Lautenschläger, E. Minaya Ramirez, L. Schweikhard, V.V. Simon and P.G. Thirolf, *The cryogenic gas stopping cell of SHIPTRAP*, Nucl. Instrum. Methods Phys. Res. Sect. B 338 (2014) 126

7.2 Publications as coauthor

[Blo10] M. Block, D. Ackermann, K. Blaum, C. Droese, M. Dworschak, S. Eliseev, T. Fleckenstein, E. Haettner, F. Herfurth, F. P. Heßberger, S. Hofmann, J. Ketelaer, J. Ketter, H.-J. Kluge, G. Marx, M. Mazzocco, Yu. N. Novikov, W. R. Plaß, A. Popeko, S. Rahaman,

D. Rodríguez, C. Scheidenberger, L. Schweikhard, P. G. Thirolf, G. K. Vorobyev and C. Weber, *Direct mass measurements above uranium bridge the gap to the island of stability*, Nature 463 (2010) 785

[Dwo10] M. Dworschak, M. Block, D. Ackermann, G. Audi, K. Blaum, C. Droese, S. Eliseev, T. Fleckenstein, E. Haettner, F. Herfurth, F. P. Heßberger, S. Hofmann, J. Ketelaer, J. Ketter, H.-J. Kluge, G. Marx, M. Mazzocco, Yu. N. Novikov, W. R. Plaß, A. Popeko, S. Rahaman, D. Rodríguez, C. Scheidenberger, L. Schweikhard, P. G. Thirolf, G. K. Vorobyev, M. Wang, and C. Weber, *Penning trap mass measurements on nobelium isotopes*, Phys. Rev. C 81 (2010) 064312

[Eli11] S. Eliseev, C. Roux, K. Blaum, M. Block, C. Droese, F. Herfurth, H.-J. Kluge, M. I. Krivoruchenko, Yu.N. Novikov, E. Minaya Ramirez, L. Schweikhard, V. M. Shabaev, F. Šimkovic, I. I. Tupitsyn, K. Zuber and N. A. Zubova, *Resonant Enhancement of Neutrinoless Double-Electron Capture in ^{152}Gd*, Phys. Rev. Lett. 106 (2011) 052504

[Eli11a] S. Eliseev, C. Roux, K. Blaum, M. Block, C. Droese, F. Herfurth, M. Kretzschmar, M. I. Krivoruchenko, Yu.N. Novikov, E. Minaya Ramirez, L. Schweikhard, V. M. Shabaev, F. Šimkovic, I. I. Tupitsyn, K. Zuber and N. A. Zubova, *Octupolar-Excitation Penning-Trap Mass Spectrometry for Q-Value Measurement of Double-Electron Capture in ^{164}Er*, Phys. Rev. Lett. 107 (2011) 152501

[Eli11b] S. Eliseev, D. Nesterenko, K. Blaum, M. Block, C. Droese, F. Herfurth, Yu.N. Novikov, E. Minaya Ramirez, L. Schweikhard and K. Zuber *Q values for neutrinoless double-electron capture in ^{96}Ru, ^{162}Er, and ^{162}Yb*, Phys. Rev. C 83 (2011) 038501

[Eli11c] S. Eliseev, M. Goncharov, K. Blaum, M. Block, C. Droese, F. Herfurth, E. Minaya Ramirez, Yu. N. Novikov, L. Schweikhard, V. M. Shabaev, I. I. Tupitsyn, K. Zuber and N. A. Zubova *Multiple-resonance phenomenon in neutrinoless double-electron capture*, Phys. Rev. C 84 (2011) 012501(R)

[Eli13] S. Eliseev, K. Blaum, M. Block, C. Droese, M. Goncharov, E. Minaya Ramirez, D. A. Nesterenko, Yu.N. Novikov, and L. Schweikhard, *Phase-Imaging Ion-Cyclotron-Resonance Measurements for Short-Lived Nuclides*, Phys. Rev. Lett. 110 (2013) 082501

[Eli14] S. Eliseev, K. Blaum, M. Block, A. Dörr, C. Droese, T. Eronen, M. Goncharov, M. Höcker, J. Ketter, E. Minaya Ramirez, D. A. Nesterenko, Yu. N. Novikov and L. Schweikhard, *A phase-imaging technique for cyclotron-frequency measurements*, Appl. Phys. B 114 (2014) 107

[Gon11] M. Goncharov, K. Blaum, M. Block, C. Droese, S. Eliseev, F. Herfurth, Yu.N. Novikov, E. Minaya Ramirez, L. Schweikhard and K. Zuber *Probing the nuclides ^{102}Pd, ^{106}Cd and ^{144}Sm for resonant neutrinoless double-electron capture*, Phys. Rev. C 84 (2011) 028501

[Min12] E. Minaya Ramirez, D. Ackermann, K. Blaum, M. Block, C. Droese, Ch. E. Düll-mann, M. Dworschak, M. Eibach, S. Eliseev, E. Haettner, F. Herfurth, F. P. Heßberger, S. Hofmann, J. Ketelaer, G. Marx, M. Mazzocco, D. Nesterenko, Yu. N. Novikov, W. R. Plaß, D. Rodríguez, C. Scheidenberger, L. Schweikhard, P. G. Thirolf and C. Weber, *Direct Mapping of Nuclear Shell Effects in the Heaviest Elements*, Science 337 (2012) 1207

[Nes12] D. Nesterenko, K. Blaum, M. Block, C. Droese, S. Eliseev, F. Herfurth, E. Minaya Ramirez, Yu. N. Novikov, L. Schweikhard, V. M. Shabaev, M. V. Smirnov, I. I. Tupitsyn, K. Zuber and N. A. Zubova *Double-β transformations in isobaric triplets with mass numbers A = 124, 130 and 136*, Phys. Rev. C 86 (2012) 044313

[Nes14] D. Nesterenko, S. Eliseev, K. Blaum, M. Block, S. Chenmarev, C. Droese, P. Filyanin, M. Goncharov, E. Minaya Ramirez, Yu.N. Novikov, L. Schweikhard, and V. V. Simon, *Direct determination of the atomic mass difference of ^{187}Re and ^{187}Os for neutrino physics and cosmochronology*, Phys. Rev. C 90.042501(R)

[Rou13] C. Roux, K. Blaum, M. Block, C. Droese, S. Eliseev, M. Goncharov, F. Herfurth, E. Minaya Ramirez, D. Nesterenko and Y. N. Novikov and L. Schweikhard, *Data analysis of Q-value measurements for double-electron capture with SHIPTRAP*, Eur. Phys. J. D 67 (2013) 146

7.3 Publications by others

[Ack11] N. Ackermann for the EXO collaboration, *Observation of Two-Neutrino Double-Beta Decay in ^{136}Xe with the EXO-200 Detector*, Phys. Rev. Lett. 107 (2011) 212501

[Ago13] M. Agostini for the GERDA collaboration, *Results on Neutrinoless Double-β Decay of ^{76}Ge from Phase I of the GERDA Experiment*, Phys. Rev. Lett. 111 (2013) 122503

[Ahm01] Q. R. Ahmad for the SNO collaboration, *Measurement of the Rate of $\nu_e + d \rightarrow p + p + e^-$ Interactions Produced by ^8B Solar Neutrinos at the Sudbury Neutrino Observatory*, Phys. Rev. Lett. 87 (2001) 071301

[Arn10] R. Arnold for the NEMO collaboration, *Probing new physics models of neutrinoless double beta decay with SuperNEMO*, Eur. Phys. J. C 70 (2010) 927

[Ast20] F. W. Aston, *The constitution of atmospheric neon*, Philosophical Magazine 39 (1920) 449

[Ast27] F. W. Aston, *A New Mass-Spectrograph and the Whole Number Rule*, Proc. R. Soc. Lond. A 115 (1927) 487

[Aud03] A.H. Wapstra, G. Audi and C. Thibault, *The AME2003 atomic mass evaluation*, Nucl. Phys. A 729 (2003) 129

[Avi08] F. T. Avignon III for the CUORICINO collaboration, *Results from a search for the 0νββ-decay of ^{130}Te*, Phys. Rev. C 78 (2008) 035502

[Ben06] J. Benlliure, *Spallation Reactions in Applied and Fundamental Research*, Lect. Notes Phys. 700 (2006) 173

[Ber83] J. Bernabeu, A. De Rujula and C. Jarlskog, *Neutrinoless double electron capture as a Tool to measure the electron neutrino mass*, Nucl. Phys. B 223 (1983) 15

[Bev88] N. Beverini, V. Lagomarsino, G. Manuzio, F. Scuri, G. Testera and G. Torelli, *Stochastic cooling in Penning traps*, Phys. Rev. A 38 (1988) 107

[Bev88a] N. Beverini, V. Lagomarsino, G. Manuzio, F. Scuri, G. Testera and G. Torelli, *Stochastic cooling in Penning traps*, Phys. Scr. T22 (1988) 238

[Bla06] K. Blaum, *High-accuracy mass spectrometry with stored ions*, Phys. Rep. 425 (2006) 1

[Bla09] K. Blaum, H. Kracke, S. Kreim, A. Mooser, C. Mrozik, W. Quint, C. C. Rodegheri, B. Schabinger, S. Sturm, S. Ulmer, A. Wagner, J. Walz and G. Werth, *g-factor experiments on simple systems in Penning traps*, J. Phys. B: At. Mol. Opt. Phys. 42 (2009) 154021

[Bla09a] K. Blaum, Sz. Nagy and G. Werth *High-accuracy Penning trap mass measurements with stored and cooled exotic ions*, J. Phys. B: At. Mol. Opt. Phys. 42 (2009) 154015

[Blu13] Y. Blumenfeld, T. Nilsson and P. Van Duppen, *Facilities and methods for radioactive ion beam production*, Phys. Scr. T152 (2013) 014023

[Bol90] G. Bollen, R.B. Moore, G. Savard and H. Stolzenberg, *The accuracy of heavy-ion mass measurements using time of flight-ion cyclotron resonance in a Penning trap*, J. Appl. Phys. 68 (1990) 4355

[Bro86] L. S. Brown and G. Gabrielse, *Geonium theory: Physics of a single electron or ion in a Penning trap*, Rev. Mod. Phys. 58 (1986) 233

[Cha07] A. Chaudhuri, *Carbon-cluster mass calibration at SHIPTRAP*, PhD thesis (Ernst-Moritz-Arndt-Universität Greifswald, 2007)

[Cha13] A. Chaudhuri, C. Andreoiu, T. Brunner, U. Chowdhury, S. Ettenauer, A. T. Gallant, G. Gwinner, A. A. Kwiatkowski, A. Lennarz, D. Lunney, T. D. Macdonald, B. E. Schultz, M. C. Simon, V. V. Simon and J. Dilling, *Evidence for the extinction of the N = 20 neutron-shell closure for ^{32}Mg from direct mass measurements*, Phys. Rev. C 88 (2013) 054317

[Com74] M. B. Comisarow and A. G. Marshall, *Fourier Transform Ion Cyclotron Resonance Spectroscopy*, Chem. Phys. Lett. 25 (1974) 282

[Com76] M. B. Comisarow and A. G. Marshall, *Theory of Fourier transform ion cyclotron resonance mass spectroscopy. I. Fundamental equations and lowpressure line shape*, J. Chem. Phys. 64 (1976) 110

[Com78] M. B. Comisarow, *Signal modeling for ion cyclotron resonance*, J. Chem. Phys. 69 (1978) 4097

[Cor89] E. A. Cornell, R. M. Weisskopf, K. R. Boyce, W. Flanagan Jr., G. P. Lafyatis and D. E. Pritchard, *Sinlge-Ion Cyclotron Resonance Measurement of $M(CO^+)/M(N_2^+)$*, Phys. Rev. Lett. 63 (1989) 1674

[Cwi96] S. Ćwiok, J. Dobaczewski, P.-H. Heenen, Magierski and W. Nazarewicz, *Shell structure of the superheavy elements*, Nucl. Phys. A 611 (1996) 211

[Den97] P. Dendooven, *The development and status of the IGISOL technique*, Nucl. Instr. Meth. Phys. Res. B 126 (1997) 182

[Den00] V. Yu. Denisov and S. Hofmann, *Formation of superheavy elements in cold fusion reactions*, Phys. Rev. C 61 (2000) 034606

[Dom00] M. Dombsky, D. Bishop, P. Bricault, D. Dale, A. Hurst, K. Jayamanna, R. Keitel, M. Olivo, P. Schmor and G. Stanford, *Commissioning and initial operation of a radioactive beam ion source at ISAC*, Rev. Sci. Instrum. 71 (2000) 978

[Edd20] A. S. Eddington, *The internal constitution of the stars*, Nature 106 Number 2653 (1920) 14

[Eib13] M. Eibach, *High-precision mass measurements in the realm of the deformed shell closure $N = 152$*, PhD thesis (Ruprecht - Karls - Universität Heidelberg, 2013)

[Eli07] S. Eliseev, M. Block, A. Chaudhuri, F. Herfurth, H.-J. Kluge, A. Martin, C. Rauth and G. Vorobjev, *Octupolar excitation of ions stored in a Penning trap mass spectrometer - A study performed at SHIPTRAP*, Int. J. Mass Spectrom. 262 (2007) 45

[Eli07a] S. Eliseev, M. Block, A. Chaudhuri, Z. Di, D. Habs, F. Herfurth, H.-J. Kluge, J.B. Neumayr, W.R. Plaß, C. Rauth, P.G. Thirolf, G. Vorobjev, Z. Wang, *Extraction efficiency and extraction time of the SHIPTRAP gas-filled stopping cell*, Nucl. Instr. Meth. Phys. Res. B 258 (2007) 479

[Eli08] S. Eliseev, M. Block, M. Dworschak, F. Herfurth, H.-J. Kluge, A. Martin, C. Rauth, G. Vorobjev, *A new cryogenic gas-filled stopping chamber for SHIPTRAP*, Nucl. Instr. Meth. Phys. Res. B 266 (2008) 4475

[Fer34] E. Fermi, *Versuch einer Theorie der β-Strahlen*, Z. Phys. A 88 (1934) 161

[Gab89] G. Gabrielse, L. Haarsna and S. L. Rolston, *Open-endcap Penning traps for high-precision mass measurements*, Int. J. Mass Spec. Ion Proc. 88 (1989) 319

[Gal12] A. T. Gallant, M. Brodeur, T. Brunner, U. Chowdhury, S. Ettenauer, V. V. Simon, E. Mané, M. C. Simon, C. Andreoiu, P. Delheij, G. Gwinner, M. R. Pearson, R. Ringle and J. Dilling, *Highly charged ions in Penning traps: A new tool for resolving low-lying isomeric states*, Phys. Rev. C 85 (2012) 044311

[Geo11] S. George, K. Blaum, F. Herfurth, A. Herlert, M. Kretzschmar, S. Nagy, S. Schwarz, L. Schweikhard and C. Yazidjian, *The ramsey method in high-precision mass spectrometry with Penning traps: Experimental results*, Int. J. Mass Spectrom. 264 (2007) 110

[Gol13] A. Goldschmidt for the NEXT collaboration, *Near-intrinsic energy resolution for 30-662keV gamm rays in a pressure xenon electroluminescent TPC*, Nucl. Instr. Meth. A 708 (2013) 101

[Gor10] S. Goriely, N. Chamel and J. M. Pearson, *Further explorations of Skyrme-Hartree-Fock-Bogoliubov mass formulas. XII. Stiffness and stability of neutron-star matter*, Phys. Rev. C 82 (2010) 035804

[Gra80] G. Gräff, H. Kalinowsky and J. Traut, *A Direct Determination of the Proton Electron Mass Ratio*, Z. Phys. A 297 (1980) 35

[GSI] www.gsi.de (11.08.2014)

[Gup97] R. K. Gupta, S. K. Patra and W. Greiner, *Structure of $^{294,302}120$ Nuclei Using the Relativistic Mean-Field Method*, Mod. Phys. Lett. A 12 (1997) 1727

[Hae11] E. Haettner, *A novel radio frequency quadrupole system for SHIPTRAP & New mass measurements of rp nuclides*, PhD thesis (Justus-Liebig-Universität Gießen, 2011)

[Hes97] F. P. Heßberger, S. Hofmann, V. Ninov, P. Armbruster, H. Folger, G. Münzenberg, H. J. Schött, A. G. Popeko, A. V. Yeremin, A. N. Andreyev, S. Saro, *Spontaneous fission and alpha-decay properties of neutron deficient isotopes $^{257-253}104$ and $^{258}106$* Z. Phys. A 359 (1997) 415

[Hey11] K. Heyde and J. L. Wood, *Shape coexistence in atomic nuclei*, Rev. Mod. Phys. 83 (2011) 1467

[Hoe13] M. Höcker, R. Rana and E. G. Myers, *Atomic masses of $^{82,83}Kr$ and $^{131,134}Xe$*, Phys. Rev. A 88 (2013) 052502

[Hof00] S. Hofmann and G. Münzenberg, *The discovery of the heaviest elements*, Rev. Mod. Phys. 72 (2000) 733

[Hof02] S. Hofmann and G. Münzenberg, *New results on Elements 111 and 112*, Eur. Phys. J. A 14 (2002) 147

[Ita95] W. M. Itano, J. C. Bergquist, J. J. Bollinger and D. J. Wineland, *Cooling Methods in Ion Traps*, Phys. Scr. T59 (1995) 106

[Jav80] J. Javanainen, *Laser Cooling of Trapped Particles I: The Heavy Particle Limit*, Appl. Phys. A 21 (1980) 283

[Jav81] J. Javanainen, *Laser Cooling of Trapped Particles II: The Fast Particle Limit*, Appl. Phys. A 24 (1981) 71

[Jef83] J. B. Jeffries, S. E. Barlow and G. H. Dunn, *Theory of space-charge shift of ion cyclotron resonance frequencies*, Int. J. Mass Spectrom. Ion Proc. 54 (1983) 169

[Jen06] T. C. Jen, Liangming Pan, Longjian Li, Qinghua Chen, Wenzhi Cui, *The acceleration of charged nano-particles in gas streams of supersonic de-Laval-type nozzle coupled with static electric field*, Appl. Therm. Eng. 26 (2006) 613

[Ket09] J. Ketelaer, K. Blaum, M. Block, K. Eberhardt, M. Eibach, R. Ferrer, S. George, F. Herfurth, J. Ketter, Sz. Nagy, J. Repp, L. Schweikhard, C. Smorra, S. Sturm, and S. Ulmer, *Recent developments in ion detection techniques for Penning trap mass spectrometry at TRIGA-TRAP*, Eur. Phys. J. A 42 (2009) 311

[Kla06] H. V. Klapdor-Kleingrothaus and I. V. Krivosheina, *The evidence for the observation of $0\nu\beta\beta$ decay: The identification of $0\nu\beta\beta$ events from the full spectra*, Mod. Phys. Lett. A 20 (2006) 1547

[Kla65] R. Klapisch and R. Bernas, *The detection of the short-lived lithium isotopes ^8Li and ^9Li by preliminary experiments with an on-line mass spectrometer*, Nucl. Instr. Meth. 38 (1965) 291

[Kod01] K. Kodama for the DONUT collaboration, *Observation of tau neutrino interactions*, Phys. Lett. B 504 (2001) 218

[Kof51] O. Kofoed-Hansen and P. Kristensen, *β-Recoil Experiments with Kr^{89}*, Phys. Rev. 82 (1951) 96

[Kon95] M. König, G. Bollen, H.-J. Kluge, T. Otto and J. Szerypo, *Quadrupole excitation of stored ion motion at the true cyclotron frequency*, Int. J. Mass Spectrom. Ion Proc. 142 (1995) 95

[Kud01] Yu. Kudryatsev, B. Bryuneel, M. Huyse, J. Gentens, P. Van den Bergh, P. Van Duppen, L. Vermeeren, *A gas cell for thermalizing, storing and transporting radioactive ions and atoms. Part I: Off-Line studies with a laser ion source*, Nucl. Instr. Methods Phys. Res. B 179 (2001) 412

[Kug00] E. Kugler, *The ISOLDE facility*, Hyperfine Interact. 129 (2000) 23

[Lob03] V. M. Lobashev, *The search for the neutrino mass by direct method in the tritium beta-decay and perspectives of study it in the project KATRIN*, Nucl. Phys. A 719 (2003) C153

[Man13] V. Manea, D. Atanasov, D. Beck, K. Blaum, C. Borgmann, R. B. Cakirli, T. Eronen, S. George, F. Herfurth, A. Herlert, M. Kowalska, S. Kreim, Yu. A. Litvinov, D. Lunney, D. Neidherr, M. Rosenbusch, L. Schweikhard, F. Wienholtz, R. N. Wolf, and K. Zuber, *Collective degrees of freedom of neutron-rich $A \approx 100$ nuclei and the first mass measurement of the short-lived nuclide ^{100}Rb*, Phys. Rev. C 88 (2013) 054322

[Mav14] S. Mavadia, G. Stutter, J. F. Goodwin, D. R. Crick, R. C. Thompson and D. M. Segal, *Optical sideband spectroscopy of a single ion in a Penning trap*, Phys. Rev. A 89 (2014) 032502

[Mel67] H. Meldner, 1967, in Proceedings of the International Symposium on Nuclides far off the Stability Line, Lysekil, Sweden, August 21ï¿½27, 1966, edited by W. Forsling, C. J. Herrlander, and H. Ryde, Ark. Fys. 36, 593.

[Moe95] P. Möller, J. R. Nix, W. D. Myers and W. J. Swiatecki, *Nuclear Ground-State Masses and Deformations*, At. Data Nucl. Data Table 59 (1995) 185

[Mos69] U. Mosel and W. Greiner, *On the stability of superheavy nuclei against fission*, Z. Phys. 222 (1969) 261

[Mun03] I. Muntian, S. Hofmann, Z. Patyk and A. Sobiczewski, *Properties of Heaviest Nuclei*, Act. Phys. Pol. B 34 (2003) 2073

[Mun81] G. Münzenberg, S. Hofmann, F. P. Heßberger, W. residorf, K. H. Schmidt, J. R. H. Schneider, P. Armbruster, C. C. Sahm and B. Thuma, *Identification of Element 107 by α-Correlation Chains*, Z. Phys. A 300 (1981) 107

[Mun84] G. Münzenberg, P. Armbruster, H. Folger, F. P. Heßberger, S. hofmann, J. Keller, K. Poppensieker, W. Reisdorf, K. H. Schmidt, H. J. Schött, M. E. Leino and R. Hingmann, *The identification of Element 108*, Z. Phys. A 317 (1984) 235

[Mun88] G. Münzenberg, S. Hofmann, F. P. Heßberger, H. Folger, V. Ninov, K. Poppensieker, A. B. Quint, W. Reisdorf, H. J. Schött, K. Sümmerer, P. Armbruster, I. Zychor, M. E. Leino, R. Hingmann, U. Gollerthan, E. Hanelt, W. Morawek, Y. Fujita, T. Schwab and A. Türler, *New results on Element 109*, Z. Phys. A 330 (1988) 435

[Mye66] Myers, W. D., and W. J. Șwiątecki, *Nuclear masses and deformations*, Nucl. Phys. 81 (1966) 1

[Mye96] W. D. Myers and W. J. Șwiątecki, *Nuclear properties according to the Thomas-Fermi model*, Nucl. Phys. A 601 (1996) 141

[Mye13] E. G. Myers, *The most precise atomic mass measurements in Penning traps*, Int. J. Mass Spectrom. 349 (2013) 107

[Neu04] J. B. Neumayr, *The buffer-gas cell and the extraction RFQ for SHIPTRAP*, PhD thesis (Ludwig-Maximilians-Universität München, 2004)

[Neu06] J.B. Neumayr, L. Beck, D. Habs, S. Heinz, J. Szerypo, P.G. Thirolf, V. Varentsov, F. Voit, D. Ackermann, D. Beck, M. Block, Z. Di, S.A. Eliseev, H. Geissel, F. Herfurth, F.P. Heßberger, S. Hofmann, H.-J. Kluge, M. Mukherjee, G. Münzenberg, M. Petrick, W. Quint, S. Rahaman, C. Rauth, D. Rodríguez, C. Scheidenberger, G. Sikler, Z. Wang, C. Weber, W.R. Plaß, M. Breitenfeldt, A. Chaudhuri, G. Marx, L. Schweikhard, A.F. Dodonov, Y. Novikov and M. Suhonen, *The ion-catcher device for SHIPTRAP*, Nucl. Instr. and Meth. in Phys. Res. B 244 (2006) 489

[Nil69] S. G. Nilsson, C. F. Tsang, A. Sobiczewski, Z. Szymański, S. Wycech, C. Gustafson, I.-L. Lamm, P. Möller and B. Nilsson, *On the nuclear structure and stability of heavy and superheavy elements*, Nucl. Phys. A 131 (1969) 1

[NUC] Nucleus Win 2.1 http://nucleus-win.software.informer.com/2.1/

[Oga99] Yu. Ts. Oganessian, A. V. Yeremin, V. I. Chepigin, M. G. Itkis, A. P. Kabachenko, M. Konstantinesky, O. N. Malyshev, A. G. Popeko, J. Roháč, R. N. Sagaidak, I. V. Shirokovsky, V. K. Utyonkov, S. Hofmann, G. Münzenberg, M. Veselsky, S. Saro, N. Iwasa, K. Morita, A. Yoneda and M. Hussonnois, *Experiments on the synthesis of superheavy elements with Z=110, 112 via ^{232}Th, $^{238}U+^{48}Ca$ reactions*, Acta Physica Slovaca 49 (1999) 65

[Oga06] Yu. Ts. Oganessian, V. K. Utyonkov, Yu. V. Lobanov, F. Sh. Abdullin, A. N. Polyakov, R. N. Sagaidak, I. V. Shirokovsky, Yu. S. Tsyganov, A. A. Voinov, G. G. Gulbekian, S. L. Bogomolov, B. N. Gikal, A. N. Mezentsev, S. Iliev, V. G. Subbotin, A. M. Sukhov, K. Subotic, V. I. Zagrebaev, G. K. Vostokin and M. G. Itkis, *Synthesis of the isotopes of elements 118 and 116 in the ^{249}Cf and $^{245}Cm+^{48}Ca$ fusion reactions*, Phys. Rev. C 74 (2006) 044602

[Pau77] W. Pauli, *Fünf Arbeiten zum Ausschließungsprinzip und zum Neutrino* Texte zur Forschung Vol. 27 (Wissenschaftliche Buchgesellschaft Darmstadt, 1977)

[Pau90] W. Paul, *Electromagnetic traps for charged and neutral particles*, Rev. Mod. Phys. 62 (1990) 531

[Pla13] W.R. Plaß, T. Dickel, S. Purushothaman, P. Dendooven, H. Geissel, J. Ebert, E. Haettner, C. Jesch, M. Ranjan, M.P. Reiter, H. Weick, F. Amjad, S. Ayet, M. Diwisch, A. Estrade, F. Farinon, F. Greiner, N. Kalantar-Nayestanaki, R. Knöbel, J. Kurcewicz, J. Lang, I. Moore, I. Mukha, C. Nociforo, M. Petrick, M. Pfützner, S. Pietri, A. Prochazka, A.-K. Rink, S. Rinta-Antila, D. Schäfer, C. Scheidenberger, M. Takechi, Y.K. Tanaka, J.S. Winfield, M.I. Yavor, *The FRS Ion Catcher: A facility for high-precision experiments with stopped projectile and fission fragments*, Nucl. Instr. Meth. Phys. Res. B 317 (2013) 457

[Pon68] B. Pontecorvo, *Neutrino experiments and the Problem of Conservation of Leptonic Charge*, Sov. Phys. JETP 26 (1968) 984

[Rah05] S. Rahaman, *First on-line mass measurements at SHIPTRAP and mass determinations of neutron-rich Fr and Ra isotopes at ISOLTRAP*, PhD thesis (Ruprecht-Karls-Universität Heidelberg, 2005)

[Rau07] C. Rauth, *Direct mass measurements beyond the proton drip-line*, PhD thesis (Ruprecht-Karls-Universität Heidelberg, 2007)

[Rei56] F. Reines and C. L. Cowan, *The Neutrino*, Nature 178 (1956) 446

[Rod03] D. Rodríguez, *An RFQ buncher for accumulation and cooling of heavy radionuclides at SHIPTRAP and high precision mass measurements on unstable Kr isotopes at ISOLTRAP*, PhD thesis (Universitat de València, 2003)

[Rut97] K. Rutz, M. Bender, T. Bürvenich, P.-G. Reinhard, J. A. Maruhn and W. Greiner, *Superheavy Nuclei in self-consistent nuclear calculations*, Phys. Rev. C 56 (1997) 238

[Sai05] M. Saidur Rahaman, *First on-line mass measurements at SHIPTRAP and mass determinations of neutron-rich Fr and Ra isotopes at ISOLTRAP*, PhD thesis (Ruprecht-Karls-Universität Heidelberg, 2005)

[Sav91] G. Savard, St. Becker, G. Bollen, H.-J. Kluge, R.B. Moore, Th. Otto, L. Schweikhard, H. Stolzenberg and U. Wiess, *A new cooling technique for heavy ions in a Penning trap*, Phys. Lett. A 158 (1991) 247

[Sav08] G. Savard, S. Baker, C. Davids, A.F. Levand, E.F. Moore, R.C. Pardo, R. Vondrasek, B.J. Zabransky and G. Zinkann, *Radioactive beams from gas catchers: The CARIBU facility*, Nucl. Instr. Meth. Phys. Res. B 266 (2008) 4086

[Sch11] S. Schwarz, *RF ion carpets: The electric field, the effective potential, operational parameters and an analysis of stability*, Int. J. Mass Spectrom. 299 (2011) 71

[Smi08] M. Smith, M. Brodeur, T. Brunner, S. Ettenauer, A. Lapierre, R. Ringle, V. L. Ryjkov, F. Ames, P. Bricault, G. W. F. Drake, P. Delheij, D. Lunney, F. Sarazin and J. Dilling, *First Penning-Trap Mass Measurement of the Exotic Halo Nucleus ^{11}Li*, Phys. Rev. Lett. 101 (2008) 202501

[Sod17] F. Soddy, *The Atomic Weight of "Thorium" Lead*, Nature 98 Number 2468 (1920) 469

[Spi01] U. Spillmann, O. Jagutzki, L. Spielberger, R. Dörner, V. Mergel, K. Ullmann-Pfleger and H. Schmidt-Böcking, *A Novel Delay-Line Anode Design for Position and Time Sensitive Read-Out of MCP-Based Detectors*, Phys. Scr. T92 (2001) 225

[Ste62] J. Steinberger, M. Schwartz, G. Danby, J-M. Gaillard, K. Goulianos and L. M. Lederman, *Observation of high-energy neutrino reactions and the existence of two kinds of neutrinos*, Phys. Rev. Lett. 9 (1962) 36

[Str67] V. M. Strutinsky, *Shell effects in nuclear masses and deformation energies*, Nucl. Phys. A 95 (1967) 420

[Str14] S. Streubel, T. Eronen, M. Höcker, J. Ketter, M. Schuh, R. S. Van Dyck Jr. and K. Blaum, *Towards a more accurate Q value measurement of tritium: status of THe-Trap*, Appl. Phys. B 114 (2014) 137

[Stu14] S. Sturm, F. Köhler, J. Zatorski, A. Wagner, Z. Harman, G. Werth, W. Quint, C. H. Keitel and K. Blaum, *High-precision measurement of the atomic mass of the electron*, Nature 506 (2014) 467

[Suj04] Z. Sujkowski and S. Wycech, *Neutrinoless double electron capture: A tool to search for Majorana neutrinos*, Phys. Rev. C 70 (2004) 052501(R)

[Ulm11] S. Ulmer, K. Blaum, H. Kracke, A. Mooser, W. Quint, C. C. Rodegheri and J. Walz, *Direct Measurement of the Free Cyclotron Frequency of a single Particle in a Penning Trap*, Phys. Rev. Lett. 107 (2011) 103002

[Wad03] Michiharu Wada, Yoshihisa Ishida, Takashi Nakamura, Yasunori Yamazaki, Tadashi Kambara, Hitoshi Ohyama, Yasushi Kanai, Takao M. Kojima, Youichi Nakai, Nagayasu Ohshima, Atsushi Yoshida, Toshiyuki Kubo, Yukari Matsuo, Yoshimitsu Fukuyama, Kunihiro Okada, Tetsu Sonoda, Shunsuke Ohtani, Koji Noda, Hirokane Kawakami, Ichiro Katayama, *Slow RI-beams from projectile fragment separators*, Nucl. Instr. Meth. Phys. Res. B 204 (2003) 570

[Wad06] M. Wada, *Deceleration and cooling of radioactive isotope beams - from GeV to μeV*, Nucl. Instr. Meth. Phys. Res. A 532 (2006) 40

[Wan12] M. Wang, G. Audi, A.H. Wapstra, F.G. Kondev, M. MacCormick, X. Xu and B. Pfeiffer, *The AME2012 atomic mass evaluation (II). Tables, graphs and references*, Chinese Phys. C 36 (2012)1603

[Web04] C. Weber, *Konzeption eines kryogenen Penningfallenaufbaus für SHIPTRAP und Massenbestimmungen von Radionukliden um den Z = 82 - Schalenabschluss an ISOLTRAP*, PhD thesis (Ruprecht-Karls-Universität Heidelberg, 2004)

[Wei05] L. Weissman, D. J. Morrissey, G. Bollen, D. A. Davies, E. Kwan, P.A. Lofy, P. Schury, S. Schwarz, C. Sumithrarachchi, *Conversion of $92\,MeV/u$ $^{38}Ca/^{37}K$ projectile fragments into thermalized ion beams*, Nucl. Instr. Meth. Phys. Res. A 540 (2005) 245 T. Suna,c, R. Ringlea,

[Win73] D. Wineland, P. Ekstrom and H. Dehmelt, *Monoelectron Oscillator*, Phys. Rev. Lett. 21 (1973) 31

[Wol10] J. Wolf for the KATRIN collaboration, *The KATRIN neutrino experiment*, Nucl. Instr. Meth. Phys. Res. A 623 (2010) 442

[Yar07] S. Yaramyshev, W. Barth, W. Bayer, L. Dahl, L. Groening and S. Richter, *Upgrade program of the high current heavy ion UNILAC as an injector for FAIR*, Nucl. Instr. Meth. Phys. Res. A 577 (2007) 211

[Zha05] W. Zhang, J. Meng, S. Q. Zhang, L. S. Geng and H. Toki, *Magic numbers for super-heavy nuclei in relativistic continuum Hartree-Bogoliubov theory*, Nucl. Phys. A. 753 (2005) 106

[Zie10] J. F. Ziegler, M. D. Ziegler and J. P. Biersack, *SRIM - The stopping and range of ions in matter (2010)*, Nucl. Instrum. Methods Phys. Res. Sec. B 268 (2010) 1818

Chapter 8

Cummulative thesis articles

8.1 Author Contribution

Min12: Direct Mapping of Nuclear Shell Effects in the Heaviest Elements,
E. Minaya Ramirez, D. Ackermann, K. Blaum, M. Block, C. Droese, Ch. E. Düllmann, M. Dworschak, M. Eibach, S. Eliseev, E. Haettner, F. Herfurth, F. P. Heßberger, S. Hofmann, J. Ketelaer, G. Marx, M. Mazzocco, D. Nesterenko, Yu. N. Novikov, W. R. Plaß, D. Rodríguez, C. Scheidenberger, L. Schweikhard, P. G. Thirolf and C. Weber, **Science 337 (2012) 1207**
E. M. R., M.B., C. D., M. D., M. E., S. E., E. H., F. H., F. P. H., J. K., D. N., M. M., W. R. P., D. R., P. G. T. and C. W. performed the measurements. E. M. R. prepared the manuscript which was edited by all coauthors.

Dro12: Probing the nuclide ^{180}W for neutrinoless double-electron capture exploration, C. Droese, K. Blaum, M. Block, S. Eliseev, F. Herfurth, Yu.N. Novikov, E. Minaya Ramirez, L. Schweikhard, V. M. Shabaev, I. I. Tupitsyn, S. Wychech, K. Zuber and N. A. Zubova, **Nucl. Phys. A 875 (2012) 1**
C. D., S. E. and E. M. R. performed the measurements. C. D. and S. E. performed the data analysis. C. D. prepared the manuscript which was edited by all coauthors.

Dro14: The cryogenic gas stopping cell of SHIPTRAP,
C. Droese, S. Eliseev, K. Blaum, M. Block, F. Herfurth, M. Laatiaoui, F. Lautenschläger, E. Minaya Ramirez, L. Schweikhard, V.V. Simon and P.G. Thirolf, **Nucl. Instrum. Methods Phys. Res. Sect. B 338 (2014) 126**
S. E. designed the apparatus. C. D. prepared and performed the measurements. C. D. prepared the manuscript which was edited by all coauthors.

Confirmed

Greifswald, den 14.11.2014

———————————— ————————————
Christian Droese   Prof. Dr. Lutz Schweikhard

8.2 Direct Mapping of Nuclear Shell Effects in the Heaviest Elements, Science 337 (2012) 1207

Direct Mapping of Nuclear Shell Effects in the Heaviest Elements

E. Minaya Ramirez,[1,2] D. Ackermann,[2] K. Blaum,[3,4] M. Block,[2]* C. Droese,[5] Ch. E. Düllmann,[6,2,1] M. Dworschak,[2] M. Eibach,[4,6] S. Eliseev,[3] E. Haettner,[2,7] F. Herfurth,[2] F. P. Heßberger,[2,1] S. Hofmann,[2] J. Ketelaer,[3] G. Marx,[5] M. Mazzocco,[8] D. Nesterenko,[9] Yu. N. Novikov,[9] W. R. Plaß,[2,7] D. Rodríguez,[10] C. Scheidenberger,[2,7] L. Schweikhard,[5] P. G. Thirolf,[11] C. Weber[11]

Quantum-mechanical shell effects are expected to strongly enhance nuclear binding on an "island of stability" of superheavy elements. The predicted center at proton number $Z = 114$, 120, or 126 and neutron number $N = 184$ has been substantiated by the recent synthesis of new elements up to $Z = 118$. However, the location of the center and the extension of the island of stability remain vague. High-precision mass spectrometry allows the direct measurement of nuclear binding energies and thus the determination of the strength of shell effects. Here, we present such measurements for nobelium and lawrencium isotopes, which also pin down the deformed shell gap at $N = 152$.

Quantum-mechanical shell effects play a crucial role in determining the structure and the properties of matter. The electronic shell structure defines the architecture of the periodic table. An analogous effect leads to the so-called magic nuclei—closed nucleon shells that result in an enhanced binding of the atomic nucleus—that opposes Coulomb repulsion of protons and governs the landscape of the nuclear chart. The heaviest stable doubly magic nucleus is ^{208}Pb with proton number $Z = 82$ and neutron number $N = 126$. The quest for the end of the periodic table and the northeast limit of the nuclear chart (Fig. 1) drives the search for even heavier magic nuclei.

In these superheavy elements (SHEs), nuclear shell effects are decisive for their mere existence. Without them, their nuclei would instantaneously disintegrate by spontaneous fission through Coulomb repulsion. A manifestation of these nuclear shell effects is an increase of the half-life by 15 orders of magnitude compared to liquid-drop-model predictions for nuclei around $N = 152$ (1). Thus, SHEs are a prime testing ground for the understanding of shell effects and the character of the nuclear force.

Already in the late 1960s, about two decades after the introduction of the nuclear shell model (2, 3), an "island of stability" of SHEs far from the known nuclei was predicted. Recent experimental evidence for the existence of isotopes of elements up to $Z = 118$ (4) has confirmed this concept, but the exact location and extension of this island are still unknown (5–7). The presently

known or claimed nuclides in the northeast end of the nuclear chart are shown in Fig. 1. The blue shaded background indicates the gain in binding energy from shell effects. Regions of enhanced binding are predicted for the deformed magic nuclei at $N = 152$ and 162 around fermium ($Z = 100$) (1) and hassium ($Z = 108$) (8, 9) and for spherical nuclei at $Z = 114$, $N = 184$.

Direct measurement of the strength of shell effects for SHE nuclei has been beyond experimental capabilities until now. It could only be derived either indirectly from a comparison of, e.g., experimental cross sections and half lives with predicted values, or from measured Q_α values, i.e., energy differences, in alpha decays. Here, we report the direct measurement of the neutron shell gap by precision mass measurements on nobelium ($Z = 102$) and lawrencium ($Z = 103$) isotopes around $N = 152$. The results supply valuable information on the nuclear structure of

SHEs, which is highly relevant for an improved prediction of the island of stability.

Mass spectrometry is a direct probe of nuclear stability, as the mass includes the total binding energy. Until recently, masses in the region of the heaviest elements could only be inferred via α-decay energies. For nuclides with even numbers of protons and neutrons, where the decay connects ground states, this approach is straightforward as the mass of the mother/daughter nucleus can be derived from the measured decay energy $E = \Delta mc^2$ and the mass of the daughter/mother nucleus, respectively. Although the uncertainties add up along decay chains, the masses of several nuclides between uranium ($Z = 92$) and copernicium ($Z = 112$) have been deduced in this way (10).

However, in general, the situation is more complex as α decays preferably connect levels with identical configurations, whereas the ground-state configurations of mother and daughter nuclei usually differ for odd-Z and/or odd-N nuclides. These nuclei decay to excited states that in turn generally de-excite to the ground state by emission of photons or conversion electrons. Thus, the total decay energy is shared among the α particle, γ rays, and/or conversion electrons, i.e., the mere knowledge of the α-particle energy is insufficient. Unfortunately, for such nuclides unambiguous decay schemes, which would provide the information needed to obtain the true Q_α values, are rarely available. For many nuclides above fermium ($Z = 100$), the mass values are only extrapolated with uncertainties of several hundred keV (10).

In contrast, direct mass measurements provide absolute mass values and model-independent binding energies E_B with no need for any ancillary

[1]Helmholtz-Institut Mainz, 55099 Mainz, Germany. [2]GSI Helmholtzzentrum für Schwerionenforschung GmbH, 64291 Darmstadt, Germany. [3]Max-Planck-Institut für Kernphysik, 69117 Heidelberg, Germany. [4]Ruprecht-Karls-Universität, 69120 Heidelberg, Germany. [5]Ernst-Moritz-Arndt-Universität, 17487 Greifswald, Germany. [6]Johannes Gutenberg-Universität, 55099 Mainz, Germany. [7]Justus-Liebig-Universität, 35392 Gießen, Germany. [8]Dipartimento di Fisica and INFN Sezione di Padova, 35131 Padova, Italy. [9]Petersburg Nuclear Physics Institute, Gatchina, 188300 St. Petersburg, Russia. [10]Universidad de Granada, 18071 Granada, Spain. [11]Ludwig-Maximilians-Universität München, 85748 Garching, Germany.

*To whom correspondence should be addressed. E-mail: m.block@gsi.de

Fig. 1. Chart of nuclides above berkelium ($Z = 97$). The blue background shows the calculated shell-correction energies (6). The orange-shaded lines indicate known and predicted shell closures. The squares represent presently known or claimed nuclides. The nobelium and lawrencium isotopes whose masses are reported here are indicated by red squares. The yellow and green squares represent nuclides whose masses are determined by use of these new mass values, respectively, as anchor points in combination with experimental α-decay energies. Hatched squares show nuclides with unknown or ambiguous excited states. For details, see text.

information. Thus, by pinning down members of α-decay chains, they can establish anchor points for a larger region in the chart of nuclei. In addition, accurate mass values define differential quantities such as the two-neutron separation energy $S_{2n}(N,Z) = E_B(N,Z) - E_B(N-2, Z)$ that are sensitive to quantum-mechanical shell effects and can uncover underlying nuclear-structure phenomena.

Direct high-precision mass measurements of short-lived nuclides are best performed with Penning traps (11, 12) by determination of the cyclotron frequency $\nu_c = qB/(2\pi m)$ of the ion of interest with charge q and unknown mass m stored in a homogeneous magnetic field B. We have extended earlier $^{252-254}$No ($Z = 102$) measurements (13, 14) to nuclei with an even larger number of protons and neutrons: ^{255,256}Lr (lawrencium, $Z = 103$) and ^{255}No/^{256}Lr ($N = 153$), respectively. The latter are found on the neutron-rich side of the $N = 152$ shell gap (Fig. 1). Combining the new results with our previous measurements, we can now directly determine the strength of the $N = 152$ shell gap at $Z = 102$, the doorway to the SHEs.

SHIPTRAP (15) at GSI Darmstadt is a Penning-trap mass spectrometer installed behind the velocity filter SHIP, which is known particularly for the discovery of the elements with $Z = 107$ to 112 (16). Nobelium and lawrencium isotopes were produced in fusion reactions of ^{48}Ca projectile ions (accelerated to 218.4 MeV) with ^{206,207,208}Pb and ^{209}Bi targets. The product nuclei were separated from the primary beam by SHIP. Their kinetic energy was reduced from about 40 MeV by Mylar degrader foils and a 2-mg/cm^2 titanium entrance window to the SHIPTRAP gas cell. There, the particles were thermalized in 50-mbar ultrahigh-purity helium. They emerged mainly as doubly charged ions; were cooled, bunched, and accumulated by a radiofrequency-quadrupole ion trap; and then transferred to a 7-T double-Penning-trap system. In the first trap, the ions of interest were selected with a mass-resolving power of up to 10^5. In the second trap, the cyclotron frequency ν_c was determined with the time-of-flight ion–cyclotron-resonance method (17) (compare Fig. 2). At least a few tens of ions must be detected to obtain a resonance. Thus, even for modern Penning traps, the extremely low production rates of exotic nuclei pose a major challenge for high-precision mass measurements. In the case of ^{256}Lr, the present measurements required a long measurement time. With a cross section as low as $\sigma = 60$ nb (18), 93 hours were required for a resonance based on 48 detected ions (Fig. 2).

We determined the mass of the ion of interest by comparing its cyclotron frequency (ν_c) with that of the reference ion ^{133}Cs$^+$ ($\nu_{c,ref}$), with well-known mass (10) and a mass-to-charge ratio close to that of the doubly charged nobelium and lawrencium ions. The statistical uncertainty depends on the number of detected ions per resonance and the Fourier-limited resolution $\Delta\nu_c \approx 1/t$, which is inversely proportional to the excitation time t that a radiofrequency signal is ap-

plied to excite the cyclotron motion of the stored ions. In addition, a systematic uncertainty of 4.5×10^{-8} [based on the residual scattering observed in cross-check measurements with carbon-cluster ions (19)] has been taken into account.

The resulting frequency ratios are given in Table 1. In addition to the confirmation for the even-Z nobelium isotopes ^{252}No and ^{254}No (14) and a further reduction in their uncertainties, accurate mass values were also determined for the odd-Z element lawrencium. Overall, the decay-energy–based values (10) agreed, within their fairly large systematic uncertainties, with our new direct mass measurements of ^{255}No, ^{255}Lr, and ^{256}Lr.

The SHIPTRAP masses provide anchor points of α-decay chains and thus affect the masses of many other nuclides. The mass of ^{255}No determines the masses of its daughters linked by α decay (^{247}Cf) and electron capture (^{247}Bk). Until recently, the nuclear spectroscopy data of

the decay chain from ^{270}Ds (darmstadtium, $Z = 110$) to ^{254}No had been incomplete (20). However, the recent discovery of an α-decay branch of ^{262}Sg (21) now provides the missing link. Thus, the mass excess of ^{270}Ds was experimentally established with an uncertainty of 40 keV. It is the highest-Z anchor point near the deformed doubly magic nucleus ^{270}Hs ($Z = 108$, $N = 162$) (8) (compare Fig. 1). Thus, our measurements affect nuclides in a region reaching into the realm of the SHEs.

These high-precision mass values can be used to benchmark nuclear models (22) and can be extended to the very heavy nuclides. The center of the island of stability around $N = 184$ is experimentally still out of reach, and reliable theoretical predictions are crucial for directing future experimental efforts. The masses measured at SHIPTRAP provide direct, model-independent values of the total binding energies and precise values
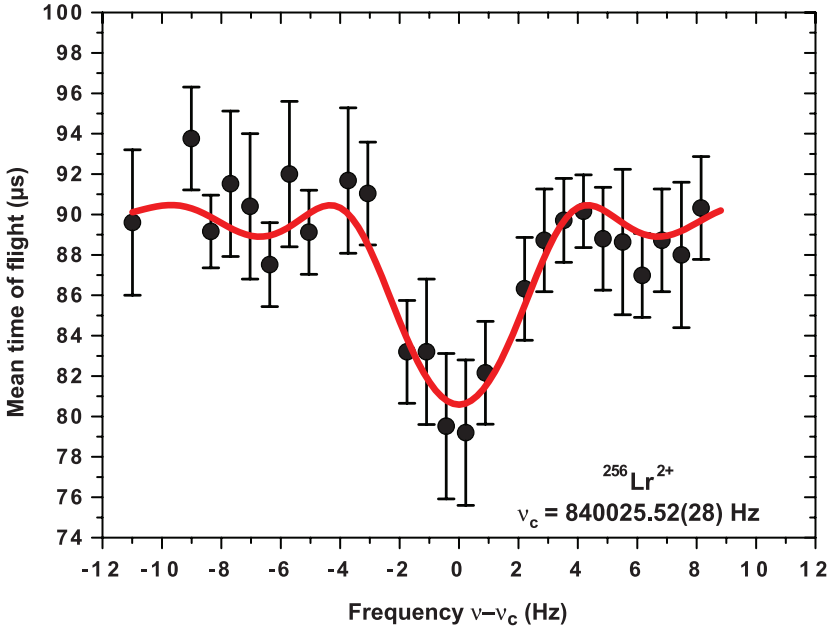
Fig. 2. Time-of-flight ion–cyclotron-resonance of doubly charged ^{256}Lr^{2+} ($t = 200$ ms). The curve is a fit of the expected line shape to the data. Error bars, ±1 SD.

Table 1. Measured frequency ratios and resulting mass-excess [$M_{exc} = M$(atomic mass) − A(atomic mass number) × u(atomic mass unit)] values for the nuclides investigated in this work, as well as theoretical predictions from several models (6, 23–25). The Z and N values of the predicted center of the island of stability by each model are indicated.

Isotope	Frequency ratio	Mass excess (keV)				
	$\nu_{c,ref}/\nu_c$	Experiment SHIPTRAP	FRDM (2) Z = 114 N = 184	MPS-03 (24) Z = 114 N = 184	TW-99 (25) Z = 120 N = 172	SkM* (23) Z = 126 N = 184
^{252}No	0.94837684(7)	82870(16)	82200	82950	91566	95308
^{253}No	0.95214494(5)	84356(13)	83840	84190	−	96396
^{254}No	0.95590852(6)	84726(14)	84050	84700	93646	96989
^{255}No	0.95967902(6)	86808(15)	86550	86700	−	98615
^{255}Lr	0.95969174(6)	89958(16)	89300	89920	−	102326
^{256}Lr	0.9634610(3)	91746(83)	91420	91690	−	103727

for derived quantities such as the shell gap parameter (*23*),

$$\delta_{2n}(N,Z) = S_{2n}(N,Z) - S_{2n}(N+2,Z)$$
$$= -2M_{exc}(N,Z) + M_{exc}(N-2,Z)$$
$$+ M_{exc}(N+2,Z),$$

that theoretical predictions can be confronted with or used to calculate other quantities. $\delta_{2n}(N,Z)$ is a sensitive indicator of shell closures and a measure of their strength and is appropriate for examining shell stabilization for $N = 152$. Because the uncertainties of our results are well below the differences among the predictions by the different models, they allow us to test their predictive power. We have selected as represent-

ative examples two microscopic-macroscopic models—namely, the global FRDM (*6*) and the approach by Muntian *et al.* (*24*) that is optimized locally for SHEs and served to produce the blue-shaded contour plot underlying Fig. 1—as well as a self-consistent mean-field model using the Skyrme-Hartree-Fock effective interaction SkM* (*23*) and, furthermore, a relativistic mean-field model using the effective interaction TW-99 (only even-even nuclei) (*25*).

Microscopic-macroscopic approaches are based on the liquid-droplet model with modifications by a microscopic shell-correction energy (*26*) crucial for the existence of SHEs. These models describe various nuclear properties across the nuclear chart and predict the island of stabil-

ity at $Z = 114$ and $N = 184$. Self-consistent mean-field models use energy-density functionals based on effective nucleon-nucleon interactions. Different effective interactions (e.g., Skyrme and Gogny forces) have been developed, which lead to different predictions for the location of the island of stability, e.g., around $Z = 126$, $N = 184$ for the effective interaction SkM*. In recent years, relativistic mean-field models have been applied. In the TW-99 parameterization, the spherical SHE shells are predicted at $Z = 120$, $N = 172$.

Figure 3 shows a comparison between the predicted and experimental $\delta_{2n}(N,Z)$ values around $N = 152$ for nobelium and lawrencium. Compared to the drastic deviation of the predicted mass excess of up to about 10 MeV from the experimental data (compare Table 1), the agreement of $\delta_{2n}(N,Z)$ is significantly better, with deviations below about 500 keV. Not surprisingly, the local model by Muntian *et al.* agrees best with the data. All models, except for the TW-99 parameterization, show a similar trend with increasing neutron number and a peak indicating the deformed $N = 152$ shell. However, the strength of the shell gap differs strongly. From our data, we obtain $\delta_{2n}(152,102) = 1242(16)$ keV. The macroscopic-microscopic models predict a larger neutron shell gap of 1310 keV (Muntian *et al.*) and 1520 keV (FRDM), whereas the self-consistent mean-field model, SkM*, yields a much smaller and more smeared out shell gap (982 keV). For the TW-99 parameterization, for which only data for even-even nuclei are available, a clear shell gap for $Z = 102$ at $N = 154$ of 1375 keV is obtained, also larger than observed experimentally. The difference in values for the size of the shell gap or even a shift from $N = 152$ to $N = 154$ for one of the selected models illustrates the sensitivity of the different predictions on the used parameterization.

The values of $\delta_{2n}(N,Z)$ obtained from our data confirm the existence of a region of enhanced shell stabilization for nuclides above the doubly magic ^{208}Pb. In particular, for $Z = 102$, our data pin down the shell gap at $N = 152$ accurately. The findings are corroborated for $Z = 103$. Thus, our mass measurements have established, with high accuracy, a shell gap at $N = 152$—a major input for theoretical models, which have not yet converged to a common prediction of the location and the strength of the shell closures in SHEs.

In this study, we have measured the masses of ^{255}No and ^{255,256}Lr directly. Mass uncertainties as low as 15 keV have been achieved, and ^{256}Lr is the heaviest nuclide and the one with the smallest production rate ever investigated at an on-line Penning-trap mass spectrometer. The combination of the present results with spectroscopic data fixes the masses of nuclides as heavy as ^{270}Ds ($Z = 110$). Moreover, the accurate experimental binding energies allow mapping of the shell effect at $N = 152$. Thus, our mass measurements on isotopes with production cross sections on the order of only tens of nanobarn pave the way to a better understanding of the superheavy elements.
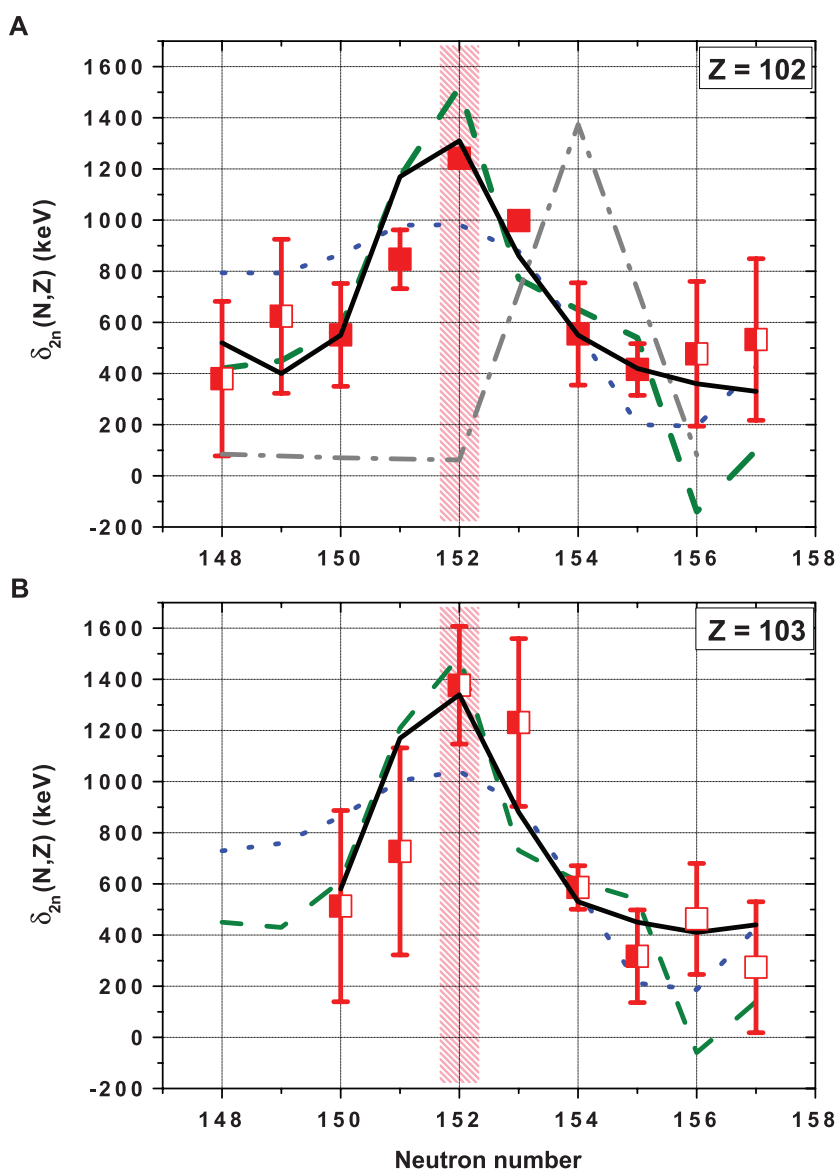
Fig. 3. Experimental shell gap $\delta_{2n}(N,Z)$ (red squares and error bars) and theoretical predictions [dashed green line: Möller (*6*); dotted blue line: SkM* (*23*); black line: Muntian *et al.* (*24*); dash-dotted gray line: TW-99 (*25*), only for (**A**)] for nobelium (**A**) and lawrencium (**B**). For further details, see text. Experimental values have been calculated using one (semi-filled red squares) or two (filled red squares) masses from this work. Values from the AME 2003 are shown by open red squares. The shaded area at $N = 152$ indicates the position of the deformed neutron shell gap. Error bars, ±1 SD.

References and Notes

1. Z. Patyk, A. Sobiczewski, P. Armbruster, K.-H. Schmidt, *Nucl. Phys. A.* **491**, 267 (1989).
2. M. Göppert-Mayer, *Phys. Rev.* **74**, 235 (1948).
3. M. Göppert-Mayer, J. H. D. Jensen, *Elementary Theory of Nuclear Shell Structure* (Wiley, New York, 1955).
4. Yu. Ts. Oganessian *et al.*, *Radiochim. Acta* **99**, 429 (2011).
5. S. Ćwiok, P. H. Heenen, W. Nazarewicz, *Nature* **433**, 705 (2005).
6. P. Möller, J. R. Nix, W. D. Myers, W. J. Swiatecki, *At. Data Nucl. Data Tables* **59**, 185 (1995).
7. M. Bender, K. Rutz, P.-G. Reinhard, J. Maruhn, W. Greiner, *Phys. Rev. C Nucl. Phys.* **60**, 034304 (1999).
8. J. Dvorak *et al.*, *Phys. Rev. Lett.* **97**, 242501 (2006).
9. A. Sobiczewski, K. Pomorski, *Prog. Part. Nucl. Phys.* **58**, 292 (2007).
10. G. Audi, A. H. Wapstra, C. Thibault, *Nucl. Phys. A.* **729**, 337 (2003).
11. L. Schweikhard, G. Bollen, Eds., special issue of *Int. J. Mass Spectrom.* **251** (2006).
12. K. Blaum, *Phys. Rep.* **425**, 1 (2006).
13. M. Block *et al.*, *Nature* **463**, 785 (2010).
14. M. Dworschak *et al.*, *Phys. Rev. C Nucl. Phys.* **81**, 064312 (2010).
15. M. Block *et al.*, *Eur. Phys. J. D* **45**, 39 (2007).
16. S. Hofmann, G. Münzenberg, *Rev. Mod. Phys.* **72**, 733 (2000).
17. G. Gräff *et al.*, *Z. Phys.* **222**, 201 (1969).
18. F. P. Heßberger *et al.*, *Eur. Phys. J. D* **45**, 33 (2007).
19. A. Chaudhuri *et al.*, *Eur. Phys. J. D* **45**, 47 (2007).
20. S. Hofmann *et al.*, *Eur. Phys. J. A* **10**, 5 (2001).
21. D. Ackermann *et al.*, GSI Ann. Rep. 2010–GSI Rep. 2011-1 (2011), p. 200.
22. D. Lunney, C. Thibault, *Rev. Mod. Phys.* **75**, 1021 (2003).
23. K. Rutz *et al.*, *Phys. Rev. C Nucl. Phys.* **56**, 238 (1997).
24. I. Muntian *et al.*, *Act. Phys. Pol. B* **34**, 2073 (2003).
25. W. Zhang, J. Meng, S. Q. Zhang, L. S. Geng, H. Toki, *Nucl. Phys. A.* **753**, 106 (2005).
26. V. M. Strutinsky, *Nucl. Phys. A.* **95**, 420 (1967).

Evidence for NO$_x$ Control over Nighttime SOA Formation

A. W. Rollins,[1]* E. C. Browne,[1] K.-E. Min,[2] S. E. Pusede,[1] P. J. Wooldridge,[1] D. R. Gentner,[3] A. H. Goldstein,[3,4] S. Liu,[5] D. A. Day,[5]† L. M. Russell,[5] R. C. Cohen[1,2]‡

Laboratory studies have established a number of chemical pathways by which nitrogen oxides (NO$_x$) affect atmospheric organic aerosol (OA) production. However, these effects have not been directly observed in ambient OA. We report measurements of particulate organic nitrates in Bakersfield, California, the nighttime formation of which increases with NO$_x$ and is suppressed by high concentrations of organic molecules that rapidly react with nitrate radical (NO$_3$)—evidence that multigenerational chemistry is responsible for organic nitrate aerosol production. This class of molecules represents about a third of the nighttime increase in OA, suggesting that most nighttime secondary OA is due to the NO$_3$ product of anthropogenic NO$_x$ emissions. Consequently, reductions in NO$_x$ emissions should reduce the concentration of organic aerosol in Bakersfield and the surrounding region.

Organic aerosol (OA) constitutes about half of the total submicrometer particulate mass in the troposphere (*1–3*). OA is emitted to the atmosphere both directly as particles (primary OA, POA) and produced in the atmosphere through oxidation of volatile molecules (secondary OA, SOA), although evidence suggests that SOA is dominant (*4*). Owing to the complexity of SOA chemistry, major gaps exist in our ability to predict the time evolution of the chemical, physical, and optical properties of aerosols. A key example is our inability to predict the response of SOA to changes in emissions of nitrogen oxides (NO$_x$). Although laboratory evidence shows that NO$_x$ should substantially affect atmospheric SOA formation, a coherent understanding of the nonlinear SOA/NO$_x$ relationship has not emerged (*5*). This issue is important because NO$_x$ has decreased by 30% or more in the United States and United Kingdom in the last decade, while comparable increases have occurred in China (*6–9*). Direct evidence that these changes in NO$_x$ affect aerosol would greatly aid in the understanding of SOA.

SOA is formed through the gas-phase oxidation of volatile organic compounds (VOCs) by reactions with the hydroxyl radical (OH), ozone (O$_3$), and the nitrate radical (NO$_3$), producing condensable material (*10*). Most laboratory (*10, 11*) and field [e.g., (*2, 12*)] SOA studies have focused on the role of oxidation via O$_3$ and OH as SOA sources. Reactions of organic compounds with NO$_3$ are also important for oxidizing unsaturated atmospheric compounds (*13*), and NO$_3$ is unique in that it is almost exclusively a by-product of anthropogenic NO$_x$ emissions (reaction 1).

$$NO_2 + O_3 \rightarrow NO_3 + O_2 \qquad (1)$$

Due to its photolabile nature and rapid reaction with nitric oxide (NO), NO$_3$ is present primarily in the nighttime atmosphere. Oxidation products of nitrate radical chemistry have a unique chemical signature due to the high yields, to form organic nitrates (RONO$_2$). Organic nitrates are also formed during the day by OH-initiated chemistry in the presence of NO, but with much lower yields. Laboratory studies of SOA from NO$_3$ have revealed both large aerosol yields, and the importance of multigenerational chemistry on compounds with multiple C-C double bonds. For example, Ng *et al.* (*14*) and Rollins *et al.* (*15*) studied the aerosol formed during NO$_3$ oxidation of isoprene. Both studies found large SOA yields (4 to 24%) and showed that the condensable compounds were formed not from the products of the initial NO$_3$ + isoprene reaction, but mostly from further oxidation of the first-generation products. Similar results were found for NO$_3$ + limonene (*16*).

We have developed a fast, sensitive, and precise instrument capable of measuring the particulate total alkyl and multifunctional nitrates (pΣANs) (*17*). Using this instrument, we made observations of pΣANs along with key precursors (NO$_2$, O$_3$, VOC) and aerosol properties in Bakersfield, California, as part of the CalNex-2010 experiment. Bakersfield is of interest due to its location in California's San Joaquin Valley, with abundant sources of biogenic VOC (BVOC) and NO$_x$ and (for the United States) relatively severe particulate matter (PM) air pollution. We interpret the observations as evidence for a substantial nighttime chemical source of pΣAN.

Air parcels arriving at the site had traveled typically through the agricultural San Joaquin Valley, and then through the Bakersfield urban center for 1 to 2 hours before reaching the site. During the experiment, OA concentrations exceeding 10 μg/m^3 were frequently observed at night. A possible contributor to these high concentrations is the reduction in the boundary layer (BL) depth before sunset in the San Joaquin Valley. At a site near Bakersfield, Bianco *et al.* (*18*) observed that during May and June, the BL on average would decrease from ≈1.7 km at noon to ≈300 m just before sunset. The nighttime increase in OA observed in this study, however, occurred after sunset (Fig. 1), and thus after the BL is thought to have reached its minimum depth. We do not know the extent to which the aerosol that we measured at the surface was well mixed through the nocturnal BL; however, the diurnal

[1]Department of Chemistry, University of California, Berkeley, Berkeley, CA 94720, USA. [2]Department of Earth and Planetary Sciences, University of California, Berkeley, Berkeley, CA 94720, USA. [3]Department of Civil and Environmetal Engineering, University of California, Berkeley, Berkeley, CA 94720, USA. [4]Department of Environmental Science, Policy, and Management, University of California, Berkeley, Berkeley, CA 94720, USA. [5]Scripps Institution of Oceanography, University of California, San Diego, San Diego, CA 92093, USA.

*Present address: NOAA Earth System Research Laboratory and Cooperative Institute for Research in the Environmental Sciences, University of Colorado, Boulder, CO 80309, USA.
†Present address: Cooperative Institute for Research in the Environmental Sciences, University of Colorado, Boulder, Boulder, CO 80309, USA.
‡To whom correspondence should be addressed. E-mail: rccohen@berkeley.edu

8.3   Probing the nuclide ^{180}W for neutrinoless double-electron capture exploration, Nuclear Physics A 875 (2012) 1

ELSEVIER

Probing the nuclide ^{180}W for neutrinoless double-electron capture exploration

C. Droese [a],[*],[1], K. Blaum [b], M. Block [c], S. Eliseev [b], F. Herfurth [c],
E. Minaya Ramirez [d], Yu.N. Novikov [e],[f], L. Schweikhard [a],
V.M. Shabaev [f], I.I. Tupitsyn [f], S. Wycech [g], K. Zuber [h], N.A. Zubova [f]

[a] *Institut für Physik, Ernst-Moritz-Arndt-Universität, 17487 Greifswald, Germany*
[b] *Max-Planck-Institut für Kernphysik, Saupfercheckweg 1, 69117 Heidelberg, Germany*
[c] *GSI Helmholtzzentrum für Schwerionenforschung, Planckstraße 1, 64291 Darmstadt, Germany*
[d] *Helmholtz-Institut Mainz, Johannes Gutenberg-Universität, 55099 Mainz, Germany*
[e] *Petersburg Nuclear Physics Institute, Gatchina, 188300 St. Petersburg, Russia*
[f] *St. Petersburg State University, 198504 St. Petersburg, Russia*
[g] *Soltan Institute for Nuclear Studies, PL-00-681 Warsaw, Poland*
[h] *Institut für Kern- und Teilchenphysik, Technische Universität, 01069 Dresden, Germany*

Abstract

The mass difference of the nuclides ^{180}W and ^{180}Hf has been measured with the Penning-trap mass spectrometer SHIPTRAP to investigate ^{180}W as a possible candidate for the search for neutrinoless double-electron capture. The $Q_{\epsilon\epsilon}$-value was measured to 143.20(27) keV. This value in combination with the calculations of the atomic electron wave functions and other parameters results in a half-life of the $0^+ \to 0^+$ ground-state to ground-state double-electron capture transition of approximately 5×10^{27} years$/\langle m_{\epsilon\epsilon}[\text{eV}]\rangle^2$.

[*] Corresponding author. Tel.: +49 6151712114; fax: +49 6151713463.
  E-mail address: c.droese@gsi.de (C. Droese).
[1] Current address: Gesellschaft für Schwerionenforschung Planckstraße 1, 64291 Darmstadt, Germany.

1. Introduction

One of the open questions in elementary particle physics is whether neutrinos are Majorana or Dirac particles. The answer to this question could be given by the observation of neutrinoless double-electron transformations, *i.e.* the double beta-particle emission, double-electron capture of orbital electrons, or a mixture of positron emission and electron capture.

Even though a resonant enhancement of neutrinoless double-electron capture was suggested long ago [1,2], only nowadays the use of Penning traps allows an assessment of different candidate nuclides [3,4]. Based on a very precise $Q_{\epsilon\epsilon}$-value measurement the resonant enhancement factor [2,5]

$$F = \frac{\Gamma_{2h}}{\Delta^2 + \Gamma_{2h}^2/4} \tag{1}$$

can be determined to identify the most suitable candidates. In Eq. (1) Γ_{2h} is the width of the double-electron hole [6] and $\Delta = Q_{\epsilon\epsilon} - B_{2h} - E$ is the degeneracy factor where B_{2h} represents the binding energy of the captured electron pair and E is the energy of the excited state in the daughter nuclide.

Several nuclides that had been listed as candidates [7] have already been probed. As an example, a recent $Q_{\epsilon\epsilon}$ measurement [8] ruled out a resonant enhancement in ^{112}Sn. An even more stringent negative result was obtained for another candidate, ^{74}Se [9,10]. Subsequent Penning-trap measurements of the $Q_{\epsilon\epsilon}$-values of ^{96}Ru, ^{162}Er, ^{168}Yb, and ^{136}Ce also excluded all of them from the list of suitable candidates for the experimental search for neutrinoless double-electron capture [11,12].

More promising candidates for neutrinoless double-electron capture are systems with ground-state to ground-state transitions ($0^+ \to 0^+$) [4]. Their major advantage is a larger nuclear matrix element $M_{\epsilon\epsilon}$ and a larger phase space compared to the ground-state to excited-state transitions. The maximum capture rate is expected if the resonant enhancement criterion is fulfilled for the capture of two K-shell electrons in heavy nuclides. Two candidates for such types of transitions, proposed in [4], have recently been explored with the Penning trap system SHIP-TRAP: ^{152}Gd $\to$ ^{152}Sm [5] and ^{164}Er $\to$ ^{164}Dy [13]. The estimated half-life for ^{152}Gd of 10^{26} years $* \text{eV}/|\langle m_{\epsilon\epsilon}[\text{eV}]\rangle|^2$ ($|\langle m_{\epsilon\epsilon}[\text{eV}]\rangle|$ is the effective Majorana neutrino mass given in electron volts) assesses this nuclide as the best candidate known to date for the search for neutrinoless double-electron capture.

The present study explores the $0^+ \to 0^+$ transition of ^{180}W to ^{180}Hf. This isotope remains the last ground-state to ground-state transition candidate that has not been investigated before our studies. The mass difference $Q_{\epsilon\epsilon}$ given in the Atomic-Mass Evaluation 2003 is 144.4(45) keV [14], which is not accurate enough to evaluate the resonant enhancement factor.

2. Experimental setup

The $Q_{\epsilon\epsilon}$-value of ^{180}W reported here was measured by high-precision Penning trap mass spectrometry with SHIPTRAP [15]. The part of the SHIPTRAP apparatus used for the present measurements is sketched in Fig. 1. All ions were produced via laser ablation from enriched samples (^{180}W metal with 89.1% and ^{180}HfO with 93.89% isotopic enrichment) on a stainless steel backing [16]. The ions were guided with electrostatic lenses and a quadrupole deflector into a tandem Penning trap placed in a 7-T superconducting solenoid.

In the preparation trap possible contaminants were removed by mass-selective buffer-gas cooling [17] from the ion ensemble before it was transferred to the measurement trap, where the
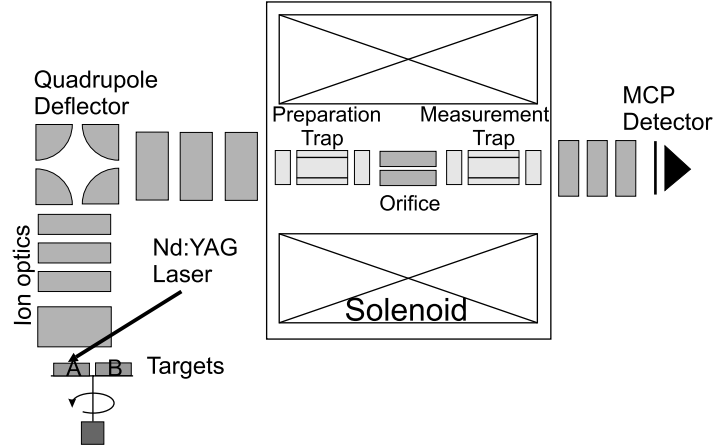
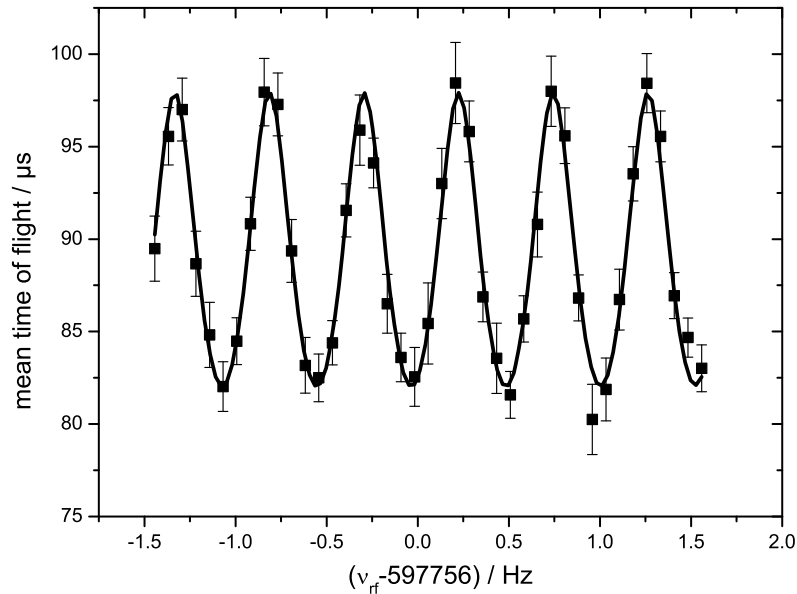Fig. 1. A sketch of the SHIPTRAP setup. For details see text.

Fig. 2. Time-of-flight ion-cyclotron-resonance of ^{180}W$^+$ for a Ramsey-excitation scheme with two excitation pulses of 100 ms separated by a waiting time of 1800 ms. The solid line is a fit of the expected line shape [21] to the data.

cyclotron-frequency measurement of the ion of interest was performed. To this end the time-of-flight ion-cyclotron-resonance (ToF-ICR) technique [18] was utilized to determine the cyclotron frequency $\nu_c = qB/(2\pi m)$ with the magnetic-field strength B and the ion's charge-to-mass ratio q/m. The charged particles were detected by a micro-channel-plate (MCP) detector. A Ramsey-excitation scheme was applied [19,20] using an excitation pattern of two radiofrequency pulses with a duration of 50 ms or 100 ms, separated by a waiting time of 900 ms or 1800 ms, respectively. An example of such a ToF-ICR resonance of ^{180}W$^+$ is shown in Fig. 2.

To determine which is the central minimum of the Ramsey curve, the cyclotron frequency was checked regularly by a single-pulse ToF-ICR measurement with an uncertainty of about 50 mHz.

The resonances of ^{180}W$^+$ and ^{180}Hf$^+$ were taken alternately. For the frequency-ratio determination the cyclotron frequency of one nuclide was linearly interpolated to the time of the measurement of the other one. Thus, due to active stabilization systems [22] any residual magnetic-field fluctuations during the short time between the resonance measurements were negligible. Due to the extremely small mass difference of the two species and the identical ion
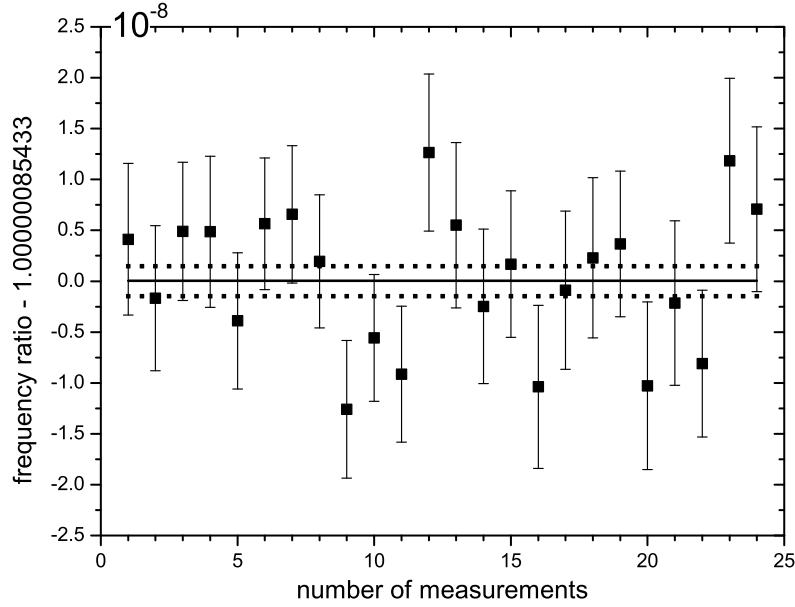
Fig. 3. Frequency ratios $\nu_c(^{180}\text{Hf}^+/^{180}\text{W}^+)$ (points) with the average value (solid line) and the one sigma statistical uncertainty (dotted lines).

production as well as preparation mechanisms systematic uncertainties can be neglected on the present level of statistical uncertainties [23]. Note that no absolute mass values are deduced from the present measurements, but only the mass difference between the two close-lying ion species. For the analysis only those events with an ion number of less than or equal to 5 ions per cycle were considered in order to exclude frequency shifts due to ion–ion interactions [24]. This data was split up into five different subsets according to the number of detected ions per measurement cycle. For each subset a frequency ratio was determined [25]. Those ratios that showed an unreasonably high scattering for different numbers of ions were removed from the measurement.

Further details of the data analysis of $Q_{\epsilon\epsilon}$-value measurements at SHIPTRAP will be given in a forthcoming publication [23].

3. Results

The resulting frequency ratios $\nu_c(^{180}\text{Hf}^+)/\nu_c(^{180}\text{W}^+)$ are shown in Fig. 3. The error bars of the individual data points give the statistical uncertainties. The mean frequency ratio is

$$\nu_c\big(^{180}\text{Hf}^+\big)/\nu_c\big(^{180}\text{W}^+\big) = 1 + 8.5433(165) \times 10^{-7}. \tag{2}$$

The $Q_{\epsilon\epsilon}$-value of the decay is given by

$$\begin{aligned}
Q_{\epsilon\epsilon} &= m\big(^{180}\text{W}\big) - m\big(^{180}\text{Hf}\big) \\
&= \big[m\big(^{180}\text{Hf}\big) - m_e\big] \cdot \left[\frac{\nu_c(^{180}\text{Hf}^+)}{\nu_c(^{180}\text{W}^+)} - 1\right],
\end{aligned} \tag{3}$$

where $m(^{180}\text{Hf})$ is the atomic mass of the daughter nuclide and m_e is the electron mass.

The resulting energy difference between the initial and final species of the double-electron capture transition $^{180}\text{W} \rightarrow {}^{180}\text{Hf}$ is $Q_{\epsilon\epsilon} = 143.20(27)$ keV. The uncertainty of the $Q_{\epsilon\epsilon}$-value is reduced by a factor of 17 in comparison to the old value of $Q_{\epsilon\epsilon} = 144.4(45)$ keV deduced from the mass values given in [14]. The value 131.96(1) keV for the K-shell double-electron
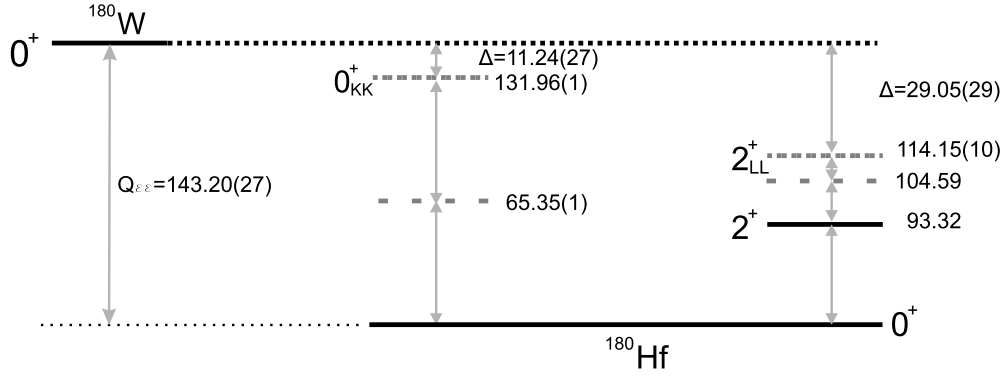
Fig. 4. Partial level scheme of the double-electron capture with the $Q_{\epsilon\epsilon}$-value including the energy difference Δ to the ground-state with the double K-shell electron binding energy 0^+_{KK} and the less favorable excited-state transition to the atomic shell orbitals L_1 and L_3 2^+_{LL} of ^{180}Hf in keV.

hole binding energy B_{2h} was taken from [26]. The degeneracy factor is calculated to be $\Delta = 11.24(27)$ keV. The width of the double-electron hole $\Gamma_{2h} = 71.8$ eV has been deduced from [6]. Thus, the resonance condition is not fulfilled.

Energetically less favorable is the capture to a nuclear excited state in ^{180}Hf with an energy of 93.3243(20) keV [27] and a spin parity of $I = 2^+$. The difference between the mother and daughter states is 29.05(27) keV for the atomic shell orbitals L_1 and L_3 and their binding energies, 11.27 keV and 9.56 keV, respectively. Based on all these parameters the transition to the excited nuclear state is unfavorable. A partial level scheme of the daughter nuclide ^{180}Hf is shown in Fig. 4.

The capture probability was deduced from [26] and is given by

$$\Lambda_{0\nu\epsilon\epsilon} = \frac{2g_A^4 G_F^4 (\cos\theta_c)^4}{(4\pi R)^2} \langle m_{\epsilon\epsilon}\rangle^2 |M_{\epsilon\epsilon}|^2 P_{\epsilon\epsilon} F. \tag{4}$$

In order to estimate $\Lambda_{0\nu\epsilon\epsilon}$ the product of the electron wave functions $P_{\epsilon\epsilon} = |\Psi_{h1}|^2 |\Psi_{h2}|^2$ for two captured electrons h_1 and h_2 in the nucleus was determined using the one-configuration Dirac–Fock method for an extended nucleus [28]. The one-electron densities of the K-shell were calculated for the ground-state of neutral ^{180}W at the center and the root-mean-square radius of the atomic nucleus. Then, the mean value of these densities was used in the calculation of $P_{\epsilon\epsilon}$. The characteristic value $|M_{\epsilon\epsilon}|^2 = 36$ for transitions between heavy nuclides was used [26]. In Eq. (4) g_A stands for the axial–vector nucleon coupling constant, G_F is the weak coupling constant, θ_c is the Cabibbo angle and R is the nuclear radius. As compared to other candidates for neutrinoless double-electron capture the absence of the energy degeneracy is partly compensated by the high values of $P_{\epsilon\epsilon}$ of 3.2×10^{11} and the nuclear matrix element. We estimate the half-life of ^{180}W to

$$T_{1/2} = \frac{\ln 2}{\Lambda_{0\nu\epsilon\epsilon}} \approx \frac{5 \cdot 10^{27}}{|\langle m_{\epsilon\epsilon}[\text{eV}]\rangle|^2} \text{years} * \text{eV}. \tag{5}$$

In [29] a radiative neutrinoless double-electron capture was predicted, particular for the case of ^{180}W. In a simplified description one of the electrons captured from the initial atomic state emits a photon during that capture process. The energy of the emitted photon is equal to the degeneracy factor Δ_{KL}, in which B_{2h} is the binding energy of captured K- and L-shell electrons. The transition probability of the process increases if the energy of the photon is equal to the energy

difference of the atomic states $1S - 2P$. In this particular case, a resonant enhancement of double-electron capture occurs. Thus, the resonance condition for radiative neutrinoless double-electron capture appears when $\Delta_{KL} = E(1S - 2P)$, whereas the resonance condition for the nonradiative transition analysed in this work is fulfilled when Δ_{KK} is approaching the value zero. The transition ^{180}W $\rightarrow$ ^{180}Hf was considered with the new measured value of $Q_{\epsilon\epsilon} = 143.20(27)$ keV. With the formulas presented in [29] we estimated a half-life of 4×10^{27} years $* \mathrm{eV}/|\langle m_{\epsilon\epsilon}[\mathrm{eV}]\rangle|^2$.

4. Summary and conclusion

This work continued the search for a suitable candidate for a future experiment dedicated to the observation of neutrinoless double-electron capture. The focus of this work was on the investigation of the ground-state to ground-state double-electron capture $0^+ \rightarrow 0^+$ in ^{180}W. This transition has a rather large nuclear matrix element, and for the case of two K-shell electron captures has a high overlap of the electron wave functions. Except for the investigated nuclide only a very limited number of possible neutrinoless double-electron capture candidates, *i.e.* ^{152}Gd and ^{164}Er, fulfill these requirements. Here we measured the atomic mass differences of ^{180}W and its daughter nuclide ^{180}Hf resulting in a value of $Q_{\epsilon\epsilon} = 143.20(27)$ keV. Although the obtained value does not result in an energy degeneracy of the mother and daughter states, a rather high neutrinoless double-electron capture probability with a half-life of 5×10^{27} years $* \mathrm{eV}/|\langle m_{\epsilon\epsilon}[\mathrm{eV}]\rangle|^2$ is obtained. For the process of radiative neutrinoless double-electron capture [29] a half-life close to this value of 4×10^{27} years $* \mathrm{eV}/|\langle m_{\epsilon\epsilon}[\mathrm{eV}]\rangle|^2$ was estimated. Both values lie between the results of the other two known ground-state to ground-state transition candidates, which both had already been investigated, ^{152}Gd with a half-life of about 10^{26} years $* \mathrm{eV}/|\langle m_{\epsilon\epsilon}[\mathrm{eV}]\rangle|^2$ and ^{164}Er with 1×10^{30} years $* \mathrm{eV}/|\langle m_{\epsilon\epsilon}[\mathrm{eV}]\rangle|^2$. The theoretical prediction from [26] combined with the experimental results and the matrix element given above yields a half-live of 1.2×10^{28} years $* \mathrm{eV}/|\langle m_{\epsilon\epsilon}[\mathrm{eV}]\rangle|^2$.

Acknowledgements

References

[1] R. Winter, Phys. Rev. 100 (1955) 142.
[2] J. Bernabeu, et al., Nucl. Phys. B 223 (1983) 15.
[3] K. Blaum, Phys. Rep. 425 (2006) 1.
[4] K. Blaum, Yu.N. Novikov, G. Werth, Contemp. Phys. 51 (2010) 149.
[5] S. Eliseev, et al., Phys. Rev. Lett. 106 (2011) 052504.
[6] J. Campbel, T. Papp, At. Data, Nucl. Data Tables 77 (2001) 1.
[7] D. Frekers, arXiv:hep-ex/0506002, 2005.
[8] S. Rahaman, et al., Phys. Rev. Lett. 103 (2009) 042501.
[9] V. Kolhinen, et al., Phys. Lett. B 684 (2010) 17.
[10] B. Mount, et al., Phys. Rev. C 81 (2010) 032501(R).
[11] S. Eliseev, et al., Phys. Rev. C 83 (2011) 038501.
[12] V. Kolhinen, et al., Phys. Lett. B 697 (2011).

[13] S. Eliseev, et al., Phys. Rev. Lett. 107 (2011) 152501.
[14] G. Audi, et al., Nucl. Phys. A 729 (2003) 337.
[15] M. Block, et al., Eur. Phys. J. D 45 (2007) 39.
[16] A. Chaudhuri, et al., Eur. Phys. J. D 45 (2007) 47.
[17] G. Savard, et al., Phys. Lett. A 158 (1991) 247.
[18] G. Gräff, et al., Z. Phys. A 297 (1980) 35.
[19] S. George, et al., Int. J. Mass Spectrom. 264 (2007) 110.
[20] S. George, et al., Phys. Rev. Lett. 98 (2007) 162501.
[21] M. Kretzschmar, et al., Int. J. Mass Spectrom. 264 (2007) 122.
[22] C. Droese, et al., Nucl. Instr. Meth. A 632 (2011) 157.
[23] C. Roux, et al., in preparation.
[24] G. Bollen, et al., J. Appl. Phys. 68 (1990) 4355.
[25] A. Kellerbauer, et al., Eur. Phys. J. D 22 (2003) 53.
[26] M. Krivoruchenko, et al., Nucl. Phys. A 859 (2011) 140.
[27] S. Wu, H. Niu, Nucl. Data Sheets 100 (2003) 483.
[28] V. Bratsev, et al., Bull. Acad. Sci. USSR, Phys. Ser. 41 (1977) 173.
[29] Z. Sujkowski, S. Wycech, Phys. Rev. C 70 (2004) 052501.

8.4 The cryogenic gas stopping cell of SHIPTRAP, Nucl. Instrum. Methods Phys. Res. Sect. B 338 (2014) 126
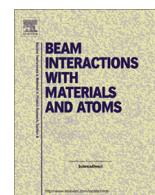
The cryogenic gas stopping cell of SHIPTRAP

C. Droese [a,b,*], S. Eliseev [c], K. Blaum [c], M. Block [d], F. Herfurth [d], M. Laatiaoui [b], F. Lautenschläger [e], E. Minaya Ramirez [b,c], L. Schweikhard [a], V.V. Simon [b], P.G. Thirolf [f]

[a] Ernst-Moritz-Arndt-Universität, Felix-Hausdorff-Straße 6, 17489 Greifswald, Germany
[b] Helmholtz-Institut Mainz, Johannes Gutenberg-Universität, 55099 Mainz, Germany
[c] Max-Planck-Institut für Kernphysik, Saupfercheckweg 1, 69117 Heidelberg, Germany
[d] GSI Helmholtzzentrum für Schwerionenforschung, Planckstraße 1, 64291 Darmstadt, Germany
[e] Technische Universität Darmstadt, Pankratiusstraße 2, 64289 Darmstadt, Germany
[f] Ludwig Maximilians-Universität München, Am Coulombwall 1, 85748 Garching, Germany

ARTICLE INFO

ABSTRACT

The overall efficiency of the Penning-trap mass spectrometer SHIPTRAP at GSI Darmstadt, employed for high-precision mass measurements of exotic nuclei in the mass region above fermium, is presently mostly limited by the stopping and extraction of fusion-evaporation products in the SHIPTRAP gas cell. To overcome this limitation a second-generation gas cell with increased stopping volume was designed. In addition, its operation at cryogenic temperatures leads to a higher gas density at a given pressure and an improved cleanliness of the helium buffer gas. Here, the results of experiments with a ^{219}Rn recoil ion source are presented. An extraction efficiency of 74(3)% was obtained, a significant increase compared to the extraction efficiency of 30% of the present gas stopping cell operated at room temperature. The optimization of electric fields and other operating parameters at room as well as cryogenic temperatures is described in detail. Furthermore, the extraction time of ^{219}Rn ions was determined for several operating parameters.

1. Introduction

Low-energy radioactive ion beams are a prerequisite for many precision experiments in nuclear physics. The efficient transformation of rare ion beams produced in nuclear reactions at high energy with large emittance into low-energy beams with small emittance and low energy spread was a challenge since the first accelerators started operation [1]. In recent years so-called ion-catcher devices have been employed to decelerate high-energy ions in a noble-gas atmosphere, from where they are extracted by gas flow and electric fields. This method is based on the ion-guide isotope-separator on-line (IGISOL) technique, first applied at the IGISOL facility in Jyväskylä [2,3], that provides thermalized ions from fusion-evaporation reactions and proton-induced fission for subsequent experiments. Since its first application in the 1980s, the noble-gas stopping technique has been extended to different nuclear reactions to provide radionuclides of essentially all elements. It is

nowadays utilized in many radioactive beam facilities [4–7] and is also an integral part of some reaccelerators [8].

In a gas stopping cell, reaction products are injected through a solid degrader, in the case of fusion-evaporation products a metallic window with a thickness of a few μm, where they lose most of their kinetic energy. The transmitted ions are thermalized by collisions with buffer-gas atoms at a pressure from tens of mbar up to few bar depending on their kinetic energy. The thermalized ions are then guided by electric fields to an exit hole. There, the ions are transported by a supersonic gas jet into an ion guide, e.g. a radio-frequency-quadrupole (RFQ), that provides the first stage of a differential pumping system and acts as a phase-space cooler for the extracted ions.

The first-generation gas stopping cell, which has been in use at SHIPTRAP since 2005 [9] has a combined efficiency for stopping and extraction of about 12% [10]. An increase of this efficiency is of particular interest for SHIPTRAP, since the cross section for the production of elements above fermium decreases steeply with increasing proton number Z. The isotope ^{256}Lr, for example, can be produced with a cross section of 60 nbarn [11], which resulted in a duration of about 4 days for a mass measurement with 50 ion counts for the present overall efficiency of SHIPTRAP [12] of about

2%. Already for the production of the next element, rutherfordium with $Z = 104$, the cross section decreases to 10 nbarn [13]. Thus, in order to perform direct mass measurements on superheavy elements ($Z \geqslant 104$), it is crucial to increase the overall efficiency of the setup, and hence the efficiency of the buffer-gas stopping cell at SHIPTRAP.

To this end, a second-generation stopping cell (CryoCell) has been developed [14]. Advantages of the new stopping cell in comparison to the first-generation gas cell are the larger stopping volume, the reduced 'dead' volume due to the coaxial injection (see Fig. 1), and the operation at 40 K. In the present gas cell, the ion beam is injected almost perpendicular (82.5°) to the extraction axis. Ions that are stopped between the entrance window and the electrostatic cage are not extracted and, thus, lost.

The operation at cryogenic temperatures provides several advantages, e.g., freezing out of most impurities in the buffer gas, which reduces the chance of ion losses due to charge exchange or molecule formation, and lower diffusion rates reducing losses in radial direction for ions stopped at the edge of the extraction volume (see Section 5.). In this report, the first extraction experiments by use of a ^{219}Rn recoil ion source are described, from which the extraction efficiency and the extraction time are determined.

2. Main components of the experimental setup

A photo of the assembled cryogenic stopping cell is given in Fig. 2. The main components of the CryoCell are shown in the right panel of Fig. 1. The CryoCell consists of two stainless steel chambers: The outer vacuum chamber provides a thermal insulation and contains a multi-layer insulation foil to reduce heat transfer to the inner chamber. The inner chamber is copper-plated on the outside with a layer of 2 mm thickness and is cooled down to approximately 40 K by a cryo cooler (RDK-400B single-stage cold head, Sumitomo Heavy Industries, 54 W at 40 K). The copper layer provides a homogeneous distribution of the temperature over the CryoCell during cooling and warming phases. In addition, the shiny copper layer reduces the radiative load on the inner chamber due to its high reflectivity.

On one end flange of the inner chamber the so-called window flange is mounted (labeled (b) in Fig. 1). It contains the entrance window, which is electrically insulated from the inner chamber and, thus, can be used as an electrode at appropriate voltages. The thickness of the entrance window is chosen such that energetic beam particles, entering the inner chamber through this window, lose ≈90% of their energy. After passing the entrance window, the beam particles are further decelerated by interactions with the
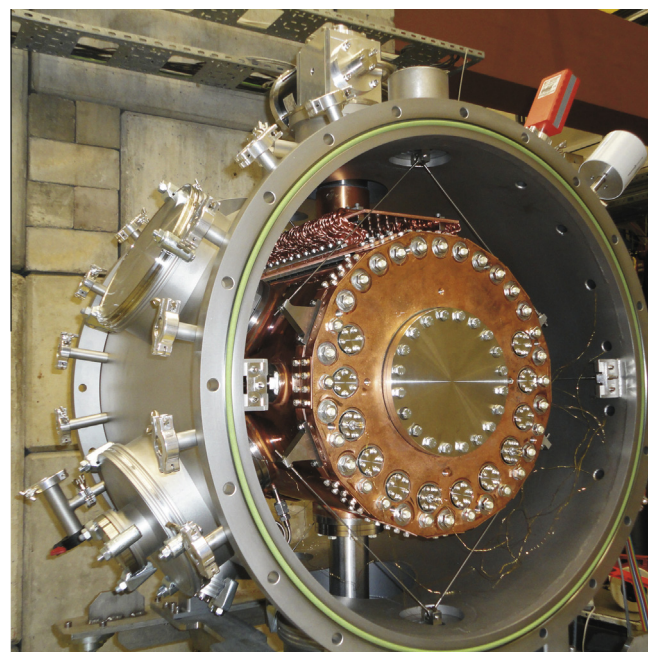

Fig. 2. Photo of the CryoCell. The endflanges on the front of the outer chamber and the multi-layer insulation foil were removed for reasons of visibility. Due to a vacuum test a blind flange was installed in front of the nozzle.

helium buffer-gas atoms. On the same end flange of the inner chamber an electrode system, the DC cage, is mounted. On its 8 ring electrodes voltages are applied that provide a homogeneous electric field. The thermalized ions are guided by the electrostatic field of the DC cage through the buffer gas towards the extraction region.

On the opposing end flange an electrode structure, called RF funnel, is installed, to which an RF voltage as well as a DC voltage gradient can be applied in order to provide a repulsive force that prevents ions from hitting the electrodes. The RF funnel focusses the ions onto the beam axis and guides them towards the exit of the CryoCell.

After passing the RF funnel, the ions are extracted out of the CryoCell in a supersonic gas jet through the extraction nozzle of de Laval type [15]. The extraction nozzle is electrically insulated and a negative potential of a few volts is applied for the extraction of positively charged ions.

2.1. Outer chamber and inner chamber

A schematic overview of the outer-chamber vacuum system is given in Fig. 3. The outer chamber of the CryoCell with a length of 650 mm and a diameter of 500 mm is made of stainless steel. It is evacuated with a 180 l/s turbomolecular pump (Pfeiffer-vacuum TMU 200M) down to pressures below 10^{-6} mbar.

The inner chamber has a length of 450 mm and a diameter of 400 mm. The vacuum vessel is fixed to the outer chamber by 12 spokes made of a Ni/Cr/Fe/Ti/Al alloy (Inconel X-750) with a thickness of 1.6 mm to minimize the heat flow. The inner chamber is wrapped with a multi-layer insulation foil (Coolcat 2, RUAG Space GmbH) to shield it from heat radiation. A cryo cooler is connected on the top of the inner chamber via flexible copper strands to avoid mechanical stress on the inner chamber during the cooling process. The inner chamber is pumped with a 365 l/s turbomolecular pump (Leybold vacuum MAG W 400) that is connected to the vessel via a right-angle all-metal valve and a CF 63 bellow at the bottom of the chamber. The right-angle valve closes the connection of the pump to the vessel when helium gas is injected. Bellows are used at the
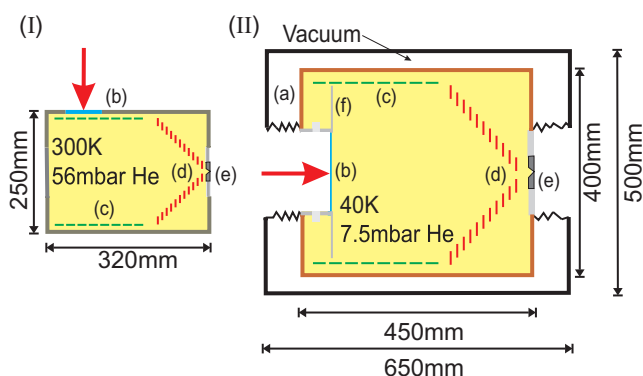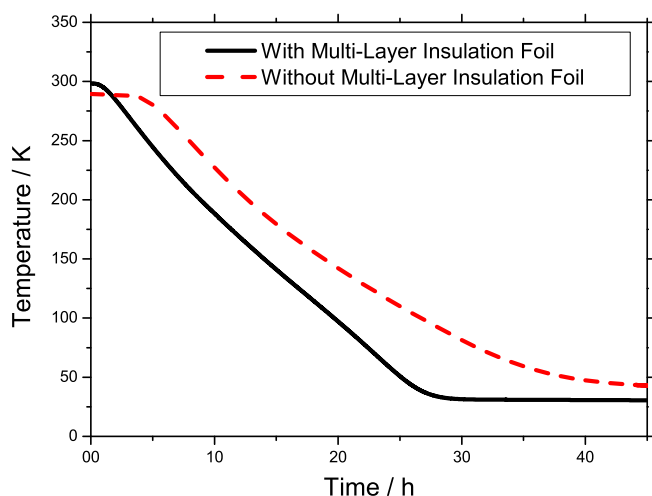

Fig. 1. Schematic comparison between the first-generation gas stopping cell [9] (I) and the cryogenic gas stopping cell (II). The main components of the gas stopping cells are: the outer chamber (a, CryoCell only), the entrance window (b), the electrostatic cage (c), the radio-frequency funnel structure (d), the extraction nozzle (e) and (f, CryoCell only) disc electrode (see Section 2.2). For details see text.
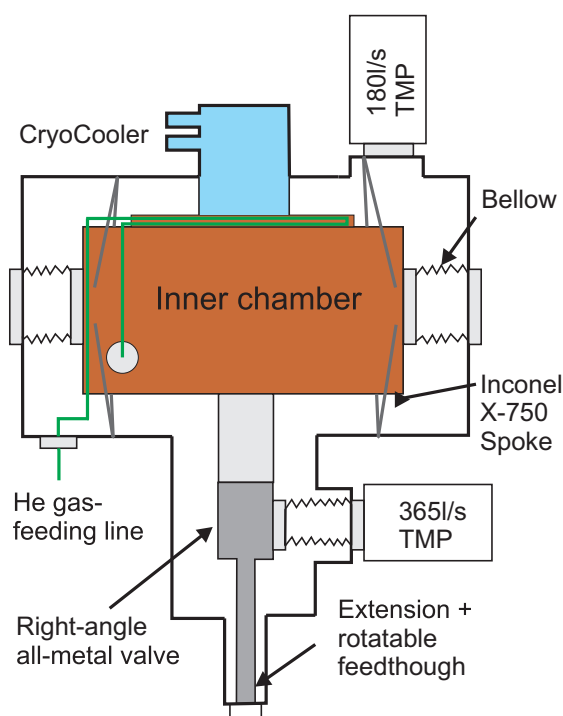
Fig. 3. Schematic overview of the vacuum system of the CryoCell. The multi-layer insulation foil is not displayed in this picture. For details see text.

turbomolecular pump (TMP) and at the entrance and exit of the CryoCell to connect the cold and warm parts of the system with minimal heat transfer. The temperature inside the inner chamber is measured with 8 ceramic-carbon temperature resistors (TMi Cryogenic, 1 kΩ at 300 K).

The volume between the outer and the inner chamber is filled with multi-layer insulation foil in order to reduce the radiative thermal load on the inner chamber. The effects of heat radiation on the cooling time are demonstrated in Fig. 4. There, the system was evacuated (inner chamber pressure $p_{IC} = 1 \cdot 10^{-7}$ mbar) and cooled down with and without the multi-layer insulation foil, respectively. When the multi-layer insulation foil is taken off, the heat radiation increases the cooling time to the steady-state temperature from 29 h to approximately 45 h. The steady-state

temperature rises as well from 35 K to 45 K. Under UHV conditions a temperature gradient of 10 K between the top and the bottom is observed which decreases to less than 1 K in the presence of buffer gas (at a pressure of 7.5 mbar) due to the thermal conductivity of the helium gas.

The composition of the residual gas inside the CryoCell while cooling was monitored with a Quadrupole-Mass-Analyzer (QMA, Pfeiffer Vacuum, Prisma™). To this end, the inner chamber was connected to the QMA with a CF 16 bellow, which is then connected to the outer chamber. The results of the measurement are displayed in Fig. 5. During the cooling procedure, the overall pressure in the CryoCell decreased from $2.5 \cdot 10^{-5}$ mbar at 300 K to $1 \cdot 10^{-8}$ mbar at 40 K. At room temperature, the major components of the residual gas mixture are H_2O and N_2/CO with an abundance of 34% and 36%, respectively. A constant level of water of 3% is present for temperatures smaller than 200 K. The level of N_2/CO in the residual gas decreases steeply as the temperature falls below 65 K. At temperatures of 40 K, the remaining components of the residual gas in the inner chamber are helium and hydrogen, which are not affected by cryo cooling due to their low boiling temperature. The remaining components of N_2/CO, H_2O, O_2 and CO_2 at 40 K arise from the measurement principle of the QMA, which creates ions by electron bombardment. A fraction of the contaminants inside the QMA module operated at 300 K are evaporated from nearby surfaces, ionized and registered even though the cell is operated at 40 K. As Fig. 5 shows, the operation at cryogenic temperatures improves the cleanliness of the system due to freezing out of all components of the residual gas mixture except hydrogen. From extended studies [16] the ratio of the reaction-rate constants for the molecule formation between residual gas molecules $H_2O:O_2:N_2$ was determined to 2500:2.5:1. Therefore, in particular the fraction of water has to be suppressed to avoid ion losses due to molecule formation in the CryoCell.

2.2. Entrance window

Due to the large size of the ion-beam spot in the focal plane [17] of about 50×30 mm^2 for the creation of heavy elements, the entrance window was chosen to have an open diameter of 60 mm. It is made of a metallic foil of a particular thickness, that is selected based on the kinetic energy and the atomic number Z

Fig. 4. Effect of heat radiation on the cooling speed and the steady-state temperature of the inner chamber. The temperature in the inner chamber is shown as a function of time.
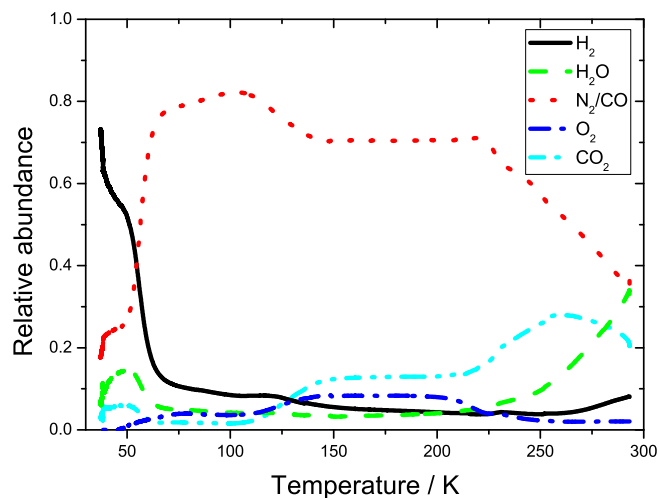
Fig. 5. The relative abundance of the residual gas components as a function of the temperature in the inner chamber. The right-angle all-metal valve (see Fig. 3) was closed and, thus, the system was pumped by the cryo cooling and through the nozzle. For reasons of visibility, helium was excluded from the determination of the relative abundances of the residual gas components. For details see text.
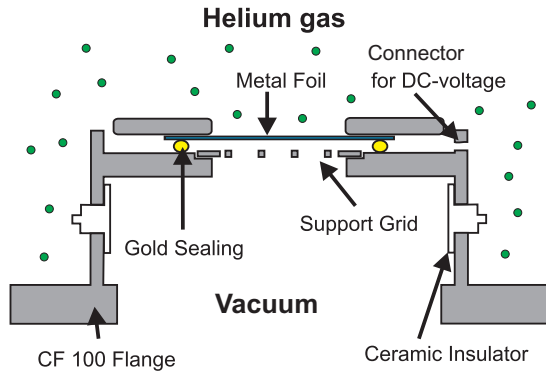
Fig. 6. Schematic view of the entrance window.

of the incoming ions as well as the atomic number of the foil material. With the 'Stopping and Range of Ions in Matter' Code (SRIM) [18] this optimum thickness of the entrance window is determined that leads to a sufficient energy loss during the injection through the foil to stop the majority of ions in the center of the gas catcher for a given buffer-gas pressure. For the recently used reactions, $^{206-208}$Pb(^{48}Ca, 2n)$^{252-254}$No [19], a titanium foil with a thickness of 3.6 μm and homogeneity of ≈±10% was used. The foil is mounted on a customized flange and sealed with a gold wire (see Fig. 6). It is supported by a grid with a geometrical transmission of 95% etched in a stainless steel plate of 1 mm thickness.

The entrance window assembly consists of several different materials with different thermal expansion coefficients. Thus, as the window flange is cooled down, the different components are not contracting uniformly. In order to prevent damages of the foil during the cooling process, it is recommended to use a foil material that is contracting less than the surrounding flange material. The main component, stainless steel, has a relative thermal expansion coefficient of $\beta = 16 \cdot 10^{-6}$ K^{-1} [20], while for gold $\beta = 14.2 \cdot 10^{-6}$ K^{-1} [21]. Titanium with $\beta = 8.6 \cdot 10^{-6}$ K^{-1} [21] is an appropriate choice as foil material, since its contraction is smaller than that of the surrounding material and no stress on the foil is caused. Due to an expansion coefficient close to the surrounding material ($\beta = 13.4 \cdot 10^{-6}$ K^{-1} [21]) nickel can be used as well as foil material. However, in comparison to titanium ($Z = 22$) thinner foils are necessary to obtain the same stopping power due to the larger proton number $Z = 28$, which are technically challenging to manufacture without pinholes.

The entrance window is electrically isolated and a voltage can be applied to optimize the electric field inside the DC cage (Section 2.3). To this end, the window flange consists of two metallic parts separated by a 5 mm thick ceramic insulator. In addition, a disc with a diameter of 270 mm and a concentric hole is connected to the entrance window to further reduce the field distortion by the endflange at ground potential (labeled (f) Fig. 1(II)). From pressure measurements, a leakage rate for the window of $3 \cdot 10^{-4}$ mbar l s^{-1} was estimated, which is acceptable to maintain the required vacuum conditions in the transfer beam line from SHIP to SHIPTRAP.

2.3. DC cage

The DC cage consists of 8 cylindrical stainless-steel electrodes each with a length of 28.4 mm and a diameter of 280 mm (Fig. 7). The distance between neighboring ring electrodes is 1 mm. Thus, the total length of the DC cage is 234.2 mm. The ions are guided downstream by an electrostatic field with a DC gradient of approximately 8 V/cm. In order to generate this gradient, the potentials applied to the first and the last segment, connected to a voltage divider consisting of 7 resistors of 0.1 MΩ inside the inner chamber, are applied via electric vacuum feedthroughs through the outer and inner chamber to the DC cage. In comparison to the mesh construction of the first-generation gas stopping cell [9], the cylindrical design of the electrodes reduces the electric field distortions.

2.4. RF funnel

The RF funnel is an ion guide that consists of 76 individual ring electrodes with a decreasing inner diameter from 266 mm to 5 mm towards the extraction nozzle. The distance between neighboring electrodes as well as their thickness is 1 mm for the first 56 electrodes and 0.5 mm for the last 20 electrodes. Between neighboring electrodes a 180° phase-shifted radio frequency is applied that creates a repulsive electric field force F_{RF} to prevent the ions from hitting the electrodes. Under the assumption of a quadrupole RF field created by a pair of adjacent electrodes in addition with a pair of virtual electrodes the repulsive force [4] on an ion with the mass m in a radius r from the center of the quadrupole field is

$$F_{RF} = -mK^2 \frac{V_{RFFunnel}^2}{d^3}\left(\frac{r}{d}\right). \tag{1}$$
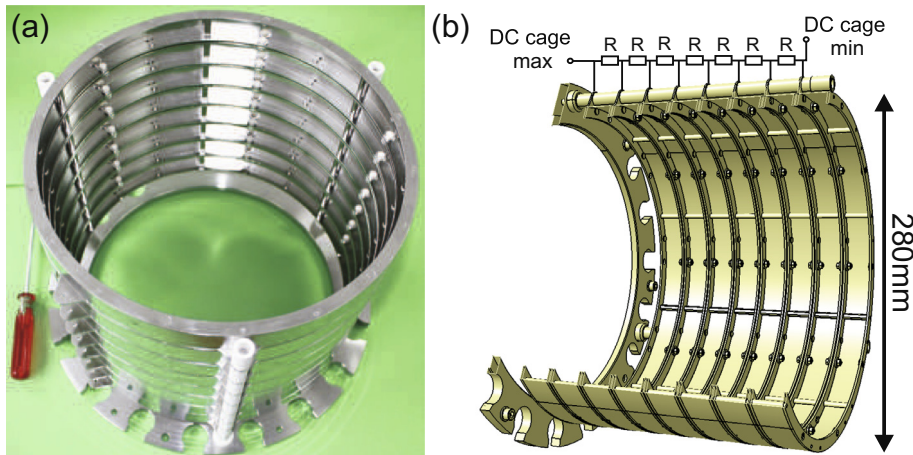

Fig. 7. Photo of the electrode structure called DC cage (a) and view on the 3D model with the circuit of the connected voltage divider (b). The DC cage consists of 8 ring segments connected by a voltage divider with seven resistors with R = 0.1 MΩ each.

Here, d is half of the electrode spacing, $V_{RFFunnel}$ is the applied RF amplitude and K is the ion mobility

$$K = K_0 \frac{T}{T_0} \frac{p_0}{p_{IC}}, \qquad (2)$$

where K_0 is the tabulated reduced mobility, T_0 is the standard temperature of 273.15 K, p_0 is the standard pressure of 1013 mbar and p_{IC} is the inner chamber pressure. In the following, for singly charged radon ions moving in helium, a reduced mobility of $K_0 = 17.37$ cm^2/V s [22] is used. The ions are pushed towards the end of the electrode structure by the electrostatic force F_{DC} created by a DC gradient. For an electric field strength E_{Funnel}, the electric field force, under consideration of the viscous drag force on an ion with the velocity v,

$$F_{DC} = qE_{Funnel} - \frac{qv}{K} \qquad (3)$$

has to overcome the axial component of the repulsive force F_{RF} created by the radio frequency applied to the funnel electrodes. The repulsive force F_{RF} is a local phenomenon in the vicinity of the funnel electrodes while the electrostatic force is constant over the whole funnel electrode structure. Due to the resulting effective force F_{eff}, the charged particles pass the electrode structure along the cone of the funnel and exit through the hole of the last ring electrode. A schematic view is given in Fig. 8.

For each RF phase an RF-/DC-mixing board is installed inside the inner chamber at the funnel to add the RF- and DC voltages. Each mixing board is equipped with 38 surface-mounted device (SMD) coupling capacitors of 220 nF (SMD-PET 0.22 μF 400 VDC, WIMA) and a voltage divider consisting of 27 resistors of 196 kΩ, one resistor of 150 kΩ and 11 SMD resistors of 100 kΩ. The
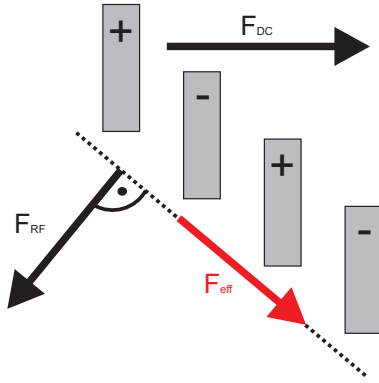
Fig. 8. Radiofrequency of alternating polarity between neighboring electrodes creates a repulsive field force F_{RF} perpendicular to the cone surface of the funnel (dashed line). The resulting effective force F_{eff} guides the ions through the RF funnel.

resistances at the last 20 electrodes were reduced by a factor of two to ensure a homogeneous DC gradient applied to the whole RF funnel. The DC voltages applied to one phase are slightly shifted relative to the other one. As a result, a homogeneous DC gradient is obtained. The circuit layout is shown in Fig. 9.

The resonance circuit is driven by a function generator (Stanford Research Systems DS345), which is connected to an RF amplifier (RM Italy KL500). The signal generator provides a sinusoidal AC voltage with an amplitude of up to 10 V at 50 Ω impedance. An air-core transformer consists of one coil turn on the primary side and ten turns on the secondary side. To reduce the resistance due to the skin effect [23], the secondary coil was wound with a 4 mm diameter copper wire. On the primary side, a copper wire with a diameter of 0.7 mm was used. The large heat conductivity of this wire and the spatial constraints in the inner chamber led to the decision to place the transformer in the outer chamber. The resonance frequency of this circuit with the RF funnel connected is 1014 kHz with a Q factor of 85. The RF funnel has a capacity of 62.6 nF, thus, the inductance of the secondary coil of the transformer is 394 nH. The maximum peak-to-peak voltage for each phase is limited by discharges to 180 V.

2.5. Extraction nozzle

The extraction nozzle (see Fig. 10) connects the high-pressure area of the inner chamber with the low-pressure area of the extraction RFQ. The geometry is based on the nozzle used at the first-generation gas cell. It was shaped according to the results of gas-dynamical simulations with the code VARJET [24]. The nozzle was designed to achieve supersonic velocities of the passing gas particles. The throat has a minimum diameter of 0.6 mm and ends on both sides in a cone. The entrance has a diameter of 2 mm and an opening angle of 90°, while the exit has a diameter of 6 mm and an opening angle of 38°. A DC voltage, depending on the potential applied to 'Funnel DC min' (see Section 4.1), is applied to the nozzle. To this end, the nozzle is electrically insulated from the flange with ceramics suitable for cryogenic temperatures. The nozzle is mounted on a CF 100 flange connected to the end flange of the inner chamber.

The gas velocity at the nozzle throat for given measurement conditions ($p_{IC} = 7.5$ K and $p_{ExtRFQ} = 1.5 \cdot 10^{-2}$ mbar) was estimated with the program 'Aximer' [25] to 600 m s^{-1}. At a constant gas flow of 1 mbar l s^{-1} at room temperature p_{IC} increases to 56 mbar, which results in a drastic increase of the velocity to 1700 m s^{-1}.

2.6. Extraction RFQ

The extraction radio-frequency quadrupole [26] is installed 2 mm behind the nozzle. Its design (as shown in the right panel
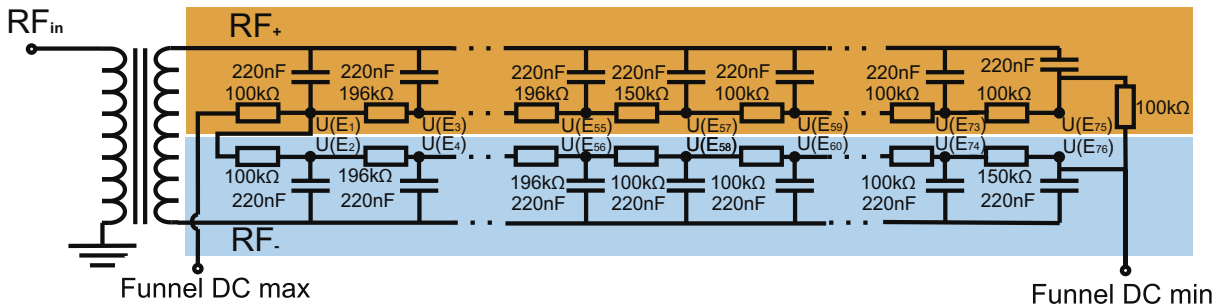
Fig. 9. Circuit layout of the two RF-/DC-mixing boards of the RF funnel indicated by the upper (orange) and lower (blue) rectangles. The amplified signal from the DS345 function generator is connected to 'RF$_{in}$'. The DC voltages are applied via the inputs 'Funnel DC max' and 'Funnel DC min'. The electrodes are connected to the mixing board via the outputs 'U(E$_{1...76}$)'. (For interpretation of the references to color in this figure legend, the reader is referred to the web version of this article.)
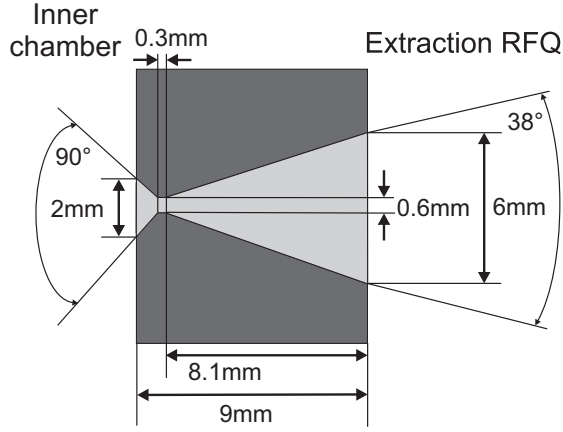
Fig. 10. Sketch of the extraction nozzle.

of Fig. 11) is based on the existing device of the first-generation gas cell [9]. It consists of four 327 mm long stainless steel rods with a diameter of 11 mm, with a distance between opposing rods of $2r_0 = 10$ mm. Between neighboring rods a 180° phase-shifted radio-frequency voltage is applied (see Fig. 11 left). Each rod consists of 16 segments in axial direction. A DC gradient of around 0.2 V/cm is superimposed to the RF voltage to guide the ions downstream. The extraction RFQ is installed in a CF 160 cross piece that is connected to a 1300 l/s turbomolecular pump (Seiko Seiki STP-H1301L1B) via a CF 160 to CF 200 reducer flange.

Similar to the RF funnel, the voltages for the extraction RFQ are provided by a resonance circuit consisting of a signal generator, an RF power amplifier (both the same models as presented in Section 2.4) and a transformer (with ferrite core). The circuit of

the RF-/DC-mixing board is given in Fig. 12. The RF-/DC-mixing board is placed outside the CF 160 cross piece. It is equipped with 32 coupling capacitors of 100 nF and 34 resistors of 196 kΩ. In order to prevent a short circuit between both RF phases, a resistor of 196 kΩ is installed between the first electrode and 'Extraction RFQ DC max' as well as between the last electrode and 'Extraction RFQ DC min' for both phases. In combination with the parasitic capacities introduced by the wires a low-pass filter is formed. The transformer has 8 turns on the primary coil and 75 turns on the secondary coil. The resonance circuit has a resonance frequency of $\nu_{RF} = 940$ kHz and a Q factor of 20.

The total capacity of the resonance circuit is 222 pF, which leads to an inductance of the secondary coil of 129 μH. A peak-to-peak output voltage of $V_{RFExtRFQ} = 300$ V is reached for an input signal of 10 V peak-to-peak. According to Paul [26], stable ion motion in an RFQ without an applied DC voltage is achieved if the parameter

$$q = \frac{eV_{RFExtRFQ}}{2mr_0^2\pi^2\nu_{rf}^2} \qquad (4)$$

of the solution of the Mathieu equation fulfills the condition $0 < q < 0.92$. The properties of the extraction RFQ result in a q value of 0.5 for $^{133}Cs^+$ and 0.2 for singly charged ions with a mass number $A = 300$, which is sufficient for future experiments to be performed at SHIPTRAP.

3. Determination of the extraction efficiency

The main characteristics describing the performance of a gas stopping cell are the stopping and extraction efficiency as well as the extraction time. A quantitative determination of the extraction efficiency ϵ_{ex} has been performed by use of a ^{219}Rn recoil ion source. The decay chain of the isotope ^{223}Ra is shown in Fig. 13.
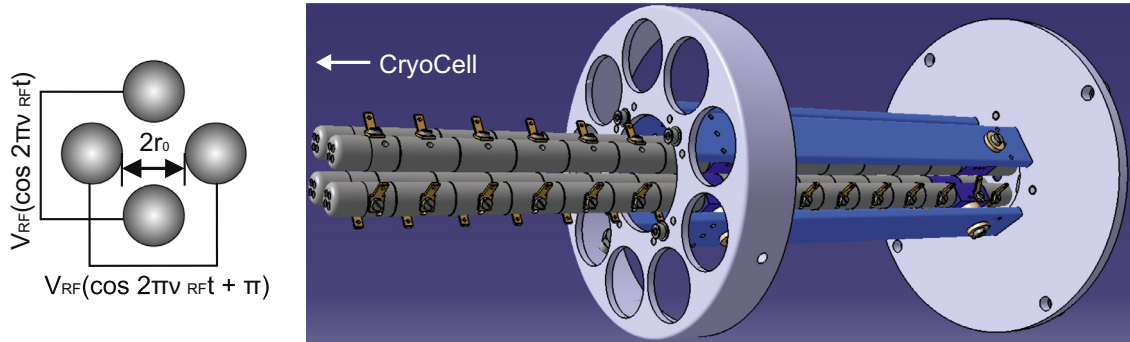

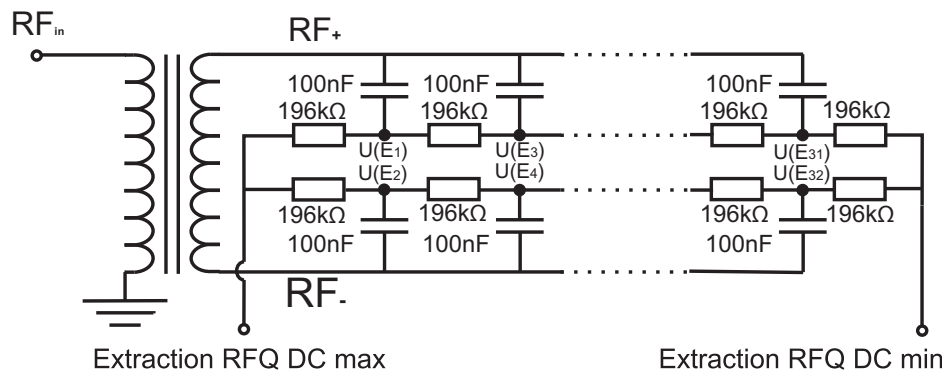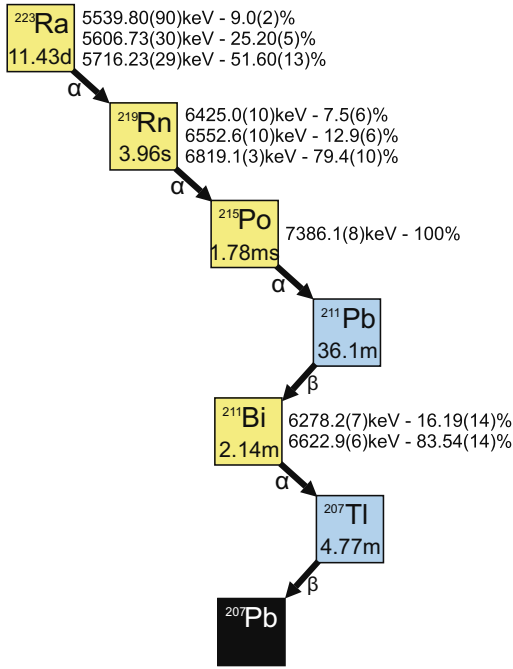**Fig. 11.** Left: Schematic of the RF connection to the rods. Right: CAD model of the extraction RFQ.

Fig. 12. Circuit layout of the RF-/DC-mixing board of the extraction RFQ. The amplified signal from a DS345 function generator 'RF$_{in}$' is connected. The segments of the electrode structure are connected to 'U(E$_{1...32}$)'.

^{223}Ra 11.43d	5539.80(90)keV - 9.0(2)%
	5606.73(30)keV - 25.20(5)%
	5716.23(29)keV - 51.60(13)%

α

^{219}Rn 3.96s	6425.0(10)keV - 7.5(6)%
	6552.6(10)keV - 12.9(6)%
	6819.1(3)keV - 79.4(10)%

α

| ^{215}Po 1.78ms | 7386.1(8)keV - 100% |

α

^{211}Pb 36.1m

β

| ^{211}Bi 2.14m | 6278.2(7)keV - 16.19(14)% |
| | 6622.9(6)keV - 83.54(14)% |

α

^{207}Tl 4.77m

β

^{207}Pb

Fig. 13. The decay chain of ^{223}Ra. The decay modes are indicated by the color of the squares and labeled at the arrows to the corresponding daughter nuclide. The α branching ratio (and the β branching ratio for ^{211}Pb and ^{207}Tl) along this decay chain is ≈100%. The branching ratios between the α-decay energies are given. The decay chain ends at the stable nuclide ^{207}Pb. The half-lives $T_{1/2}$ of the isotopes are given in the squares. The values have been taken from [27]. (For interpretation of the references to color in this figure legend, the reader is referred to the web version of this article.)

The decay spectrum recorded with a silicon detector (Ortec TU-016-150-100) in an evacuated chamber is displayed in Fig. 14. The energy resolution, i.e. the full-width-at-half-maximum (FWHM), was 65 keV, sufficient to separate the relevant alpha lines. From this spectrum, a rate of detected radium alpha particles from the ^{223}Ra decay of 3(0.03) s^{-1} was obtained. For a given distance of 184 mm between the detector and the source and the diameter of 13.8 mm of the mono-crystalline silicon detector used, a total activity $\alpha_{tot}^{Ra} = 8.5(1)$ kBq of the sample was obtained.

For further calculations we assume that the number of emitted α particles from the ^{223}Ra decay is identical to the number of emitted ^{219}Rn recoil ions. The ions emitted into the backward direction are implanted in the backing material of the source and, thus, are not extracted. Therefore, we assume that only the ^{219}Rn recoils released in one hemisphere can be extracted. Thus, the rate of the emitted ^{219}Rn ions is half of the total activity of the source. Considering the half life $T_{1/2}$ of ^{223}Ra (see Fig. 13), the rate of the emitted ^{219}Rn recoil ions after a certain period t since the activity measurement is

$$\alpha_{emitted}^{Rn}(t) = 0.5 \cdot \alpha_{tot}^{Ra} \cdot e^{-\frac{ln2}{T_{1/2}}t} = 0.5 \cdot \alpha_{tot}^{Ra} \cdot 0.5^{t/T_{1/2}}. \quad (5)$$

The calibrated radioactive ion source was installed in the inner chamber of the CryoCell (Fig. 15). The ion source was placed on axis at a distance of about 10 mm from the largest RF funnel electrode. Therefore, the extraction efficiencies presented in the following refer to the axial extraction efficiency.

The detector-/foil-assembly was installed 60 mm behind the extraction RFQ. A 0.8 μm thick aluminum foil with a diameter of 16 mm was installed at a distance of 9 mm in front of the silicon detector. A voltage of −1.7 kV is applied to accelerate the ions towards the foil. According to calculations using the SRIM code [18], the radon recoils will be implanted in a depth of approximately 40 nm into the aluminum foil, which prevents them from diffusing away from the detector before the decay occurs.

In this arrangement the silicon detector observes the alpha particles of the extracted radon ions and of their decay products. Thus, the decay spectra look similar as that of Fig. 14 obtained in an evacuated chamber except for the missing alpha lines of the ^{223}Ra. The alpha lines from ^{211}Bi and ^{219}Rn cannot be fully resolved. Thus, an accurate determination of the number of ^{219}Rn decays is difficult. This problem can be overcome if the ^{215}Po decays are evaluated instead, since the corresponding alpha line is well separated. For the calculation we assume that half of the extracted ^{219}Rn ions create polonium recoils that remain in the aluminum foil. These polonium nuclei can lead to an observable decay. The other half of ^{219}Rn ions is emitted in the hemisphere towards the extraction RFQ and thus are lost. The extraction efficiency is given by

$$\epsilon_{ex} = \frac{2\alpha^{Po}}{\alpha_{emitted}^{Rn}\epsilon^{Det}} = \frac{4\alpha^{Po}}{\alpha_{tot}^{Ra}\epsilon^{Det}0.5^{\frac{t}{T_{1/2}}}}. \quad (6)$$

Considering a detection efficiency of 100% for alpha particles using a silicon detector, the overall detection efficiency ϵ^{Det} is basically given by the solid angle coverage due to the foil and detector size and their distance. The detection efficiency amounts to $\epsilon^{Det} = 16(1)\%$.

4. Extraction efficiency measurements

A schematic overview of the electrode potentials optimized for the determination of the maximum extraction efficiency is given in Fig. 15. All parameters have been optimized at 300 K (in all following figures indicated by black squares) and at 40 K (in all following figures indicated by red circles) for maximum extraction efficiency. The optimum DC voltages are identical for both conditions (see Table 1). The extraction efficiency was measured for a fixed distance from the source to the extraction nozzle of ≈140 mm. To determine the maximum extraction efficiency, the setup was pumped for several days to reduce the residual gas components. A buffer-gas pressure of 56 mbar at 300 K and 7.5 mbar at 40 K, respectively, was applied. A maximum extraction efficiency of 37(3)% at room temperatures and 74(3)% at 40 K was obtained. The operation at cryogenic temperatures described in Section 1 results in an increased extraction efficiency by a factor of 2. It should be noted that no mass separation has been performed. Thus, the fraction of molecules and adducts created in the cell
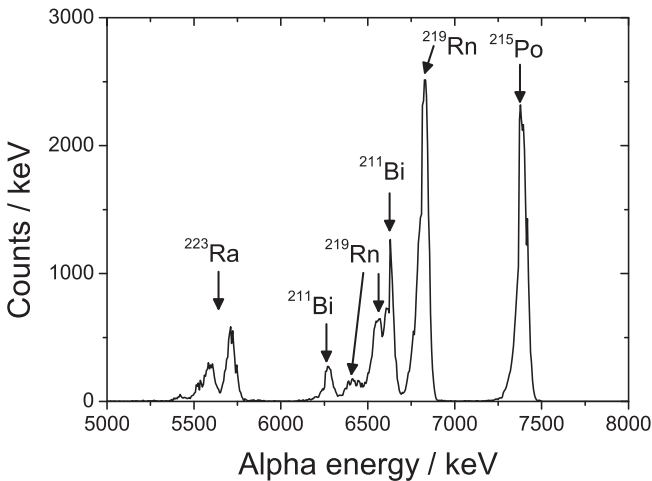
Fig. 14. Alpha decay spectrum of the ^{219}Rn recoil ion source for calibration measurements, accumulated in an evacuated chamber for 3608 s with a silicon detector (Ortec TU-016-150-100). The bin width was 1 keV.
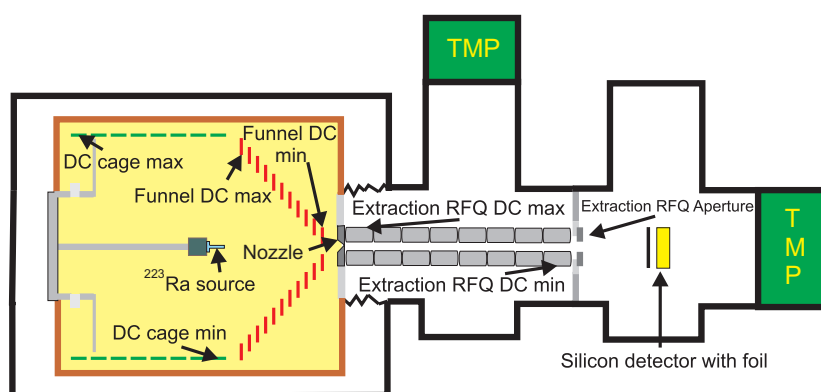
Fig. 15. Schematic of the experimental setup used for the determination of the extraction efficiency and the optimized DC voltages. For details see text.

Table 1
Optimum DC potentials and RF amplitudes applied to the electrodes of the setup for temperatures of 40 K and 300 K.

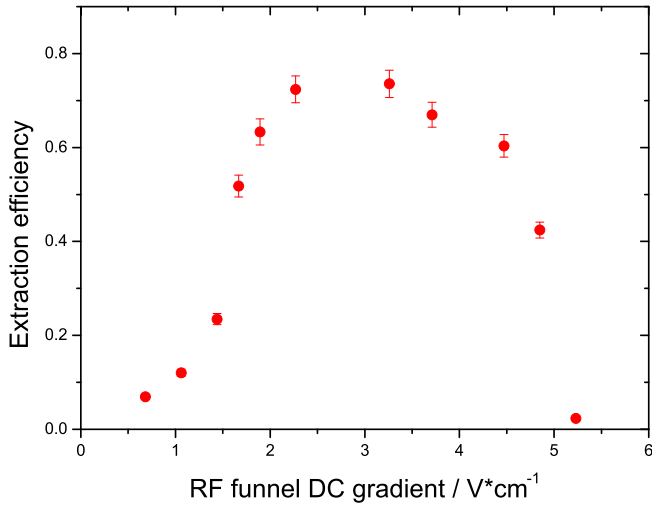| Electrode	U (V)
DC cage max	240
DC cage min	60
Funnel DC max	39
Funnel DC min	−4
Funnel RF	170
Nozzle	−8.6
Extraction RFQ DC max	−20
Extraction RFQ DC min	−30
Extraction RFQ DC aperture	−40
Extraction RFQ RF	200
Si detector foil	−1700

Fig. 16. Extraction efficiency as a function of the voltage difference between the nozzle and the closest RF funnel ring segment at two different operating temperatures.

within the extracted ion sample is unknown. According to earlier investigations [16] the reaction with H_2O is strongly enhanced compared to other residual gas atoms. As pointed out in Section 2.1, the concentration of water in the buffer gas strongly decreases as the system is cooled. Therefore, a smaller fraction of molecules is expected for 40 K in comparison to 300 K.

In this section, we focus on the optimization of the DC potential applied to the extraction nozzle (see Section 4.1) and the DC gradient (see Section 4.2) applied to the RF funnel. Furthermore, the influence of the buffer-gas pressure (see Section 4.3), the temperature (see Section 4.4) and the axial source position (see Section 4.5) on the extraction efficiency was investigated.

4.1. Optimization of the nozzle DC potential

The extraction efficiency as a function of the difference between the DC potential applied to the nozzle and the last ring electrode of the RF funnel, i.e. 'Funnel DC min', for two different buffer-gas temperatures is shown in Fig. 16. Both measurements were performed at a gas flow of 1 mbar l s^{-1}, which results in pressures of 56 mbar and 7.5 mbar at 300 K and 40 K, respectively. The optimum voltage difference of −4.6 V between the nozzle and the last RF funnel electrode is nearly identical for both temperature conditions. Due to an improved cleanliness of the buffer gas, the extraction efficiency increases by a factor of two as the system is cooled down to 40 K. Compared to previous investigations with the first-generation gas stopping cell [9], the optimum voltage difference between the nozzle and the last funnel electrode is remarkably lower. In a previous configuration, the voltage dividers of the RF-/DC-mixing boards were equipped with identical resistors of 196 kΩ each. The reduced electrode spacing at the last 20 electrodes, as well as the reduced electrode thickness doubled the DC
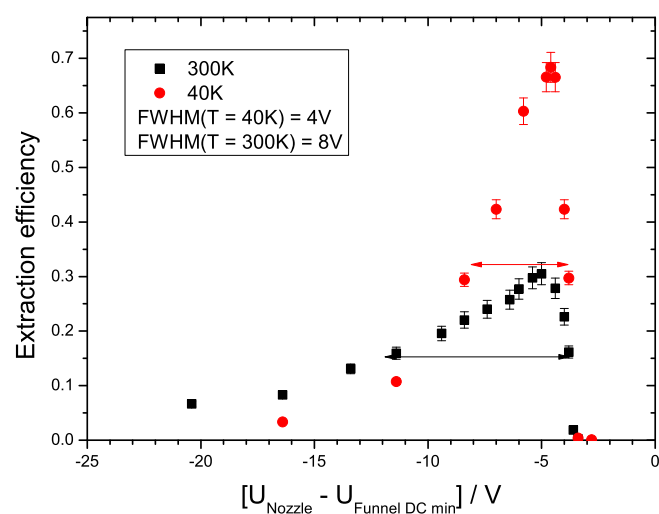
gradient in the area near the entrance nozzle. A reduction of the resistance to 100 kΩ at the last 20 electrodes (see Fig. 9) resulted in a reduced DC gradient in the vicinity of the nozzle. Due to these modifications, the axial ion velocity in front of the nozzle is reduced. In order to match the ion velocity with the gas flow velocity in front of the extraction nozzle, the ions are reaccelerated by a slightly negative DC potential of −8.6 V applied to the nozzle. The FWHM decreases from 8 V at room temperature to 4 V for 40 K, which corresponds to a reduced width of the velocity distribution of the ^{219}Rn ions.

4.2. Optimization of the RF funnel DC gradient

For mass measurements of short-lived nuclei, rapid extraction of the ions from the CryoCell is desired, which can be achieved for instance by large electric field strengths. Due to discharges to the vacuum vessel in the current design, the DC cage gradient is limited to 7.7 V/cm. Faster extraction times can be obtained by increasing the DC gradient applied to the RF funnel. By variation of the voltage 'Funnel DC min', the DC gradient applied to the funnel structure was changed. The DC potentials applied to subsequent electrodes, i.e. 'Nozzle', 'Extraction RF DC max', 'Extraction RFQ DC min' and 'Extraction RFQ aperture' (see Fig. 15) were changed accordingly to maintain identical voltage differences between the electrodes. The results are presented in Fig. 17. For DC

Fig. 17. Extraction efficiency as a function of the DC gradient applied to the RF funnel. Therefore, 'Funnel DC max' was fixed and 'Funnel DC min' was varied. The voltages applied to the downstream electrodes were changed accordingly to maintain equal voltage differences between the electrodes. The measurements were performed with a funnel RF amplitude of 170 V_{pp} at a temperature of 40 K and a buffer-gas pressure of 7.5 mbar. (For interpretation of the references to color in this figure legend, the reader is referred to the web version of this article.)

gradients smaller than about 2 V/cm, F_{DC} is not sufficient to overcome the axial component of the repulsive the force F_{RF}, which is directed away from the nozzle area (see Fig. 8). For values larger than 2.3 V/cm, the superimposed effective force F_{eff} guides the ions towards the nozzle. However, for DC gradients applied to the funnel of more than 3.3 V/cm, F_{RF} is insufficient to push all ions inside the cone of the extraction nozzle, from which they are extracted by the gas jet. This results in a decreasing extraction efficiency.

Larger DC gradients E_{Funnel} at maximum transmission through the RF funnel could be obtained, if the repulsive force F_{RF} would be increased. However, since the maximum RF funnel amplitude is limited by discharges between the neighboring electrodes, a modification towards an RF-carpet system [4,28] is foreseen in the future to reduce the spacing between neighboring electrodes, and, thus, to obtain a larger repulsive RF force.

The DC potentials were optimized for highest extraction efficiency. A DC gradient at the RF funnel (see Fig. 17) of 3.3 V/cm was chosen, which delivers maximum transmission through the electrode structure at the smallest extraction time. Due to the long half life of ^{219}Rn of 3.96 s and the axial position of the ion source, the DC gradient of the electrostatic cage has no influence on the extraction efficiency as long as the gradient is positive and, thus, the ions are guided towards the RF funnel.

4.3. Optimization of the buffer-gas pressure

The energy loss of the energetic beam particles in the buffer-gas filled inner chamber is proportional to the electron density of the stopping material and, thus, the pressure of the helium buffer gas [29] (see Fig. 18). For larger buffer-gas pressures, a shorter range is obtained and the stopping distribution narrows, which results in a higher stopping efficiency. Saturation is obtained when the distribution is smaller than the stopping volume and thus none of the incoming ions collides with the vacuum vessel. For the determination of the stopping efficiency, the ion trajectories of 10,000 ^{205}Rn ions with a point like starting distribution and a kinetic energy of 50 MeV [30] were calculated using the SRIM code [18]. The stopping efficiency is given by the ratio between the ions stopped in the extraction volume of the CryoCell and the initial number of particles.
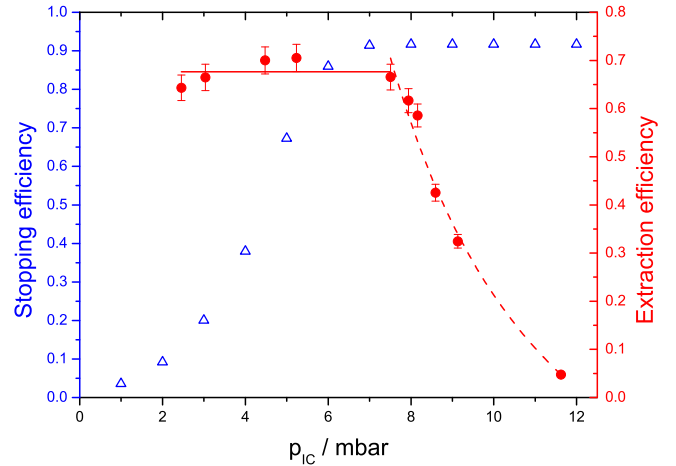
Fig. 18. Simulated stopping and extraction efficiency for DC- and RF-parameters given in Table 1 as a function of the buffer-gas pressure at 40 K. The experimental data (red circles) was fitted with a constant for p_{IC} smaller than 7.5 mbar (solid line) and with an inverse-square fit function (dashed line). The stopping efficiency (open blue triangles) was calculated with the SRIM code [18] for ^{205}Rn ions with a kinetic energy of 50 MeV impinging on a 4.5 μm thick titanium foil.

The correlation between p_{IC} and the stopping and extraction efficiency is shown in Fig. 18. The buffer-gas pressure was varied in a range from 2 mbar to 12 mbar for constant RF-/DC-parameters (see Table 1). Under these conditions pressures smaller than 2 mbar are not accessible due to discharges in the region of the RF funnel and the DC cage. However, we assume that the transmission vanishes for p_{IC} approaching 0 mbar, since the ions are not decelerated by the buffer gas and, thus, collide with the electrodes or walls of the inner chamber. The extraction efficiency is at maximum (about 70%) for all pressures p_{IC} smaller than 7.5 mbar.

In contrast, the stopping efficiency increases with increasing pressure until saturation of approximately 90% is reached for p_{IC} larger than 6 mbar. The remaining 10% of the incoming ^{205}Rn particles are stopped within the entrance window. For buffer-gas pressures exceeding 7.5 mbar, the extraction efficiency strongly decreases. A p_{IC}^{-2} function can be fitted to the data, which corresponds to the correlation between the repulsive funnel force F_{RF} and the buffer-gas pressure p_{IC} (see Eqs. (1) and (2)). Thus, we deduce that the extraction efficiency of the CryoCell for $p_{IC} > 8$ mbar is limited by the performance of the funnel. Due to the reduced mobility for increasing p_{IC}, larger RF amplitudes are necessary to guide the ions inside the cone of the nozzle from which they can be extracted by a supersonic gas jet. Even though the maximum applicable RF amplitude increases for increasing pressures [31], the gain is smaller than the step size of ≈20 V used. For further experiments, the maximum value of p_{IC} that delivers full transmission through the funnel and maximum stopping efficiency is used, i.e. 7.5 mbar.

### 4.4. Effect of the temperature

The influence of the temperature on the extraction efficiency was investigated in more detail in a long-term measurement performed during the cooling process. The results are shown in Fig. 19. The RF-/DC-parameters presented in Table 1 have been applied and the buffer-gas flow was fixed to 1 mbar l s^{-1}, which results in $p_{IC} = 7.5$ mbar at 40 K, (see Fig. 18).

The extraction efficiency increases for decreasing buffer-gas temperatures T. For temperatures smaller than approximately 150 K, the extraction efficiency remains constant within the error bars. In the temperature regime between 300 K and 150 K, the vapor pressure of H_2O is decreasing by 12 orders of magnitude
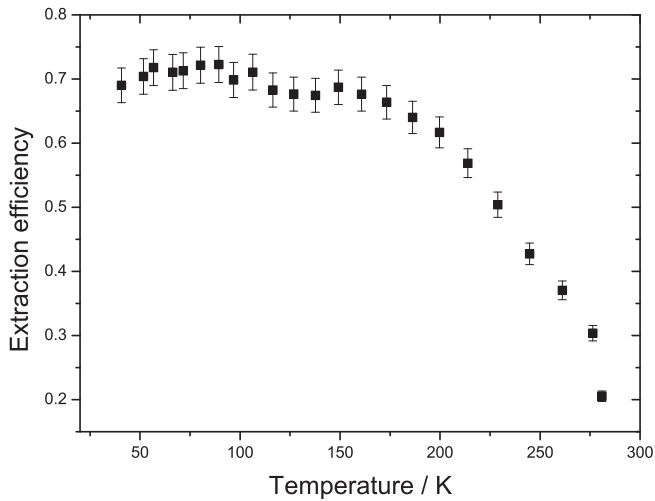
Fig. 19. Extraction efficiency as a function of the buffer-gas temperature. For details see text.
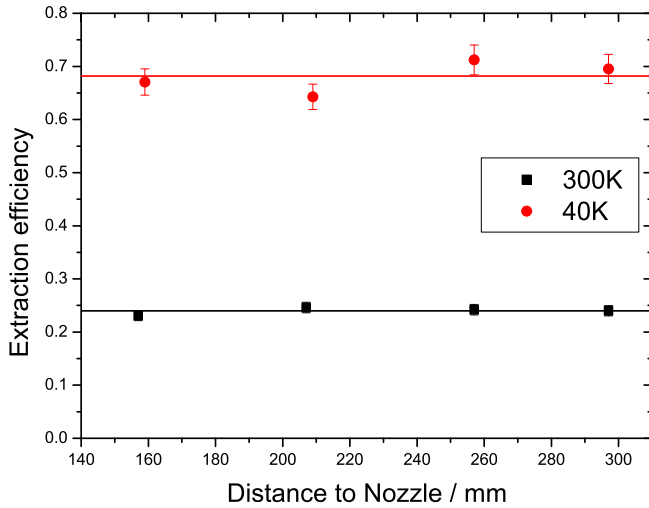
Fig. 20. Extraction efficiency as a function of the distance of the ^{219}Rn recoil ion source from the nozzle. The solid lines represent the mean values of extraction efficiencies.

[32]. The investigation performed with the QMA (see Fig. 5) revealed that water molecules are nearly entirely removed from the residual gas and that the abundance of carbon dioxide is reduced by a factor of two. The other components of the residual gas are not influenced by cryo cooling. Therefore, we deduce that even though ultra-pure helium buffer gas is used, the remaining water still has the largest effect on the extraction efficiency due to its propensity to undergo charge-exchange reactions with charged particles and molecule formation.

4.5. Effect of the axial source position

For the data of Fig. 20 the position of the ion source was varied along the symmetry axis. The DC potential applied to the ion source was matched to the voltage at the closest electrode to minimize the distortion of the electric fields due to the presence of the source.

The investigations revealed that the extraction efficiency for distances between 160 mm and 300 mm from the extraction nozzle is constant within the error bars. Diffusion has no influence on the transmission of ions stopped along the radial symmetry axis neither at 40 K nor at 300 K throughout the whole stopping volume. A discussion of the influence of diffusion on the ions stopped in the CryoCell is given in Section 5.3.

The overall efficiency of the CryoCell is the product of the extraction efficiency and the stopping efficiency of the ions in the extraction volume. In Table 2 the calculated stopping efficiency and the stopping range of three isotopes that have been investigated at SHIPTRAP in previous experiments [30,33,34] are presented for the CryoCell and the first-generation gas cell. After passing an optional Mylar degrader and the titanium window foil, the ions were stopped in He at a pressure of 56 mbar at 300 K. From the stopping distribution, the fraction of the ions stopped in the extraction volume was calculated for the first-generation gas cell (ϵ_{GC}^{stop}) and the CryoCell (ϵ_{CC}^{stop}). However, it has to be noted that the calculation of the stopping efficiency with the SRIM code [18] does not consider ion losses caused by charge-exchange reactions and molecule formation. Moreover, the energy spread of the beam and the beam size have not been taken into account. The increase of the stopping efficiency in CryoCell by a factor of 2 is caused by the larger stopping volume and the vanishing dead volume between the entrance window and the DC cage due to the axial injections of the energetic beam particles.

In Fig. 21, the axial and radial distribution of a typical stopping distribution of ^{205}Rn particles with a kinetic energy of 50 MeV entering a buffer-gas filled volume through a titanium window with a thickness of 4.5 μm was calculated with the SRIM code [18]. The areas shaded in light gray show the axial and radial extent of the stopping volume of the CryoCell and the dark gray shaded area the stopping volume of the first-generation gas cell. Due to the axial injection into the CryoCell, the axial extent of the stopping volume increases drastically in comparison to the first-generation gas cell as reflected by the left panel of Fig. 21. The beam particles stopped within the entrance window appear in the first column.

The right panel of Fig. 21 shows that only a minor gain of the stopping efficiency is obtained due to the larger diameter of the stopping volume for these particular beam conditions. However, in the simulation the source was considered point-like, which is in contrast to the beam of 50×30 mm^2 in the focal plane behind SHIP. Therefore, it can be deduced that the gain of the stopping efficiency due to the larger radial dimension of the CryoCell is larger than the simulation was able to reveal. Including the extraction efficiency of 74(3)% measured with ^{219}Rn ions, an overall efficiency of the cryogenic gas stopping cell of about 67% is anticipated for future on-line experiments. A comparison between the

Table 2
Calculated stopping range L_{SRIM} for three isotopes previously investigated at SHIPTRAP by use of the first-generation gas cell. The isotopes passed through a Mylar degrader foil (thickness Δ_{Mylar}) and the titanium entrance window (thickness Δ_{Ti}) at a buffer-gas pressure of 56 mbar with a kinetic energy E_{kin}. The FWHM of the peak distribution of the stopping range is given in round brackets. The calculated stopping efficiency of the first-generation buffer-gas cell and the CryoCell is given by ϵ_{GC}^{stop} and ϵ_{CC}^{stop}, respectively.

Isotopes	E_{kin} (MeV)	Δ_{Mylar} (μm)	Δ_{Ti} (μm)	L_{SRIM} (mm)	ϵ_{GC}^{stop} (%)	ϵ_{CC}^{stop} (%)	References
^{87}Tc	70	9.5	2.3	152 (78)	45.3	89.6	[33]
^{147}Ho	95	0	7.1	247 (122)	62.2	90.7	[34]
^{205}Rn	50	0	4.5	195 (103)	44.5	91.6	[30]
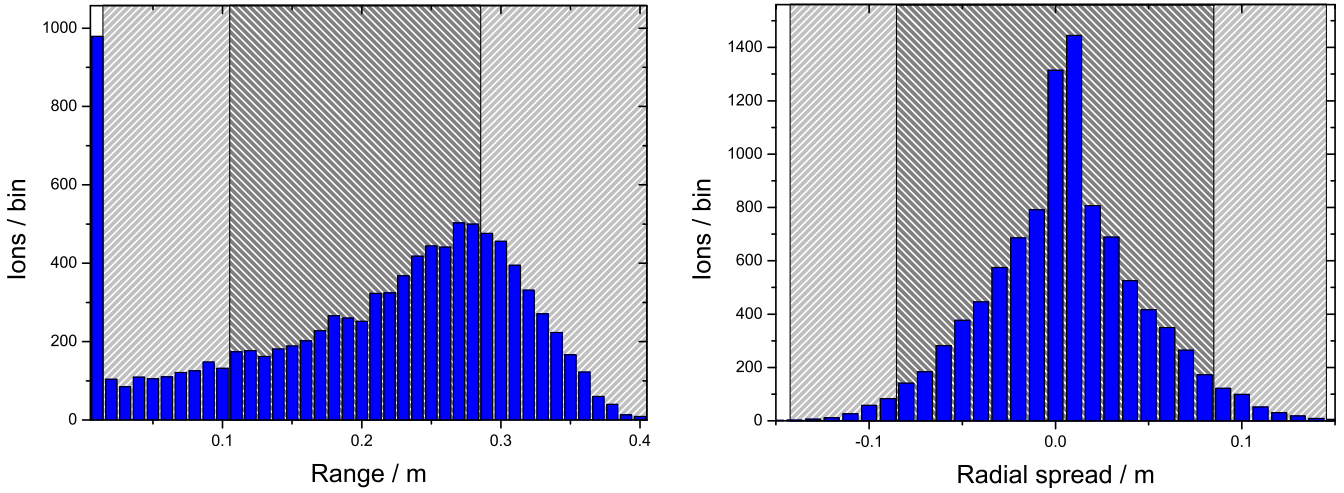
Fig. 21. Calculated axial (left panel) and radial (right panel) stopping distribution with respect to the beam axis of 10,000 [205]Rn particles after passing the titanium foil of 4.5 μm thickness in an helium environment with $p_{IC} = 56$ mbar for 300 K. The light shaded area depicts the extent of stopping volume of the CryoCell and the dark grayish area of the first-generation gas cell. The first bin of axial stopping distribution includes the particles stopped within the entrance window.

Table 3
Comparison of the calculated stopping efficiency ϵ_{stop} for [205]Rn (see Table 2), the extraction efficiency ϵ_{ex} and the overall efficiency ϵ_{tot} between the first-generation gas stopping cell and the CryoCell.

	Gas cell	CryoCell at 40 K
ϵ_{stop}([205]Rn) (%)	44.5	91.6
ϵ_{ex}([219]Rn) (%)	30 [10]	74 (3)
ϵ_{tot} (%)	12 [10]	67 (3)

first-generation gas cell and the CryoCell in terms of efficiency numbers is given in Table 3.

5. Extraction time measurements

Besides low production rates of exotic nuclides, their short half-life provides another challenge for Penning-trap mass spectrometry. To avoid decay losses of short-lived nuclides, a fast extraction from the gas cell is required. According to SIMION simulations, the ions pass the extraction RFQ within a few hundreds of microseconds. Thus, the overall extraction time is mainly determined by the transport through the CryoCell.

5.1. Measurements principle

For a measurement of the extraction time, the voltage applied to the [219]Rn ion source and the RF voltage of the extraction RFQ were pulsed, separated by a variable delay time t_d as depicted in Fig. 22. The recoil energy of the [219]Rn ions is 104 keV. In the presence of buffer gas ($p_{IC} = 7.5$ mbar at 40 K) the recoil ions are thermalized in less than 1 cm. For an ion source potential of -10 V, the thermalized ions are guided backwards onto the source. Thus, the ion source is 'off'. To 'turn on' the ion source its potential was

switched to a positive voltage U_{source} of the same value as its closest electrode in order to assure a homogeneous electric field. For a distance of 110 mm between the nozzle and the ion source $U_{source} = 30$ V. The ions were released for a period of 5 ms in an ion bunch. The extraction RFQ radio-frequency was switched on for 2 ms. The total cycle time was kept at 100 ms, which allowed maximum delay times up to 93 ms. For a period of 1000 s, which corresponds to 10,000 cycles, an alpha decay spectrum for a certain delay time t_d was taken. The delay time was varied and the number of detected [215]Po decays was obtained for each alpha decay spectrum. In Fig. 23 the results of these investigations for one single parameter set is given. The plot shows a Gaussian distribution, which is linked to a variation of the drift time due to the stopping distribution of the [219]Rn ions in the CryoCell and the duration of the ion source pulse. The center of the distribution gives the mean extraction time of 13.7(1) ms for this configuration and source position with a full-width-at-half-maximum of 7.3 ms. The constant background in Fig. 23 arises from residual activity of [219]Rn, still remaining on the foil of the silicon detector from previous investigations, which have been performed in a continuous mode of the source and the extraction RFQ and, therefore, with a larger count rate.

The calculation of the drift time of a path length of 110 mm at an electric field strength of 3 V/cm for a reduced ion mobility $K_0 = 17.37$ cm^2/V s [22] yields a value of 9.7 ms for the given experimental conditions ($T = 300$ K, $p_{IC} = 56$ mbar) which within the delay time distribution of Fig. 23.

5.2. Influence of the buffer-gas pressure

Fig. 24 shows the influence of the pressure on the extraction time for two DC gradients applied to the RF funnel at 300 K and
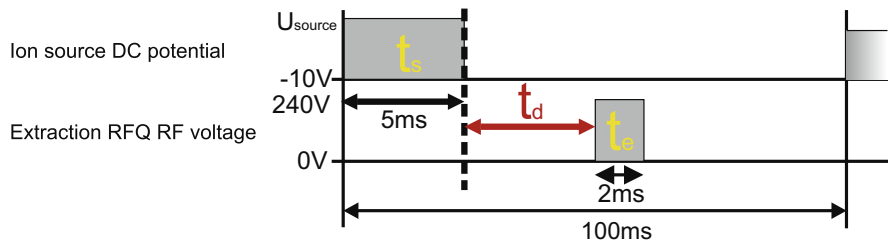
**Fig. 22.** Timing pattern for the extraction-time measurements. For details see text.
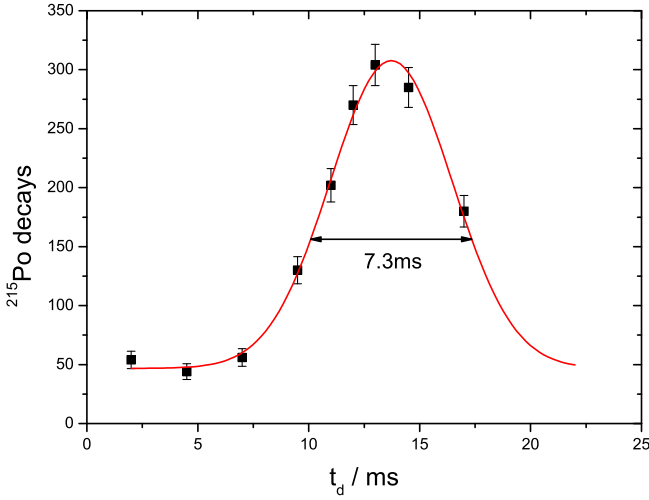
Fig. 23. The number of detected ^{215}Po decays as a function of the delay time t_d between U_{source} (positioned 110 mm from the nozzle) applied to the ion source and the applied extraction RFQ RF for a pressure of 56 mbar at a temperature of 300 K. The DC- and RF-parameters given in Table 1 have been used. The source potential was switched between -10 V and 30 V. The solid line shows a Gaussian fit to the data (red circles). (For interpretation of the references to color in this figure legend, the reader is referred to the web version of this article.)

40 K. The ion source was positioned at a distance of 240 mm from the nozzle and its potential was switched between -10 V and 160 V. For a DC gradient of 3 V/cm, the parameters given in Table 1 have been used. The potential applied to 'Funnel DC min' and the following electrodes along the beamline were increased by 13 V to achieve a funnel DC gradient of 2 V/cm. The extraction time is mainly determined by the sum of the drift times through the DC cage and the RF funnel

$$t = \frac{s_{Cage}T_0 p_{IC}}{K_0 T p_0 E_{Cage}} + \frac{s_{Funnel}T_0 p_{IC}}{K_0 T p_0 E_{Funnel}}, \tag{7}$$

where s_{Cage} and s_{Funnel} represent the distance of the ion trajectory through the DC cage and the RF funnel, respectively. $E_{Cage} = 7.7$ V/cm is the electric field strength applied to the DC cage. For both DC gradients applied to the RF funnel at both temperature conditions the extraction times show a linear dependency on the buffer-gas pressure as described in Eq. (7). Fig. 24 illustrates the strong influence of the buffer-gas pressure on the extraction time. For a DC gradient at the funnel of 3 V/cm the extraction time decreases by a factor of four from 29.4(22.6) ms at 79 mbar to 7.9(6.2) ms for a buffer-gas pressure of 29 mbar. For room temperature conditions it is possible to extract ions out of the CryoCell in less than 10 ms, which gives access to exotic nuclei with short half-lives far away from the valley of stability. However, this would result in a lower stopping efficiency due to the larger range and broader stopping distribution as shown in Section 4.3.

The mobility of the ions is decreasing for decreasing temperatures, which is also reflected by the extraction time measurements. For cryogenic conditions p_{IC} was varied from 4 mbar to 9.5 mbar, corresponding to a room temperature equivalent of 30 mbar and 71.3 mbar. This results in a change of the extraction time from 27.1(7.1) ms to 73.2(14.1) ms. Clearly, the DC gradient applied to the RF funnel has a strong influence on the extraction time, which is observable in the significant increase of the mean extraction time for a DC gradient of 2 V/cm applied to funnel structure. Shorter extraction times can be obtained by larger DC gradients up to 5 V/cm applied to the funnel. However, the maximum transmission is not achievable under these conditions (see Fig. 17).
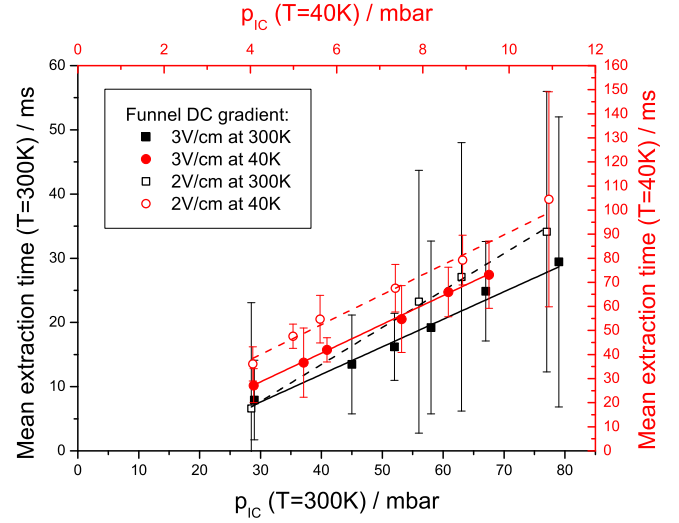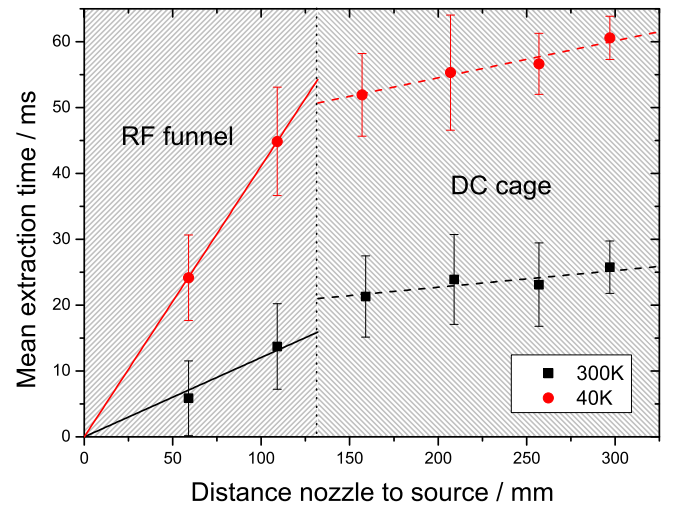

Fig. 24. The mean extraction time as a function of the buffer-gas pressure p_{IC} determined for DC gradients of 3 V/cm (full symbols) and 2 V/cm (open symbols) applied to the RF funnel determined for 300 K (black squares) and 40 K (red circles). According to Eq. (7) linear fits (solid lines for DC gradients of 3 V/cm and dashed lines for DC gradients of 2 V/cm) were applied to the experimental data.

5.3. Variation of the axial positions

The extraction time as a function of the position of the ion source along the radial symmetry axis was measured for 300 K and 40 K. The DC potential applied to the recoil ion source U_{source} was changed according to its position while the remaining RF-/DC parameters were kept constant (see Table 1). The buffer-gas flow was 1 mbar l s^{-1}, resulting in a buffer-gas pressure of 56 mbar at 300 K and 7.5 mbar at 40 K, respectively. The distance between the ion source and the nozzle was varied between 60 mm and 210 mm. The results are given in Fig. 25.

The acceleration of the ions is smaller in the RF funnel than in the DC cage. The mean velocity of ^{219}Rn ions can be extracted from linear fits applied to the data points in Fig. 25. In the funnel region, the mean velocity of the ions is 8 m/s at 300 K and 2 m/s for 40 K,

Fig. 25. The mean extraction time for the RF–DC parameters given in Table 1 as a function of the position of the ^{219}Rn ion source. Linear fits were applied to the data points obtained for different ion source positions inside the RF funnel (solid lines) and the DC cage (dashed lines). The dotted line indicates the end of the funnel structure. (For interpretation of the references to color in this figure legend, the reader is referred to the web version of this article.)

respectively. The mean velocity of the ions passing through the DC cage and the RF funnel is 40 m/s for room temperature and 18 m/s under cryogenic conditions.

Efficient transport through the CryoCell can only be obtained if the extraction time of the ions stopped near the entrance window is shorter than the radial diffusion time t_{diff} until they hit the ring electrodes of the DC cage. The radial distribution of the ion ensemble moving towards the exit nozzle of the CryoCell is mainly caused by diffusion. According to the Einstein relation [35], the diffusion coefficient D of a charged particle with the ion mobility K (see Eq. (2)) can be calculated with

$$D = \frac{Kk_BT}{q} = \frac{K_0 p_0 k_B T^2}{T_0 p_{IC} q}, \tag{8}$$

where k_b is Boltzmann's constant. The coefficient for the diffusion of $^{219}Rn^+$ ions in helium gas at a pressure of 56 mbar at 300 K was calculated with Eq. (8) to $8.92 \cdot 10^{-4}$ m²/s. The diffusion coefficient decreases by a factor of 7.5 to $1.18 \cdot 10^{-4}$ m²/s for a buffer-gas pressure of 7.5 mbar at a temperature of 40 K. The period of a particle diffusing the radial distance r is given by [35]

$$t_{diff} = r/3D. \tag{9}$$

From Fig. 25 an upper limit of the drift time through the DC cage of 15 ms can be deduced. Within this period, the ions are diffusing 2.3 mm radially. Thus, all ions that are stopped at a larger distance from the DC cage electrodes can be extracted. Therefore, ion losses due to diffusion to the DC cage electrodes are not relevant.

6. Summary and outlook

The cryogenic gas cell for SHIPTRAP [14] has been presented in detail. It has been characterized by extraction measurements using a ^{219}Rn recoil ion source. Detailed investigations regarding the DC- and RF parameters have been performed in terms of the optimization of the extraction efficiency. An extraction efficiency of 74(3)% was obtained, which corresponds to an increase by a factor of 2.5 in comparison to the present (first-generation) gas stopping cell [10]. This is linked to the operation at cryogenic temperatures, which improves the cleanliness of the buffer gas and, thus, reduces the probability of molecule formation and neutralization due to charge exchange.

According to calculations using the SRIM code [18], the stopping efficiency increases by a factor of two to approximately 90% due to the larger stopping volume and the axial injection in the CryoCell. Furthermore, the diffusion coefficient is decreased by a factor of 7.5 at 40 K compared to 300 K, which leads to negligible ion losses in radial direction. The overall efficiency is the product of the stopping and extraction efficiency. In the CryoCell an increase of the overall efficiency by a factor of more than 5 to a value of 67% in comparison to the first-generation gas stopping cell with an overall efficiency of 12% is anticipated.

Extended studies have been performed regarding the influence of the electric field strength and the buffer-gas pressure on the extraction time by pulsing the ^{219}Rn ion source and the RF amplitude of the extraction RFQ, separated by a variable delay time. For typical on-line operating conditions of 7.7 V/cm applied at the DC cage and 3.3 V/cm at the RF funnel, a pressure of $p_{IC} = 7.5$ mbar and a temperature of 40 K, extraction times of approximately 60 ms can be obtained for ions stopped in the center of the DC cage. The extraction time reduces to about 24 ms, if the system is operated at 300 K at a buffer-gas pressure of 56 mbar.

Shorter extraction times can be obtained by larger DC gradients applied to the DC cage and the RF funnel. However, the maximum applicable DC gradient at the DC cage is currently limited by gas discharges to 7.7 V/cm. A modified version of the electrode structure would be necessary to apply larger DC gradients.

The DC gradient at the RF funnel was optimized in terms of maximum extraction efficiency. For larger values, the RF field is not sufficient to keep the ions away from the electrodes and to guide them inside the cone of the nozzle from where they are extracted by a supersonic gas jet. The applicable RF amplitude is limited by discharges. The implementation of an RF-carpet system [4,28] with reduced electrode spacing and, thus, larger repulsive field would allow applying larger DC gradients. As a result, the extraction time could be substantially reduced.

However, the main focus of the CryoCell for the operation at SHIPTRAP is the efficient stopping and extraction of the heavy ions. Extraction times in the order of a few tens of milliseconds are sufficient to access the majority of relevant nuclides in the region above fermium, in particular the neutron-rich isotopes.

The functionality of the CryoCell has been successfully demonstrated by the extraction measurements presented in this article. An on-line demonstration of the advantages of the new setup with a high-energy ion beam is planned for the near future.

Acknowledgements

References

[1] Y. Blumenfeld, T. Nilsson, P. Van Duppen, Phys. Scr. T152 (2013) 014023.
[2] J. Äystö et al., Phys. Rev. Lett. 54 (1985) 99.
[3] J. Ärje et al., Nucl. Instr. Meth. Phys. Res. Sec. A 247 (1986) 431.
[4] M. Wada et al., Nucl. Instr. Meth. Phys. Res. Sec. B 204 (2003) 570.
[5] L. Weissman et al., Nucl. Instr. Meth. Phys. Res. Sec. A 540 (2005) 245.
[6] S. Purushothaman et al., Europhys. Lett. 104 (2013) 42001.
[7] W. Plaß et al., Nucl. Instr. Meth. Phys. Res. Sec. B 317 (2013) 457.
[8] G. Savard et al., Nucl. Instr. Meth. Phys. Res. Sec. B 266 (2008) 4086.
[9] J.B. Neumayr et al., Nucl. Instr. Meth. Phys. Res. Sec. B 244 (2006) 489.
[10] S. Eliseev et al., Nucl. Instr. Meth. Phys. Res. Sec. B 258 (2007) 479.
[11] F.P. Heßberger et al., Eur. Phys. J. D 45 (2007) 33.
[12] E. Minaya Ramirez et al., Science 337 (2012) 1207.
[13] F.P. Heßberger et al., Z. Phys. A 359 (1997) 415.
[14] S. Eliseev et al., Nucl. Instr. Meth. Phys. Res. Sec. B 266 (2008) 4475.
[15] T.C. Jen et al., Appl. Therm. Eng. 26 (2006) 613.
[16] Yu. Kudryatsev et al., Nucl. Instr. Meth. Phys. Res. Sec. B 179 (2001) 412.
[17] S. Hofmann, G. Münzenberg, Rev. Mod. Phys. 72 (2000) 733.
[18] J.F. Ziegler, M.D. Ziegler, J.P. Biersack, Nucl. Instr. Meth. Phys. Res. Sec. B 268 (2010) 1818.
[19] M. Block et al., Nature 463 (2010) 785.
[20] <http://www.dew-stahl.com/fileadmin/files/dew-stahl.com/documents/Publikationen/Werkstoffdatenblaetter/RSH/Datenblatt4301UK.pdf> (17.03.2014).
[21] W.M. Haynes, CRC Handbook of Chemistry and Physics, 92nd ed., Taylor and Francis Group, 2011.
[22] L.A. Viehland, Int. J. Ion Mobility Spectrom. 15 (2012) 21.
[23] H. Lamb, Philos. Trans. R. Soc. Lond. 174 (1883) 519.
[24] V.L. Varentsov et al., Nucl. Instr. Meth. Phys. Res. Sec. A 413 (1998) 447.
[25] <http://theknowledgeworld.com/world-of-aerospace/MS-Aximer-Free-Aerospace-Software.htm> (17.03.2014).
[26] W. Paul, Rev. Mod. Phys. 62 (1990) 531.
[27] <http://www.nndc.bnl.gov> (17.03.2014).
[28] S. Schwarz, Int. J. Mass Spectrom. 299 (2011) 71.
[29] H.A. Bethe, Ann. Phys. 397 (1930) 325.
[30] C. Droese et al., Eur. Phys. J. A 49 (2013) 13.
[31] F. Paschen, Ann. Phys. 273 (1889) 69.
[32] P.D. Bentley, Vacuum 30 (1980) 145.
[33] E. Haettner et al., Phys. Rev. Lett. 106 (2011) 122501.
[34] C. Rauth et al., Eur. Phys. J. Special Topics 150 (2007) 329.
[35] G.A. Eiceman, Z. Karpas, H.H. Hill Jr., Ion Mobility Spectrometry, third ed., Taylor and Francis Group, 2014.

Chapter 9

Publications

9.1 Peer-reviewed publications

- M. Block, D. Ackermann, K. Blaum, C. Droese, M. Dworschak, S. Eliseev, T. Fleckenstein, E. Haettner, F. Herfurth, F. P. Heßberger, S. Hofmann, J. Ketelaer, J. Ketter, H.-J. Kluge, G. Marx, M. Mazzocco, Yu. N. Novikov, W. R. Plaß, A. Popeko, S. Rahaman, D. Rodríguez, C. Scheidenberger, L. Schweikhard, P. G. Thirolf, G. K. Vorobyev and C. Weber, *Direct mass measurements above uranium bridge the gap to the island of stability*, Nature 463 (2010) 785

- M. Block, D. Ackermann, K. Blaum, C. Droese, M. Dworschak, M. Eibach, S. Eliseev, T. Fleckenstein, E. Haettner, F. Herfurth, F.P. Heßberger, S. Hofmann, J. Ketelaer, J. Ketter, H.-J. Kluge, G. Marx, M. Mazzocco, Yu.N. Novikov, W.R. Plaß, A. Popeko, S. Rahaman, D. Rodríguez, C. Scheidenberger, L. Schweikhard, P.G. Thirolf, G.K. Vorobyev and C. Weber, *Penning trap mass measurements of trans-fermium elements with SHIP-TRAP*, Hyperfine Int. 196 (2010) 225

- M. Dworschak, M. Block, D. Ackermann, G. Audi, K. Blaum, C. Droese, S. Eliseev, T. Fleckenstein, E. Haettner, F. Herfurth, F. P. Heßberger, S. Hofmann, J. Ketelaer, J. Ketter, H.-J. Kluge, G. Marx, M. Mazzocco, Yu. N. Novikov, W. R. Plaß, A. Popeko, S. Rahaman, D. Rodríguez, C. Scheidenberger, L. Schweikhard, P. G. Thirolf, G. K. Vorobyev, M. Wang, and C. Weber, *Penning trap mass measurements on nobelium isotopes*, Phys. Rev. C 81 (2010) 064312

- C. Droese, M. Block, M. Dworschak, S. Eliseev, G. Marx, E. Minaya Ramirez, D. Nesterenko and L. Schweikhard, *Investigation of the magnetic field fluctuation and implementation of a temperature and pressure stabilization at SHIPTRAP*, Nucl. Instrum. Methods Phys. Res. Sect. A 632 (2011) 157

- S. Eliseev, C. Roux, K. Blaum, M. Block, C. Droese, F. Herfurth, H.-J. Kluge, M. I. Krivoruchenko, Yu.N. Novikov, E. Minaya Ramirez, L. Schweikhard, V. M. Shabaev,

F. Šimkovic, I. I. Tupitsyn, K. Zuber and N. A. Zubova, *Resonant Enhancement of Neutrinoless Double-Electron Capture in ^{152}Gd*, Phys. Rev. Lett. 106 (2011) 052504

- S. Eliseev, C. Roux, K. Blaum, M. Block, C. Droese, F. Herfurth, M. Kretzschmar, M. I. Krivoruchenko, Yu.N. Novikov, E. Minaya Ramirez, L. Schweikhard, V. M. Shabaev, F. Šimkovic, I. I. Tupitsyn, K. Zuber and N. A. Zubova, *Octupolar-Excitation Penning-Trap Mass Spectrometry for Q-Value Measurement of Double-Electron Capture in ^{164}Er*, Phys. Rev. Lett. 107 (2011) 152501

- S. Eliseev, D. Nesterenko, K. Blaum, M. Block, C. Droese, F. Herfurth, Yu.N. Novikov, E. Minaya Ramirez, L. Schweikhard and K. Zuber *Q values for neutrinoless double-electron capture in ^{96}Ru, ^{162}Er, and ^{162}Yb*, Phys. Rev. C 83 (2011) 038501

- S. Eliseev, M. Goncharov, K. Blaum, M. Block, C. Droese, F. Herfurth, E. Minaya Ramirez, Yu. N. Novikov, L. Schweikhard, V. M. Shabaev, I. I. Tupitsyn, K. Zuber and N. A. Zubova *Multiple-resonance phenomenon in neutrinoless double-electron capture*, Phys. Rev. C 84 (2011) 012501(R)

- M. Goncharov, K. Blaum, M. Block, C. Droese, S. Eliseev, F. Herfurth, Yu.N. Novikov, E. Minaya Ramirez, L. Schweikhard and K. Zuber *Probing the nuclides ^{102}Pd, ^{106}Cd and ^{144}Sm for resonant neutrinoless double-electron capture*, Phys. Rev. C 84 (2011) 028501

- C. Droese, K. Blaum, M. Block, S. Eliseev, F. Herfurth, Yu.N. Novikov, E. Minaya Ramirez, L. Schweikhard, V. M. Shabaev, I. I. Tupitsyn, S. Wychech, K. Zuber and N. A. Zubova, *Probing the nuclide ^{180}W for neutrinoless double-electron capture exploration*, Nucl. Phys. A 875 (2012) 1

- E. Minaya Ramirez, D. Ackermann, K. Blaum, M. Block, C. Droese, Ch. E. Düllmann, M. Dworschak, M. Eibach, S. Eliseev, E. Haettner, F. Herfurth, F. P. Heßberger, S. Hofmann, J. Ketelaer, G. Marx, M. Mazzocco, D. Nesterenko, Yu. N. Novikov, W. R. Plaß, D. Rodríguez, C. Scheidenberger, L. Schweikhard, P. G. Thirolf and C. Weber, *Direct Mapping of Nuclear Shell Effects in the Heaviest Elements*, Science 337 (2012) 1207

- D. Nesterenko, K. Blaum, M. Block, C. Droese, S. Eliseev, F. Herfurth, E. Minaya Ramirez, Yu. N. Novikov, L. Schweikhard, V. M. Shabaev, M. V. Smirnov, I. I. Tupitsyn, K. Zuber and N. A. Zubova *Double-β transformations in isobaric triplets with mass numbers A = 124, 130 and 136*, Phys. Rev. C 86 (2012) 044313

- C. Droese, D. Ackermann, L.-L. Andersson,4, K. Blaum, M. Block, M. Dworschak, M. Eibach, S. Eliseev, U. Forsberg, E. Haettner, F. Herfurth, F.P. Heßberger, S. Hofmann, J. Ketelaer, G. Marx, E. Minaya Ramirez, D. Nesterenko, Yu. N. Novikov, W. R. Plaß, D. Rodríguez, D. Rudolph, C. Scheidenberger, L. Schweikhard, S. Stolze, P.G. Thirolf and C. Weber, *High-precision mass measurements of $^{203-207}Rn$ and ^{213}Ra with SHIPTRAP*, Eur. Phys. J. A 49 (2013) 13

- M. Block, D. Ackermann, K. Blaum, C. Droese, Ch. E. Düllmann, M. Eibach, S. Eliseev, E. Haettner, F. Herfurth, F. P. Heßberger, S. Hofmann, G. Marx, E. Minaya Ramirez, D. Nesterenko, Yu. N. Novikov, W.R. Plaß, D. Rodríguez, C. Scheidenberger, L. Schweikhard, P.G. Thirolf and C. Weber, *Extending Penning trap mass measurements with SHIPTRAP to the heaviest elements*, AIP Conf. Proc. 1521 (2013) 191

- S. Eliseev, K. Blaum, M. Block, C. Droese, M. Goncharov, E. Minaya Ramirez, D. A. Nesterenko, Yu.N. Novikov, and L. Schweikhard, *Phase-Imaging Ion-Cyclotron-Resonance Measurements for Short-Lived Nuclides*, Phys. Rev. Lett. 110 (2013) 082501

- E. Minaya Ramirez, D. Ackermann, K. Blaum, M. Block, C. Droese, Ch.E. Düllmann, M. Eibach, S. Eliseev, E. Haettner, F. Herfurth, F.P. Heßberger, S. Hofmann, G. Marx, D. Nesterenko, Yu.N. Novikov, W.R. Plaß, D. Rodríguez, C. Scheidenberger, L. Schweikhard, P.G. Thirolf, C. Weber , *Recent Developments for High-precision Mass Measurements of the Heaviest Elements with SHIPTRAP*, Nucl. Instrum. Methods Phys. Res. Sect. B 317 (2013) 501

- C. Roux, K. Blaum, M. Block, C. Droese, S. Eliseev, M. Goncharov, F. Herfurth, E. Minaya Ramirez, D. Nesterenko and Y. N. Novikov and L. Schweikhard, *Data analysis of Q-value measurements for double-electron capture with SHIPTRAP*, Eur. Phys. J. D 67 (2013) 146

- C. Droese, S. Eliseev, K. Blaum, M. Block, F. Herfurth, M. Laatiaoui, F. Lautenschläger, E. Minaya Ramirez, L. Schweikhard, V.V. Simon and P.G. Thirolf, *The cryogenic gas stopping cell of SHIPTRAP*, Nucl. Instrum. Methods Phys. Res. Sect. B 338 (2014) 126

- S. Eliseev, K. Blaum, M. Block, A. Dörr, C. Droese, T. Eronen, M. Goncharov, M. Höcker, J. Ketter, E. Minaya Ramirez, D. A. Nesterenko, Yu. N. Novikov and L. Schweikhard, *A phase-imaging technique for cyclotron-frequency measurements*, Appl. Phys. B 114 (2014) 107

- D. Nesterenko, S. Eliseev, K. Blaum, M. Block, S. Chenmarev, C. Droese, P. Filyanin, M. Goncharov, E. Minaya Ramirez, Yu.N. Novikov, L. Schweikhard, and V. V. Simon, *Direct measurement of the atomic mass difference of ^{187}Re and ^{187}Os for the determination of the neutrino mass*, to be submitted to Phys. Rev. C

9.2 Miscellaneous, non-peer reviewed publications

- M. Dworschak, D. Ackermann, K. Blaum, M. Block, C. Droese, S. Eliseev, E. Haettner, F. Herfurth, F.P. Heßberger, S. Hofmann, J. Ketelaer, G. Marx, D. Nesterenko, Yu. Novikov, W.R. Plaß, A. Popeko, D. Rodríguez, C. Scheidenberger, L. Schweikhard, P. Thirolf and C. Weber, *Towards a direct mass measurement of ^{255}Lr at SHIPTRAP*, GSI SCIENTIFIC REPORT 2009 NUSTAR-SHE-07

- D. Rudolph, M. Block, F.P. Heßberger, D. Ackermann, L.-L. Andersson, M.L. Cortes, C. Droese, M. Dworschak, M. Eibach, U. Forsberg, P. Golubev, R. Hoischen, J. Ketelaer, I. Kojouharov, J. Khuyagbaatar, D. Nesterenko, H. Schaffner, S. Stolze and the SHIP-TRAP collaboration, *TRAPSPEC – Towards Isotope-Selected Decay Spectroscopy*, GSI SCIENTIFIC REPORT 2009 NUSTAR-SHE-08

- M. Block, D. Ackermann, K. Blaum, C. Droese, Ch. E. Düllmann, M. Dworschak, M. Eibach, S. Eliseev, A. Gonschior, E. Haettner, F. Herfurth, F.P. Heßberger, S. Hofmann, J. Ketelaer, G. Marx, M. Mazzocco, E. Minaya Ramirez, D. Nesterenko, Yu. Novikov, W. R. Plaß, D. Rodríguez10, C. Scheidenberger, L. Schweikhard, P. Thirolf and C. Weber, *Mass Measurements of No and Lr isotopes with SHIPTRAP*, GSI SCIENTIFIC REPORT 2010 PHN-NUSTAR-SHE-02

- E. Minaya Ramirez, D. Ackermann, K. Blaum, M. Block, C. Droese, Ch. E. Düullmann, M. Dworschak, M. Eibach, S. Eliseev, E. Haettner, F. Herfurth, F.P. Heßberger, S. Hofmann, J. Ketelaer, J. Ketter, G. Marx, D. Nesterenko, Yu. Novikov, W.R. Plaß, D. Rodríguez, C. Scheidenberger, L. Schweikhard, P.G. Thirolf, G.K. Vorobjev and C. Weber, *Mass Measurements of heavy actinides with SHIPTRAP*, GSI SCIENTIFIC REPORT 2011 PHN-NUSTAR-SHE-07

- L.-L. Andersson†, M. Block, D. Rudolph, D. Ackermann, H.G. Burkhard, C. Droese, C. Fahlander, U. Forsberg, P. Golubev, F.P. Heßberger, J. Jeppsson, I. Kojouharov, M. Laatiaoui, R. Mändl, J. Maurer, E. Minaya Ramirez, L.G. Sarmiento, T. Schäfer, H. Schaffner, and M. Smirnov, *A study of the possibilities and limitations of the TRAPSpec setup*, GSI SCIENTIFIC REPORT 2011 PHN-NUSTAR-SHE-09

- S. Eliseev, K. Blaum, M. Block, C. Droese, M. Goncharov, F. Herfurth, E. Minaya Ramirez, D. Nesterenko, Yu.N. Novikov, C. Roux, L. Schweikhard and K. Zuber, *Search for a resonant enhancement of neutrinoless double electron capture with SHIPTRAP*, GSI SCIENTIFIC REPORT 2011 PHN-NUSTAR-SHE-10

- R. R. Mändl, D. Ackermann, J. Adamczewski-Musch, L.-L. Andersson, M. Block, H.-G. Burkhard, V. Comas, C. Droese, S. Heinz, F. P. Heßberger, J. Hoffmann, S. Hofmann, N. Kurz, M. Laatiaoui, J. Maurer, E. Minaya Ramirez, K. Schmidt and L. Zimmermann, *Implementation of a digital data readout system for double sided silicon strip detectors for ion and alpha particle spectroscopy*, GSI SCIENTIFIC REPORT 2011 PHN-NUSTAR-SHE-17

- C. Droese, K. Blaum, M. Block, S. Eliseev, F. Herfurth, M. Laatiaoui, F. Lautenschläger, E. Minaya Ramirez, L. Schweikhard and P. G. Thirolf, *Commissioning of a cryogenic gas cell for ion stopping at SHIPTRAP*, GSI SCIENTIFIC REPORT 2011 PHN-NUSTAR-SHE-18

- C. Droese, K. Blaum, M. Block, S. Eliseev, F. Herfurth, M. Laatiaoui, F. Lautenschläger, G. Marx, E. Minaya Ramirez, L. Schweikhard and P. G. Thirolf, *First Extraction Measurements with the Cryogenic Gas Stopping Cell at SHIPTRAP*, GSI SCIENTIFIC REPORT 2012 PHN-ENNA-EXP-11

Chapter 10

Presentations

- *Erste direkte Massenmessungen an Nobelium und Lawrencium mit dem Pennigfallen-Massenspektrometer SHIPTRAP*, German Physical Society Spring Meeting Section Hadrons and Nuclei, Bonn, Germany, 15.-19.03.2010, Talk

- *Direct mass measurements above uranium*, Euroschool on Exotic Beams, Santiago de Compostela, Spain, 04.-10.09.2010, Poster

- *Penning trap-assisted decay spectroscopy at SHIPTRAP*, German Physical Society Spring Meeting Section Atomic Physics, Dresden, Germany, 14.-18.03.11, Talk

- *Penning trap-assisted decay spectroscopy at SHIPTRAP*, XXXII Mazurian Lakes Conference on Physics, Piaksi, Poland, 11.-18.9.11, Talk

- *Using the CAEN HV Classes with the LV2009 DSC-Engine*, CS Workshop, Jena, Germany, 09.-10.02.12, Talk

- *Commissioning of the Cryogenic Buffer-Gas Stopping Cell at SHIPTRAP*, German Physical Society Spring Meeting Section Hadrons and Nuclei, Mainz, Germany, 19.-23.03.12, Talk

- *Commissioning and first efficiency measurements of the cryogenic gas stopping Cell at SHIPTRAP*, TASCA 12 - 11th Workshop Recoil Separator for Superheavy Element Chemistry, Darmstadt, Germany, 14.09.12, Talk

- *SHIPTRAP - The gateway towards high-precision mass measurements of superheavy Elements*, NuStar Seminar, Darmstadt, Germany, 05.12.12, Invited Talk

- *High-precision mass measurements of the heaviest elements with SHIPTRAP*, German Physical Society Spring Meeting Section Hadrons and Nuclei, Dresden, Germany, 04.-08.03.13, Talk

- *Cryogenic gas cell at SHIPTRAP*, 11th IGISOL Workshop, Jyväskylä, Finland, 11.-13.06.13, Invited Talk

- *Cryogenic gas cell at SHIPTRAP*, NuStar Week 2013, Helsinki, Finland, 07.-11.10.13, Invited Talk

- *Q-value measurements with the PI-ICR technique at SHIPTRAP*, CS Workshop, Mainz, Germany, 10.-11.04.14, Talk

- *The SHIPTRAP cryogenic gas stopping cell*, Topical Workshop of the FLAIR Collaboration, Heidelberg, Germany, 15.-16.05.2014, Poster

Kapitel 11

Erklärung

Hiermit erkläre ich, dass diese Arbeit bisher von mir weder an der Mathematisch-Naturwissen-schaftlichen Fakultät der Ernst-Moritz-Arndt-Universität Greifswald noch einer anderen wissenschaftlichen Einrichtung zum Zwecke der Promotion eingereicht wurde.
Ferner erkläre ich, daßich diese Arbeit selbstständig verfasst und keine anderen als die darin angegebenen Hilfsmittel und Hilfen benutzt und keine Textabschnitte eines Dritten ohne Kennzeichnung übernommen habe.

Greifswald, den 18.11.2014

Danksagung